

LIBRARY  
Michigan State  
University

This is to certify that the  
dissertation entitled

IMAGE PROCESSING ENHANCEMENTS FOR SCANNING  
PROBE RECOGNITION MICROSCOPY

presented by

YUAN FAN

has been accepted towards fulfillment  
of the requirements for the

Ph.D. degree in Electrical Engineering

  
Major Professor's Signature

Aug 27, 2009  
Date



**IMAGE PROCESSING ENHANCEMENTS FOR SCANNING PROBE  
RECOGNITION MICROSCOPY**

**By**

**Yuan Fan**

**A DISSERTATION**

**Submitted to  
Michigan State University  
In partial fulfillment of the requirements  
for the degree of**

**DOCTOR OF PHILOSOPHY**

**Electrical Engineering**

**2009**

## ABSTRACT

### IMAGE PROCESSING ENHANCEMENTS FOR SCANNING PROBE RECOGNITION MICROSCOPY

By

Yuan Fan

The family of scanning probe microscopy (SPM) techniques has revolutionized studies of micro and nano objects. Nanobiology is one field which is being dramatically impacted by the newly available direct information provided by SPM techniques. Although SPM has great potential in nanobiology, it is important to realize that it also has challenges: image artifacts; slow scanning speed; difficulty in efficient recognition of the region of interest; optimization of scanning parameters. A new mode of SPM operation, Scanning Probe Recognition Microscopy (SPRM), has been developed by our group in partnership with Veeco Instruments Inc. Scanning Probe Recognition Microscopy is a new scanning probe microscopy technique which allows us to adaptively track individual structures using a fine resolution scan restricted to the region of interest, and providing statistically significant data for multiple properties. Two implementation methods, an off-line processing scheme and an on-line dynamically adaptive multi-resolution scanning mode, are developed and presented in this thesis.

A second challenge in AFM data is the distortion of the measured image due to tip-sample interaction which is significant in nanoscale metrology. Two approaches for deconvolution are investigated and applied for the first time in the estimation of true topological shape of nanoscale features from the measured height data. The first approach is based on morphological image processing and uses the geometrical tip and sample information. The second approach is a physics based deconvolution method and involves

the modeling and characterization of tip/sample interaction forces. Initial results based on modeling only Van der Waals component of the over all tip-sample interaction, show the feasibility of the method for determining true topographic shapes of the sample.

SPRM was developed within an application framework for two reasons. One was to challenge the instrument development with real versus ideal problems. Another reason was to immediately use the new SPRM capability to investigate significant problems. Tissue scaffolds built from electrospun carbon nanofibers whose purpose is bridging injuries in damaged spinal cords were characterized in terms of properties that influence neural cell growth and attachment, such as surface roughness and elasticity. The results of SPRM investigations of the surface roughness and elasticity of tissue scaffolds are presented. SPRM provided the first capability to acquire force curves directly along an individual nanofiber under optimal conditions where the tip and hence applied force is exactly normal to the curved nanofiber surface. Statistical methods based on histograms were developed to analyze the surface roughness and elasticity properties of the tissue scaffold nanofibers. This is the first time that statistically meaningful information has been extracted along individual nanofibers using an automatic procedure that maintains uniformity of experimental conditions.

**To my beloved wife and parents**

# Acknowledgement

I would like to express my sincere gratitude to Dr. Lalita Udpa and Dr. Virginia Ayres for the continuous guidance and encouragement they has provided throughout the present study. Particularly, my very special thanks to Dr. Lalita Udpa, who gave me the opportunity to pursue the Ph.D degree. I am grateful for her intellectual and financial support, inspiration, freedom of work, invaluable advice and above all trust that gave me the confidence and guided me to take the right decisions throughout my graduate studies. I also sincerely thank my coadvisor Dr. Virginia Ayres for her intellectual guidance, discussions and encouragement in many aspects of my graduate studies. She taught me the Scanning Probe Microscopy and its application. I am glad to work with my advisors and I have learned science and many invaluable moral values working with them.

I would like to thank my committee members Dr. Satish Udpa and Dr. S.D.Mahanti for taking the time to serve on my committee and for providing invaluable comments and suggestions to enhance the quality of this dissertation.

I would like to thank Ms. Qian Chen for the intellectual discussions and dedicated team work on SPRM experiments. My special thanks to my friend Dr. Zhiwei Zeng for the help on the numerical model computation. I would like to thank Shiva Arun Kumar for the intellectual discussions and team work on geometric AFM image deconvolution algorithm. I would also like to thank Ms. Xin Liu for the intellectual discussions on inverse problem. I am thankful to Benjamin W. Jacobs for providing nano circuit sample.

We collaborated with Dr. Sally Meiners of UMDNJ-Robert Wood Johnson Medical School in application of SPRM in tissue scaffolds. I would like to express my gratitude to the collaborators for providing tissue scaffold sample and helpful discussion.

Once again I thank each person related to this work directly or indirectly for the successful completion of the dissertation.

Finally, I would like to thank my wife Jun Chen and my parents, Peilian Fan and Yuede Shen, for their unconditional support, love and caring. To them, I dedicate this dissertation.

## TABLE OF CONTENTS

LIST OF FIGURES .....	IX
CHAPTER 1 INTRODUCTION .....	1
1.1 Motivation.....	1
1.2 Overview of Scanning Probe Microscope Family .....	1
1.3 SPM Family .....	3
1.4 Atomic Force Microscopy .....	5
1.4.1 AFM System .....	6
1.4.2 Imaging Modes .....	10
1.5 Applications of AFM.....	13
1.6 Summary of the Later Chapters .....	15
CHAPTER 2 IMAGE PROCESSING CHALLENGES IN AFM.....	17
2.1 Analysis Challenge .....	17
2.1.1 Imaging Artifacts .....	17
2.1.2 Region of Interest Recognition .....	19
2.2 Implementation Challenge.....	21
2.2.1 Scan Speed .....	21
2.2.2 Scanning Parameters Optimization.....	24
2.3 Challenges and Opportunities for Data Fusion.....	25
CHAPTER 3 DEVELOPMENT OF SPRM .....	27
3.1 Off-line Processing Mode.....	29
3.1.1 Multi Scale Analysis.....	31
3.1.2 Skeleton analysis.....	32
3.2 Online Scanning Mode .....	39
3.2.1 Online Scan Plan Generation .....	39
3.2.2 Fine Resolution Scan Plan .....	43
3.3 Real Time Display .....	47
CHAPTER 4 IMAGE RECONSTRUCTION BASED ON GEOMETRIC DECONVOLUTION .....	49
4.1 Deconvolution in Atomic Force Microscopy .....	50
4.2 Morphological Processing Technique for Surface Reconstruction .....	51
4.3 Legendre Transform Technique for Sample Surface Reconstruction.....	55
4.4 Blind Tip Estimation.....	60
4.5 Example Applications of Deconvolution for Nanobiology .....	62
4.6 Conclusions.....	65
CHAPTER 5 DECONVOLUTION BASED ON THE TIP-SAMPLE INTERACTION FORCE MODEL .....	67

5.1 Summary of Tip Sample Interaction..... 67

5.2 Van der Waals Force Model ..... 71

    5.2.1 Model Equation..... 74

    5.2.2 Parameter Estimation and Model Validation..... 77

5.3 Numerical Result of Van der Waals (VDW) Force Model..... 82

    5.3.1 Surface Discretization..... 83

    5.3.2 Numerical Model Validation ..... 89

5.4 Model Based Deconvolution of AFM Image..... 93

5.5 Implementation Results ..... 95

**CHAPTER 6 APPLICATION OF SPRM TO TISSUE ENGINEERING ..... 101**

    6.1 Introduction..... 101

    6.2 Materials and Methods..... 103

    6.3 Surface Roughness..... 104

    6.4 Elasticity ..... 111

    6.5 Discussion ..... 124

**CHAPTER 7 SUMMARY OF RESULTS AND FUTURE WORK..... 126**

**REFERENCE:..... 130**

## List of Figures

Figure 1.1 Block diagram of the SPM .....	2
Figure 1.2 Lateral Force Microscopy.....	4
Figure 1.3 Magnetic Force Microscopy.....	4
Figure 1.4 Schematic of the AFM system .....	7
Figure 1.5 Tip-sample interaction force VS. distance .....	8
Figure 1.6 Quad-Photodiode orientation.....	8
Figure 1.7 Schematic of FM-AFM .....	13
Figure 2.1 Example of the dilation artifact (Solid line: experimental profile; Dash line: theoretical profile).....	18
Figure 2.2 AFM image of biological sample with two different types of ROI. AFM images by Y. Fan and Q. Chen. Cell and tissue samples from S. Meiners, college of Medicine UMDNJ.....	20
Figure 2.3 Typical scanner piezo tube and X-Y-Z electrical configurations [59].....	22
Figure 2.4 Schematic of traditional raster scan pattern on a tissue scaffold sample .....	23
Figure 2.5 AFM image of DNA structure, Courtesy J. Reed, UCLA.....	23
Figure 3.1 Block diagram of the dynamic scanning system. ....	27
Figure 3.2 Signal Access Module [60] .....	28
Figure 3.3 AFM image of DNA molecules (Image size: $0.5 \times 0.5 \mu\text{m}^2$ ) [61] .....	30
Figure 3.4 Result of offline processing [62] .....	32
Figure 3.5 AFM image of DNA structure, Courtesy J. Reed, UCLA.....	33
Figure 3.6 Flow chart of the Contour-Pruned skeletonization algorithm .....	35
Figure 3.7 Object and inscribed circle .....	36

Figure 3.8 Skeletonization results: (a) raw DNA image; (b) binary image; (c) radius of the maximum inscribed circle; (d) image of length of segmented perimeter; (e) skeleton image; (f) skeleton image shown in original DNA image. ....	38
Figure 3.9 Skeleton of the DNA image (a) without pruning (b) with pruning .....	39
Figure 3.10 Online multi-ROI scan plan flowchart .....	41
Figure 3.11 Schematic of single ROI scanning mode.....	42
Figure 3.12 Fine scan without prediction (a) Conventional AFM image of the nanofiber (b) Coarse Scan picks up the first nanofiber; (c) Fine scan only on the first nanofiber (d) Finish the fine scan and return to coarse scan to find another region of interest; (e) Coarse Scan picks up the second nanofiber; (f) Fine scan only on the second nanofiber (g) Finish the high resolution fine scan only on the second nanofiber .....	43
Figure 3.13 AFM image of the tissue scaffold sample with cross section area.....	44
Figure 3.14 SPRM scan plan of intersecting tissue scaffold sample. 1(a)-(d) shows SPRM scan without prediction; 2(a)-(d) shows corresponding SPRM scan with prediction .....	46
Figure 3.15 SPRM scan image of the nanofiber. (a) Conventional AFM image of the nanofiber (b) Coarse Scan picks up the first nanofiber; (c) Finish high resolution fine scan only on the first nanofiber and return to coarse scan to find another region of interest; (d) Coarse Scan picks up the second nanofiber; (e) Finish the high resolution fine scan only on the second nanofiber and return to coarse scan to find another region of interest; (f) Coarse Scan picks up the third nanofiber; (g) Finish the high resolution fine scan only on the third nanofiber.....	48
Figure 4.1 Morphological dilation Model of AFM image data with sharp surface features ( Note : The tip surface is reflected about its origin in accordance with equation (4.3)) [73, 74] .....	52
Figure 4.2 Surface reconstruction using grayscale morphological erosion [74]. .....	53
Figure 4.3 Results of Morphological Processing (a) True (known) Specimen Surface (b) Simulated AFM Image (c) Reconstructed Specimen Surface (d) Profile Comparison ....	55
Figure 4.4 A schematic of tip surface, sample surface and image surface [76] .....	56
Figure 4.5 Relationship between the Legendre Transform of the sample surface (black bold), image surface (dotted) and tip surface [73].....	59
Figure 4.6 Application of the Legendre transform to an artificial AFM height image(a) True surface image of a cylindrical structure of 500nm diameter and 800nm high. (b)	

Simulated AFM image using 20nm parabolic tip. (c) Reconstructed image. (d) Profiles of measured and reconstructed images [73].	59
Figure 4.7 Blind tip estimation results at different iterations (a) initial guess,(b) 1st iteration,(c) 2 <sup>nd</sup> iteration & (d) final estimate of the tip shape after convergence [73].	62
Figure 4.8 AFM images of NRK2 cell on polymer tissue scaffolding (a) top view and (b) surface plot. Two ambiguous features are circled (1) the actual width of the scaffold fibers and (2) a sharp feature on the cell surface [73].	63
Figure 4.9 Comparison of line scans in (a) Region1 and (b) Region 2 of Figure 4.8 showing deconvolution of fiber width [73].	64
Figure 5.1 Schematic of the liner, time invariant system	67
Figure 5.2 Force curve.	68
Figure 5.3 Integration of the interaction force between two arbitrarily shaped bodies	72
Figure 5.4 Schematic of the tip model. R is the radius of the spherical cap. $\alpha$ is the angle include the spherical cap, $\beta$ is the cone angle, $z_0$ is the distance between the tip end and sample.	74
Figure 5.5 Schematic of the spherical cap	75
Figure 5.6 Schematic of the truncated cone.	76
Figure 5.7 schematic of the tip and sample position in z direction.	78
Figure 5.8 Ten experimental force curves in same sample position.	80
Figure 5.9 A scheme showing the estimation of the unknown parameters and comparison of the theoretical force curve with the experimental data	81
Figure 5.10 Schema of Van der Waals force calculation.	82
Figure 5.11 Discretization of spherical cap.	84
Figure 5.12 (a) Schematic of elements in spherical cap (b) Cross section of spherical cap in x-z plane (c) Cross section of spherical cap in x-y plane.	85
Figure 5.13 Mesh in truncated cone.	87
Figure 5.14 (a) Schematic of the mesh in truncated cone (b) Cross section of truncated cone in x-z plane (c) Cross section of truncated cone in x-y plane.	88

Figure 5.15. Mesh of the tip and sample.....	90
Figure 5.16 Force vs. Size of integration area in sample surface .....	91
Figure 5.17 Force vs. Size of integration area in tip surface .....	92
Figure 5.18 Force vs. tip-sample distance .....	93
Figure 5.19 Schematic of AFM image deconvolution using force model .....	94
Figure 5.20 Procedure of AFM image deconvolution using force model. ....	94
Figure 5.21 Schematic of the tip and sample surface .....	96
Figure 5.22 Mesh of the sample surface .....	96
Figure 5.23 Line scan of the scan image and initial guess image.....	97
Figure 5.24 Result of the image deconvolution using VDW force model.....	98
Figure 5.25 Schematic of the tip and sample.....	99
Figure 5.26 Result of the image deconvolution using VDW force model.....	100
Figure 6.1 (a) AFM image of electrospun carbon nanofiber tissue scaffold. The scan area is 5 square microns and the z-height projection is 1500 nanometers. (b) SEM image of electrospun carbon nanofiber tissue scaffold. The scan area is 20 square microns, images by Q. Chen and Y. Fan [70]......	106
Figure 6.2 SPRM scan image of the nanofiber. (a) Conventional AFM image of the nanofiber (b) Coarse Scan picks up the first nanofiber; (c) Finish high resolution fine scan only on the first nanofiber and return to coarse scan to find another region of interest; (d) Coarse Scan picks up the second nanofiber; (e) Finish the high resolution fine scan only on the second nanofiber and return to coarse scan to find another region of interest; (f) Coarse Scan picks up the third nanofiber; (g) Finish the high resolution fine scan only on the third nanofiber. Images by Y. Fan and Q. Chen [109]......	107
Figure 6.3 Circle fit based on Kása method [70] .....	108
Figure 6.4 (a) Characteristic tip-dilation artifacts (b) The cross section of a real AFM nano fiber image and the best fit circle [70] .....	109
Figure 6.5 Surface roughness map along individual fiber [109] .....	110
Figure 6.6 Histogram of surface roughness map [109]......	111

Figure 6.7 Approach force curve and corresponding tip sample distance .....	113
Figure 6.8 Traditional AFM force volume image.....	114
Figure 6.9 (a) Tissue scaffold surface the tip contact point (b) 6 points were acquired along the individual nanofiber .....	115
Figure 6.10 SPRM force curve signal timing waveform .....	117
Figure 6.11 Force curve collected by the second PC.....	117
Figure 6.12 Approace force curve after average filter.....	118
Figure 6.13 Force-distance curve and corresponding force-distance curve .....	119
Figure 6.14 Force curve in contact region (a) and corresponding fitting result (b).....	123
Figure 6.15 Box plot of the estimated Young's modulus .....	124

# Chapter 1 Introduction

## 1.1 Motivation

The family of scanning probe microscopy (SPM) techniques has revolutionized studies of nanostructures. The key capability of scanning probe microscopy is that, through a controlled combination of feedback loops, detectors and piezoelectric actuation, it enables direct investigations of micron, nanometer to atomic scale phenomena. One important emerging area of application for SPM is in nanobiology. The main advantages of SPM in nanobiology are that it requires minimal sample preparation, and reaches macromolecular resolution under near life-like conditions. Although SPM has great potential in nanobiology, it is important to realize that it also has some drawbacks. These challenges include: image artifacts; slow scanning speed; difficulty in efficient recognition of the region of interest; optimization of scanning parameters. Furthermore, from the different types of information provided by the SPM it would be desirable to construct a composite picture representative of a living specimen's perception of its environment. These challenges are addressed in this thesis via development and application of appropriate signal processing and pattern recognition algorithms which are integrated with SPM to build a system that we refer to as the scanning probe recognition microscope (SPRM).

## 1.2 Overview of Scanning Probe Microscope Family

The family of scanning probe microscopy techniques started with invention of the scanning tunneling microscope (STM) in 1981 [1], which offered the capability for high

resolution imaging of surfaces of conducting and semiconducting materials [2, 3]. The invention of STM was considered so significant that it was awarded the Nobel Prize in Physics in 1986, one of only four such prizes given for the development of an instrument. It received a significant extension in 1986 with the invention of the atomic force microscopy [4] which brought the power of the SPM analysis to non-conductive samples in air and liquid environments [5]. The SPM family has since made a dramatic impact in many fields such as materials science, semiconductor physics, biology, electrochemistry, biochemistry, organic chemistry, catalysis, micromechanics, and medical implant technology etc [6]. The SPM provides three-dimensional, real-space images of surfaces at nanoscale spatial resolution. Images are based on the local inter-atomic forces of interaction between a small probe tip and surface features.

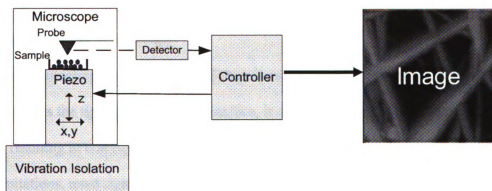


**Figure 1.1 Block diagram of the SPM**

Figure 1.1 shows a block diagram of a Scanning Probe Microscope. Instead of using light or focused electrons, scanning probe microscopes use a tiny needle like probe attached to a cantilever that is scanned across the specimen surface. The interactions between probe and sample are recorded and processed to form an image. Scanning probe microscopes can visualize a sample surface, in micro/nano/atomic resolution in three dimensions and generate images which are spatial maps of sample properties such as thermal conductivity,

friction, hardness, elasticity, magnetic permeability and chemical binding etc. The operational environment of SPM can be ambient air, liquid or vacuum. Each SPM technique (STM, AFM etc) includes a family of microscopy modalities i.e. constant current imaging in addition to constant height imaging. Different modalities of SPM measurements provide different types of information about physical surface, topography, electronic structure, electric or magnetic fields and many other local properties.

### **1.3 SPM Family**

Since its invention in 1981, SPM has developed into a family of instruments. Different modalities of SPM measurements provide different types of information about physical surface, topography, electronic structure, electric or magnetic fields and other local properties as described below:

#### **Scanning Tunneling Microscopy**

Scanning tunneling microscopy (STM) monitors the tunneling current between the tip and sample. As the tip scans the sample surface, it encounters sample features of different heights, resulting in corresponding changes in the tunneling current. However STM has some limitations, most significant of which is that the surface of both the tip and sample must be good conductors. This severely limits the type of materials that can be studied.

#### **Atomic Force Microscopy**

The atomic force microscopy (AFM) [4] initially developed to overcome the limitations of the STM in imaging the non-conducting materials. AFM operates by scanning a tip attached to the end of a cantilever across the sample surface while monitoring the change in cantilever deflection with a split photodiode detector.

## Lateral Force Microscopy

Lateral force microscopy (LFM) [7-9] measures lateral deflections of the cantilever that arise from shear/friction forces on the cantilever normal to the z direction. LFM studies are useful for imaging variations in surface friction that can arise from inhomogeneity in surface material.

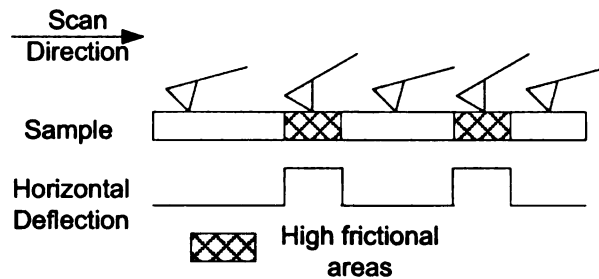


Figure 1.2 Lateral Force Microscopy

## Magnetic Force Microscopy

Magnetic Force Microscopy (MFM) [10] images the spatial variation of magnetic forces on a sample surface. For MFM, the tip is coated with a ferromagnetic thin film. The system operates in non-contact mode, detecting changes in the resonant frequency of the cantilever induced by the magnetic field/s depending on tip-sample separation. MFM can be used to image naturally occurring and deliberately written domain structures in magnetic materials.

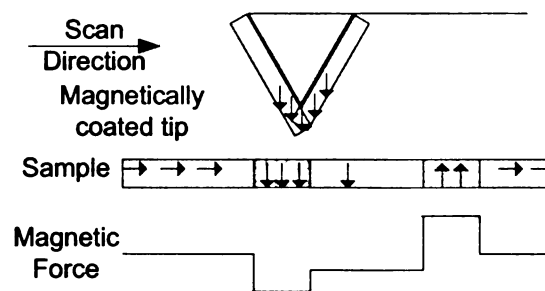


Figure 1.3 Magnetic Force Microscopy

## Electric Force Microscopy

Electric force microscopy (EFM) [11-13] applies a voltage between the tip and the sample while the cantilever hovers above the surface, not touching it. The cantilever deflects when it scans over static charges. EFM plots the locally charged domains of the sample surface. EFM is used to study the spatial variation of surface charge carrier density.

### **Scanning Capacitance Microscopy**

Scanning capacitance microscopy (SCM) [14-16] images spatial variations in capacitance. The cantilever operates in non-contact, constant-height mode. A special circuit monitors the capacitance between the tip and sample. SCM studies can image variations in the thickness of a dielectric material on a semiconductor substrate. SCM can also be used to visualize sub-surface charge carrier distributions.

Other forms of SPM include Surface Potential Microscopy [17-19], Electrochemical STM & AFM [20], Scanning Thermal Microscopy [21, 22], Photon Scanning Tunneling Microscopy [23] and Near-field Scanning Optical Microscopy [24] etc. This thesis focuses on the application of one SPM technique, namely, Atomic Force Microscopy (AFM).

## **1.4 Atomic Force Microscopy**

The principle of STM makes it not suitable for imaging largely nonconductive biological samples, and this led to the development of the AFM for nanbiological research. Because of its ability to provide active and high resolution probing of specimens with minimal sample preparation and under nearly lifelike conditions, the potential of AFM for use in investigating minimally conductive biological surfaces was immediately recognized.

A brief description of the operating principles of AFM is given in this section. More detailed information related to instrumental aspects of the AFM can be found in several excellent reviews [25, 26].

In an Atomic Force Microscope, a minute tip is mounted at the end of a flexible micro-cantilever and is maintained in gentle 'contact' with the sample surface. As investigated within this thesis, 'contact' is really a precise summation of all possible Coulomb interactions between the tip and the sample. When the term 'contact' is used in this thesis, the more precise summation tip-sample interaction force is implied. The tip scans the sample in a raster fashion. The tip movement is performed with sub-angstrom accuracy by a piezoelectric actuator. AFM is capable of generating 3D images of surface topography with nanometer resolutions. It can operate in vacuum, ambient air and liquid. With the tip in direct contact with a biological specimen, AFM offers insight into cellular and sub-cellular features. With its sensitivity down to tens of pico-newtons, AFM can also make nano mechanical measurements of elasticity [27].

### **1.4.1 AFM System**

Figure 1.4 shows a schematic representation of the different components in an AFM.

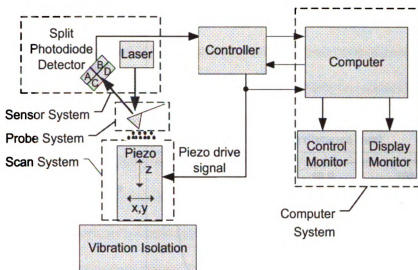


**Figure 1.4 Schematic of the AFM system**

A generic AFM comprises the following components: scanning system; probe system; sensor system; vibration isolation; controller; computer system.

The AFM measures the interaction force between the sample and a very sharp tip which is attached to a spring cantilever typically micro-fabricated from silicon or silicon nitride with length of the cantilever ranging from several microns to hundreds of microns. When the cantilever tip is brought close to the sample surface, the interaction force between the tip and sample surface causes the cantilever to bend, or deflect. Different types of tip sample interaction force can be measured depending on the distance between the tip and sample as shown in Figure 1.5. When the tip is far away the sample surface (>several tens of nanometers), long-range attractive interactions, such as the electric and magnetic forces, may be the main source of the tip-sample interaction. When the tip-sample distance is one to several tens of nanometers, the mid-range attractive force, Van der Waals force, usually dominate the tip-sample interaction. As the tip is brought close to 'contact' the sample surface at about 1nm, the short-range ion-ion repulsive force dominates the tip sample interactions.

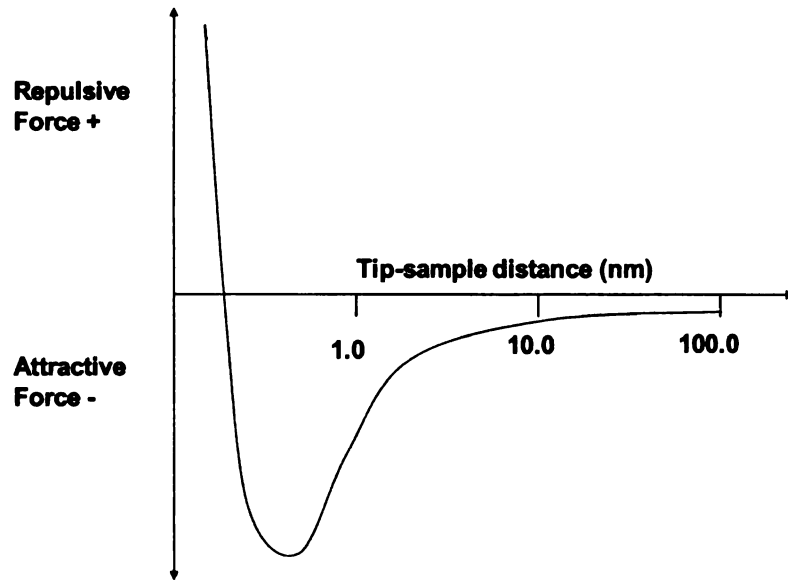


**Figure 1.5 Tip-sample interaction force VS. distance**

A laser beam shines on and reflects off the back of the cantilever onto a quad-photodiode to measure the cantilever deflection both in vertical and lateral direction.

Figure 1.6 shows the schematic of a quad-photodiode.

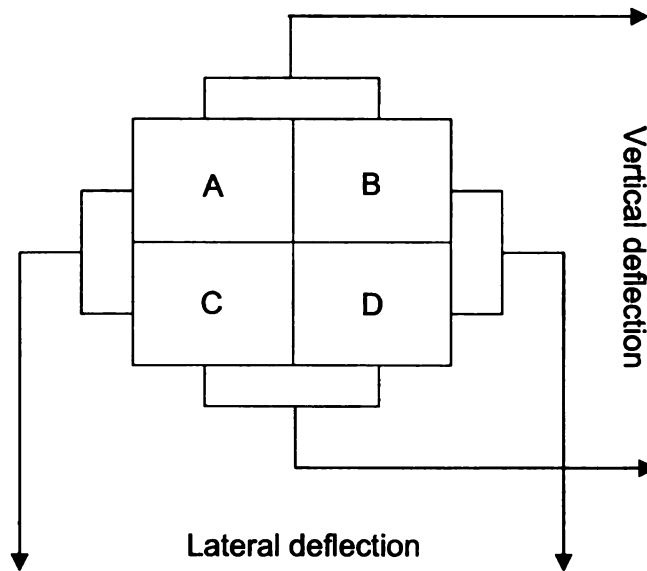


**Figure 1.6 Quad-Photodiode orientation**

The vertical deflection is calculated as:

$$D_v = \frac{(A+B)-(C+D)}{A+B+C+D} \quad (1.1)$$

The lateral deflection is calculated as:

$$D_l = \frac{(A+C)-(B+D)}{A+B+C+D} \quad (1.2)$$

The sample is mounted on the top of a piezoelectric scanner that provides sub-angstrom motion increments in the lateral (x, y) and vertical (z) directions.

A controller provides the interface between the computer, sensor system and scanning system. The controller converts the photodiode output analog voltage signal to digital signal and sends it to the computer. The controller also generates the voltage drive signal for the piezoelectric scanner to control the sample movement in all directions. In the x and y direction the piezo drive signal may be generated by an open loop control circuit according to the scan command sent by computer, while the z directional drive signal is generated by a proportional integral (PI) close loop controller. The z feedback loop can maintain a specific quantity, such as force on the tip, amplitude of tip oscillation or frequency of tip oscillation, at a constant user specified value by changing the z piezo voltage drive signal which moves the sample up or down.

Mechanical vibrations are a large component of the system noise, and it is a major challenge to reduce the vibration noise while maintaining the system sensitivity down to tens of pico-newtons. These vibrations can originate from the building, the chamber or the table on which the microscope sits. To achieve the highest resolution, the microscope must be vibrationally isolated from its surroundings. The low frequency vibration mainly comes from the building. An effective way to damp vibration is to suspend the microscope on long tension wires. This can be accomplished by suspending a massive

table from the ceiling by cords. The length of the cord, the mass of the table, and the spring constant of the cords can be varied to achieve maximum attenuation at the frequency of concern. A second approach to damping low frequency vibration is to levitate the system on air cushioned feet. In our lab, the AFM system is put in a mass table as an effective but simple way for isolating AFMs from floor vibrations and from acoustic vibration sources, while the STM system is isolated using tripod based suspension mount.

A computer drives the scanner system, acquires, processes, displays and analyzes the data produced. The computer also provides a user interface for operator to set scan parameters.

In this research, the AFM used is Digital Instrument's Multimode Nanoscope IIIa.

### **1.4.2 Imaging Modes**

The AFM works in three different imaging modalities or modes. These are contact mode; tapping mode; non-contact mode.

#### **Contact Mode:**

The first imaging mode that was developed is the contact mode. Contact mode AFM operates by scanning a tip attached to the end of a cantilever across the sample surface while monitoring the change in cantilever deflection with a split photodiode detector. During scanning, in ambient air which is the easiest and most commonly used sample preparations, the tip contacts the surface through the humidity fluid layer on the sample surface. In z direction, a feedback loop maintains a constant cantilever deflection, to user "set-point" deflection value, by moving the scanner, vertically up or down, at each (x, y)

data point. The force between the tip and sample can be calculated from the cantilever deflection using Hooke's Law:

$$F = k \cdot x \quad (1.3)$$

where F: Force;

k: spring constant;

x: cantilever deflection.

Maintaining a constant cantilever deflection implies that the force between the tip and the sample remains constant. By recording the close-loop voltage applied to the z-axis piezo simultaneously with the sample's x and y position, the topography or height image of the sample surface can be inferred and stored in the computer. In contact mode, the deflection of the cantilever that occurs prior to re-establishing the constant force via the z-feedback loop, is also recorded and displayed as deflection image data. The deflection image is more sensitive to sharp sample feature. This mode of operation can take place in ambient air and liquid environments.

#### **Tapping Mode:**

In the tapping mode, which is also called intermittent contact mode, the cantilever is oscillated at or near its resonance frequency with amplitude ranging typically from 20nm to 100nm. The tip taps lightly on the sample surface during scanning, contacting the surface at the bottom of its swing. The tip oscillation amplitude changes in response to the tip-sample distance from its initial free oscillation to a different amplitude and frequency that reflects some property of the sample surface. The feedback loop maintains constant oscillation amplitude based on constant RMS amplitude as recorded by the four-cell photodiode. The vertical position of scanner at each (x, y) point that maintains the

'setpoint' amplitude is recorded by the computer to generate a topographic or height image of the sample surface. The frequency change of the tip oscillation near the sample surface relative to the free resonant frequency of cantilever oscillation can also be recorded by computer at the same time to generate a phase shift or phase image. The high sensitivity of the phase shifts due to material and topographic properties has made phase images a very useful tool in many applications. However, since it is difficult to isolate the different sample properties responsible for the phase shift, quantitative analysis of the sample properties using phase image is still limited. The tapping mode operation can be performed in vacuum, ambient and liquid environments although the damping effects of the liquids on cantilever oscillation must be taken into account..

#### **Non-contact Mode**

Non-contact mode of AFM operation is very similar to the tapping mode except that the tip does not contact the sample surface but oscillates above the sample surface. The resonance frequency, amplitude and phase shift of the tip vibration are related to the tip-surface interaction. The feedback loop can use any of these values as a parameter to maintain a constant tip-sample separation by vertically moving the scanner at each point (x, y) and generate a topography image. There are two major non-contact AFM modes, amplitude modulation atomic force microscopy (AM-AFM) [28-30] and frequency modulation atomic force microscopy (FM-AFM) [30, 31]. In AM-AFM, the z direction feedback loop maintains the amplitude of cantilever oscillation at the "set-point" value to generate the sample surface topography image. The drive signal of the cantilever oscillation is a constant amplitude and frequency excitation. While in FM-AFM, the cantilever is a self-driven oscillator. The cantilever oscillates with constant amplitude at

its current resonance frequency which is different from the free cantilever resonance frequency due to the tip-sample interaction. Figure 1.7 shows a schematic of FM-AFM.

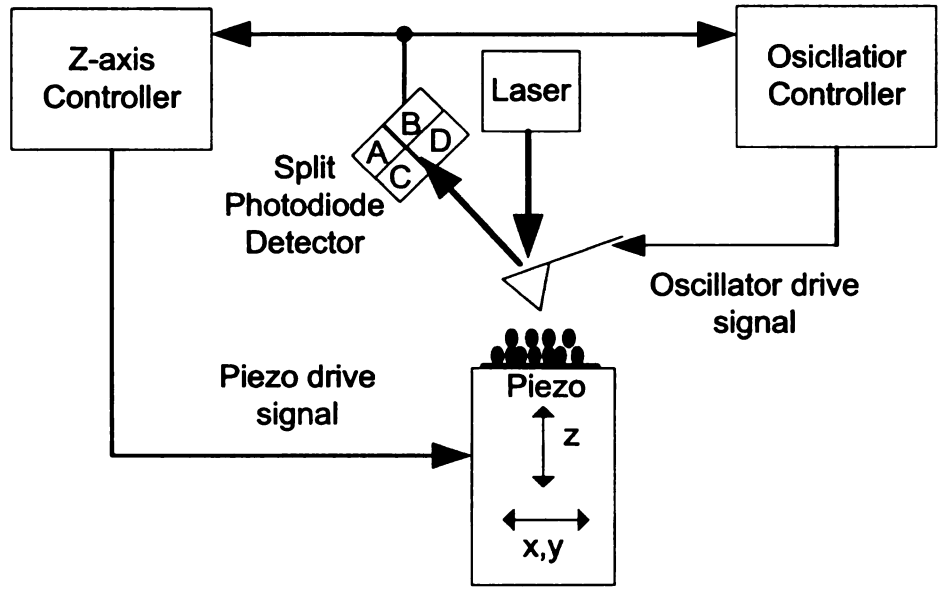


Figure 1.7 Schematic of FM-AFM

Two feedback loops are used by the controller. One feedback loop keeps the oscillation amplitude at the constant value by changing the cantilever oscillation drive signal. The difference between the current resonance frequency and that of the free lever,  $\Delta f$ , is used as the z-direction feedback loop parameters. By moving the sample up and down, the z-direction feedback loop maintains the constant value for  $\Delta f$ . The distance that the scanner moves vertically at each (x, y) position is stored in the computer to generate a topographic image of the sample surface. Currently, the non-contact mode AFM mostly performs in ultra high vacuum (UHV) because of the very weak forces involved.

## 1.5 Applications of AFM

The family of Scanning Probe Microscopy techniques have revolutionized studies of semiconductors [32-34], polymers [35-37], nanostructures [38] and biological systems [39-43]. This thesis will focus on study of SPM applications for imaging biological samples.

The potential of scanning probe microscopy for use in biological studies was immediately recognized, and research efforts began shortly after the invention of STM. The original nano-Amp STM was not suitable for imaging largely nonconductive biological samples, and this led to the development of the atomic force microscope (AFM) for nanobiological research. As the nano-Newton tip-sample interaction forces of AFM proved to be sufficient to damage soft biological tissues, pico-Newton imaging systems based on perturbations to a freely oscillating cantilever were developed (Tapping Mode or non-contact AFM). Liquid environment systems that greatly reduced Van der Waals and surface adhesive forces were also developed [44, 45]. The successful operation of AFM techniques in liquid ambient environments also provides another important capability for biological investigations: the ability to conduct direct investigations under nearly life-like conditions [46].

AFM contributions in nanobiology and medicine has been revolutionary in that it includes: the first direct observations of DNA and RNA [47, 48], the first direct investigations of membrane proteins [49], the first direct investigations of ligand binding by functionalized tip AFM [50] and many more important first direct studies. A persuasive argument for the use of AFM techniques in nanobiology is that it is a direct investigative technique in a field that has largely relied on indirect or after-the-fact observations. Recognition of the importance of AFM techniques for medically relevant

nanobiological investigations is growing rapidly [51]. Examples of recent studies include high resolution combined topographical and mechanical studies for multiple living cells types [51-53], direct investigations of the growth cones on living neurons [51], and, opening up an very important nanobiological research area, the first direct single molecule investigations [40, 51, 54].

The main advantages of AFM in nanobiology are that it easily reaches macromolecular resolution, with minimal sample preparation, and under nearly life-like conditions. A drawback of AFM is that it has been a surface technique requiring complementary investigations to provide sub-surface information. However, sub-cellular AFM is also under development [51, 55]. Although AFM has considerable potential in molecular and nanobiology, it is important to realize that accurate data collection is often challenged by several limitations and difficulties associated with existing commercial systems.

## **1.6 Summary of the Later Chapters**

The challenges addressed in this thesis are introduced in Chapter 2. Chapter 3 addresses the need for improved scanning efficiency. Two implementation methods, namely, off-line processing scheme and an on-line dynamically adaptive multi-resolution scanning mode, are presented. A dynamic or adaptive, site specific scanning feature is developed and mechanisms for incorporating this feature in commercial AFM systems are also discussed. The nature and source of image artifacts are described in Chapter 4 in detail with respect to operation of AFM in contact mode. Two different classes of

methods that are widely used in AFM image deconvolution, namely, mathematical morphology [56] and Legendre transforms [57], are discussed. An alternate approach for AFM data restoration is physics based deconvolution which includes the modeling and characterization of the tip and sample artifact sources. Investigations that model the tip-sample interaction are presented in the Chapter 5. An iterative procedure based on the tip-force interaction model is proposed to deconvolve the image. And results of two different samples are shown and compared with the result of geometrical deconvolution method. Chapter 6 introduces the application of SPRM in tissue scaffold engineering. Two important properties of the bio sample, surface roughness and elasticity, are introduced and the role of deconvolution in each is identified. The future works are summarized in chapter 7.

## **Chapter 2 Image processing challenges in AFM**

The main advantages of AFM in nanobiology are that it easily reaches macromolecular resolution, with minimal sample preparation, and under nearly life-like conditions. A drawback of AFM is that it has been a surface technique requiring complementary investigations to provide sub-surface information. However, sub-cellular AFM is also under development [51, 55]. Although AFM has considerable potential in molecular and nanobiology, it is important to realize that accurate data collection is often challenged by several limitations and difficulties associated with existing commercial systems.

These limitations are the main focus of this research. Limitations include: image artifacts; slow scanning speed; lack of automated recognition of region of interest (ROI); not optimized scanning parameters. These difficulties can be addressed by incorporating a number of image and signal processing solutions to the raw data acquired by the AFM. Further, due to the multi-modal nature of data provided by SPM systems, a composite picture representative of a sample environment can be obtained using data fusion algorithms. This thesis attempts to address many of these disadvantages within the framework of the Scanning Probe Recognition Microscope.

### **2.1 Analysis Challenge**

#### **2.1.1 Imaging Artifacts**

In atomic force microscopy, a sharp tip is brought within nanometers of a sample surface by the z-motion of a piezoelectric scanner and held there by a z-feedback loop.

Any tip shape introduces significant artifacts in the form of physically missed region information. In addition to missed regions, contact at any point other than the tip will result in an image smearing or dilation artifact. Figure 2.1(a) shows an example of the dilation artifact. In the figure, the red dashed line shows the theoretical profile of the sample surface and black line shows the corresponding profile in the experimental scanned image data.

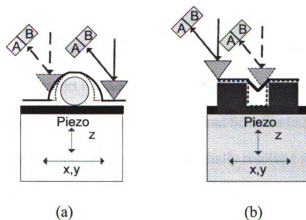


**Figure 2.1 Example of the dilation artifact (Solid line: experimental profile; Dash line: theoretical profile)**

The sample surface may also contribute missing region and dilation artifacts of its own as shown in Figure 2.1 (b).

The AFM tip-sample interaction is caused by the summation of all possible Coulomb forces between the tip and the sample, summed along the physical structure of the tip and a local region of the sample surface. These forces can introduce distortions into the information that represents some given aspect of the sample surface. In the case of a yielding or soft sample, which is the case in cellular imaging, any deformation of the sample surface can dynamically change the interaction forces in play. This means that for fully understanding the acquired data a dynamic model that takes into account contribution of the electrostatic force component in the tip-sample interaction at each

position of the tip, is needed [51-53], since an a priori model of such highly individual conditions cannot exist. Another common artifact is due to drag through a surface water layer which introduces torsioning of the cantilever that is due to the water layer not to the sample topography. Also when a tip is raised or lowered through the surface layer while maintaining its z-feedback condition, it feels vertical adhesive forces as well. Therefore, tip shape, surface shapes, surface environment and yielding surfaces can all result in information artifacts.

Physics based approach for enhancing accuracy of measurements include the work by Grimellec et al [58], where effort is made to reduce the tip-sample interaction for increasing the accuracy of height imaging data. Jiao and Schaffer [52] use additional information about the mechanical properties from spatially resolved force curve at each pixel to obtain accurate height and volume information of soft samples. Touhami et al [53] use a similar approach for mapping of elasticity of microbial cells. Physics based approaches are often developed where a problem with imaging artifacts has required that careful attention be paid to data interpretation. A new signal processing research field could evolve from the systematic integration of physics based information with powerful image processing and deconvolution techniques to increase both the extraction and the reliability of the data.

### **2.1.2 Region of Interest Recognition**

In scanning probe microscope investigation, because a tip is in actual direct interaction with a nanoscale object rather than viewing its image, this gives the system itself the

potential for site-specific probing, in addition to its current high-resolution imaging.

Figure 2.2 shows two examples of AFM imaging of biological samples. Figure 2.2 (a) shows an ordinary AFM image of an NIH 3T3 fibroblast cell. Figure 2.2 (b) shows an ordinary AFM image of a tissue scaffold of the type used for cell re-growth in regenerative medicine. These two examples show two different types of region of interest (ROI) problems in ordinary SPM imaging.

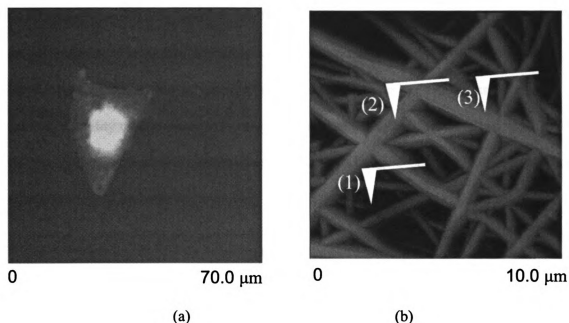


**Figure 2.2 AFM image of biological sample with two different types of ROI. AFM images by Y. Fan and Q. Chen. Cell and tissue samples from S. Meiners, college of Medicine UMDNJ**

Figure 2.2 (a) shows AFM image of fibroblasts grown on plastic 2D surface. The traditional SPM will scan the whole area while the region of interest in the image is only the cell. Figure 2.2 (b) shows an AFM image of the tissue scaffold sample, in which analysis of the properties of individual nanofibers which affect their biocompatibility is the goal. As shown in the Figure 2.2 (b), the ordinary AFM image contains data point (1), off the nano fiber, data point (3), on the side of the nanofiber, and data point (2) in the center of the nanofiber. When imaging the nanofiber, the ROI is along the individual

nanofiber. While analysis the surface roughness of the nanofiber, only the top of nanofiber is not limited by geometric dilation and provide reliable data. The ROI thus is only the top of the individual nanofiber in this case. While investigating the elasticity of nanofiber, only the center line of the nanofiber is the ROI since only in this place tip is normal to the sample surface.

To rapidly and reliably detect the region of interest is a highly desirable goal. In order to achieve this goal the Scanning Probe Microscope system itself should be given the ability to return to a specific nanoscale feature of interest by recognizing the way that site is detected by the SPM system rather than by the way the site looks to a human operator. Such a capability can be realized if the system has the ability to combine Scanning Probe Microscope piezoelectric implementation with on-line image processing and dynamically adaptive learning algorithms

## **2.2 Implementation Challenge**

### **2.2.1 Scan Speed**

In traditional SPM, the tip scans inside a regular rectangular area following a raster pattern. In virtually all scanning probe microscopes, a piezoelectric scanner is used as an extremely high resolution positioning stage to move the probe over the sample (or the sample under the probe). Figure 2.3 shows typical scanner piezo tube and X-Y-Z electrical configurations.

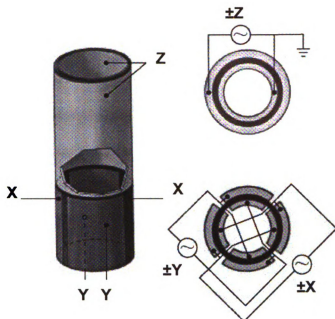


**Figure 2.3 Typical scanner piezo tube and X-Y-Z electrical configurations [59]**

The scan motion in the x-y plane is controlled by applying AC voltage to the scanner's piezoelectric crystal X-Y axes as represented in Figure 2.3. In this example, the horizontal axis presented on the display monitor is referred to as the “fast axis” or X-axis and scans at a preset scan rate entered by the user. The orthogonal axis is known as the “slow axis” or Y-axis.

In the SPM, an AC voltage applied to the x-y Piezo scanner produces a raster pattern in the x-y scan plan. Figure 2.4 shows a traditional raster scan pattern on a tissue scaffold sample. The scanner moves across the first line of the scan (fast axis), and back. It then steps in the perpendicular direction (slow axis) to the second scan line, moves across it and back, then to the third line, and so forth. The path differs from a traditional raster pattern in that the alternating lines of data are acquired in opposite directions. SPM data are collected in only one direction—commonly called the fast-scan direction—to minimize line-to-line registration errors that result from scanner hysteresis.

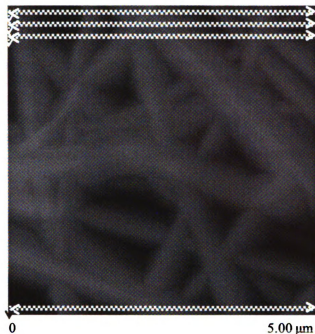


**Figure 2.4 Schematic of traditional raster scan pattern on a tissue scaffold sample**

The traditional raster scanning pattern is a time consuming procedure, especially when the region of interest is non regular or only a very small part of the rectangular boundary area. Figure 2.5 shows an AFM image of a DNA sample which has the same ROI problem discussed in section 2.2, Figure 2.2 (a). In order to get the AFM image of the DNA, the AFM has to scan the whole rectangular area.

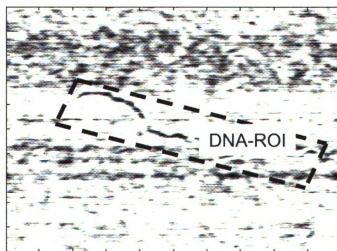


**Figure 2.5 AFM image of DNA structure, Courtesy J. Reed, UCLA**

In the normal scanning operation, the SPM uses the same scan speed for the whole image. In the DNA image, the actual DNA structure is only a very small part of the whole image. It is therefore very wasteful to use the SPM to collect high resolution data in the background region. If the SPM can automatically use high scan speed in the background area and only use low scan speed in the region of interest, the system can be utilized more effectively. The total area scan time can be decreased thereby increasing the overall efficiency and scan speed for samples.

### **2.2.2 Scanning Parameters Optimization**

In SPM system a sharp tip is used to scan across the sample. The scan parameters such as scan speed, set point, scan angle control the quality of scan image. Since the shape of the tip is not symmetric in each direction, the scan angle is known to have a significant effect in optimizing imaging conditions. The system should generate the scan plan based on different scan angle and find the optimized scan angle.

Optimized scan angle also can help to reduce the image artifact. As discussed in section 2.1.1, the AFM tip-sample interaction is caused by the summation of all possible Coulomb forces between the tip and the sample, summed along the physical structure of the tip and a local region of the sample surface. These forces can introduce distortions into the information that represents some given aspect of the sample surface. One of the physics based approach for enhancing accuracy of measurements is to reduce the tip-sample interaction for increasing the accuracy of surface height which in turn means to reduce the tip-sample contact region. The optimized scan angle can reduce the contact area between the tip and sample.

## 2.3 Challenges and Opportunities for Data Fusion

AFMs provide several types of data. In contact mode, the distance that the scanner moves vertically at each  $(x,y)$  data point is stored in the computer to form a topographic (height) image of the sample surface. The deflection of the cantilever at each data point is also stored as a deflection image. The deflection image will give more local detail. The lateral torsioning of the cantilever at each data point is also stored as the friction image. The friction image can provide a measure of comparative surface roughness. In contact mode, SPM system also provides the friction image which shows the lateral force at each  $(x, y)$  point.

In the tapping mode, the tip is oscillating above the sample at or near its resonance frequency. The tip lightly “taps” on the sample surface during scanning, contacting the surface at the bottom of its swing. In addition to a ‘sharper’ height image with less distortion due to lateral torsioning, the phase shift of the cantilever oscillation, is also stored as a phase image and provides valuable information that detects variations in composition, adhesion, friction, viscoelasticity, and numerous other properties.

AFM is also capable of even more complementary operational modes which provide information on other surface properties, such as stiffness, hardness, friction, or elasticity. It can record the amount of force felt by the cantilever as the probe tip is brought close to — and even indented into — a sample surface and then pulled away. This technique can be used to measure the long range attractive or repulsive forces between the probe tip and the sample surface, revealing local chemical and mechanical properties like adhesion and elasticity, and even thickness of adsorbed molecular layers or bond rupture lengths.

While all these information provide different properties of the sample, the system does not present a comprehensive map of the object. By virtue of this multi-modal nature of the data, the AFM serves as an ideal candidate for data fusion applications. Data fusion techniques can be utilized to synergistically combine mechanical, topographical and curvature information into a composite picture representative of a specimen.

## Chapter 3 Development of SPRM

The traditional raster scanning procedure performed in scanning probe microscopy (SPM) is an extremely time consuming procedure, especially when the area of interest is non regular and/or occupies a very small part of the rectangle scan area selected. While in the traditional SPM, the tip scans inside a regular rectangle area following a raster pattern, in this thesis we develop a new and innovative capabilities for direct investigations of the specific sites and interactions that control healthy or dysfunctional cell regulation. We propose a novel recognition and motion control scan system, scan probe recognition microscopy (SPRM) that achieves the goal of site-specific.

The key underlying idea is to replace the current x-y raster scan with a machine-based auto-focus strategy that allows scanning, data collection and subsequent processing to be restricted to site-specific investigation. Figure 3.1 shows the schematic block diagram of the SPRM dynamic scanning system in its prototype implementation.

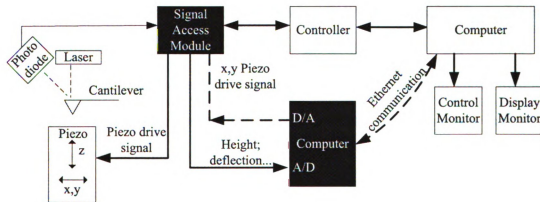


Figure 3.1 Block diagram of the dynamic scanning system.

The SPRM prototype system consists of three major components: the scanning probe microscope system; Signal Access Module (SAM); Data processing computer. Detailed

information about the basic SPM system has been discussed in Chapter 1. The SAM enables SPM users to make direct connections to the microscope's electronics. Figure 3.2 shows a photograph of the SAM used in our system.



**Figure 3.2 Signal Access Module [60]**

The SAM is provided with BNC connectors which interface with most standard laboratory instruments. Twenty-five separate SPM signals are available. Toggle switches enable the user to switch each line separately between a normal, uninterrupted configuration and an external input signal. Output BNC connectors permit monitoring of both conditioned and uninterrupted signals for use in experiments.

The data processing computer is used to collect the data from SAM via an Analog-to-Digital converter, analyze the data and generate a scan plan. There are two ways to control the SPM tip motion. One method is through the signal access module. In this method, the data processing computer directly generates the piezo drive signals which are high voltage signals. The signals are added directly in the piezo via the SAM. Since the voltage range of the piezo drive signal is between -220v and +220v, this method requires very careful attention. A second method is to use the SPM built-in lithography command

to control the tip movement. The nanolithography feature allows tip motion in nano scale increments. In our research, we choose the second method and use the data processing computer to analyze the data and generate appropriate scan control commands.

Site specific scan plan generation can be accomplished either in off-line processing or on-line processing mode. In the off-line processing mode SPRM first scans the entire sample area at a coarse resolution. The collected data are processed off-line to determine the region of interest and a scan plan is generated which will guide the tip to scan inside the region of interest (ROI) in a subsequent scan at a higher resolution. In the on-line processing mode the pattern recognition and scan plan generation are performed as the data is acquired. The algorithm analyzes the current collected data and generates the scan command for the next scan step. In either strategy, the two major steps are ROI recognition and motion control.

### **3.1 Off-line Processing Mode**

In the off-line processing mode, the SPM first scans a large area in the sample which includes the region of interest (ROI) and obtains a coarse resolution image of the specimen. The SPM measurements of sample features are processed to recognize the different landmarks and their locations in terms of integer pixel coordinates, which in turn can be converted to coordinates in nanometers. These coordinates are used to redirect the tip to the ROI for further investigation. The overall recognition algorithm consists of: (i) preprocessing for enhancing image quality; (ii) ROI detection; (iii) scan plan generation.

In a conventional AFM raster-scanned image, not all data points represent an ROI, ie a cell, a DNA strand etc. Figure 3.3 shows AFM image of DNA molecules. The overall measured image can be segmented into background (substrate) and ROI (DNA object) pixels. These are superimposed with noise and artifacts due to operational parameters. Hence it is important to process the AFM image data to remove noise to facilitate identification of the ROI. Histogram equalization is applied in order to increase local contrast of the image.

Based on the shape of structure that is being imaged, two different algorithms are used to detect the ROI: multi scale analysis and skeleton analysis.

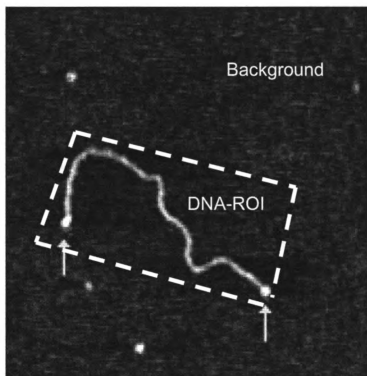


Figure 3.3 AFM image of DNA molecules (Image size:  $0.5 \times 0.5 \mu\text{m}^2$ ) [61]

### 3.1.1 Multi Scale Analysis

Images in general consist of several scales and features in the image can be broadly classified in terms of its scale. For instance, a cell belongs to larger scale than the nucleus, and a receptor site belongs to smaller scale than a nucleus. A multi scale analysis exploits the scale information to allow the object to be analyzed at different resolution levels. In this research, multiscale analysis is implemented using the continuous wavelet transformation. A continuous wavelet transform is a scale based two-dimensional transformation defined as:

$$W(\sigma, \tau_1, \tau_2) = \frac{1}{\sigma} \iint f(x, y) \psi^* \left( \frac{x - \tau_1}{\sigma}, \frac{y - \tau_2}{\sigma} \right) dx dy \quad (3-1)$$

where  $\sigma$  is the scale parameter,  $\tau_1$  and  $\tau_2$  are the translation parameters in the  $x$  and  $y$  directions,  $*$  denotes complex conjugation, and  $\psi$  is the mother wavelet function. We use a differential Gaussian function mother wavelet because this function enhances edge information. Figure 3.4 shows the results of offline processing. A rectangular region of interest (ROI) is represented in terms of coordinates  $\{(x_{\min}, y_{\min}), (x_{\max}, y_{\max})\}$ .

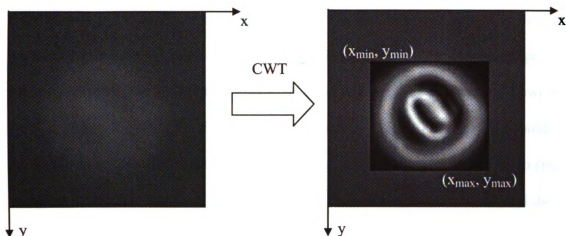


**Figure 3.4 Result of offline processing [62]**

Once a rectangular region of interest in the image has been identified for further investigation, the coordinates of the boundary pixels are obtained and used to control the tip to perform a raster scan only inside the region of interest. The SPRM automatically finds the ROI, scans inside the ROI and provides continuous, reliable and high resolution information of ROI. However the off-line processing mode cannot provide the reliable ROI coordinate information if the shape or location of sample is dynamically changing during the scanning process.

### **3.1.2 Skeleton analysis**

In the AFM image of DNA, as shown in Figure 3.5, the actual DNA structure is a long thin string and occupies a very small part of the whole image of scanned region. It is therefore wasteful to use the SPM to collect high resolution data in the background region. On detecting of the ROI, the SPM is controlled to scan only inside the ROI with high

resolution to save operation time and obtain accurate, high resolution data. Also as previously discussed in Chapter 2, the scan angle controls the quality of scan image. Since the shape of the tip is not symmetric in each direction, the scan angle is known to have a significant effect in optimizing imaging conditions. The SPRM system should ideally generate scan plans using different scan angles and find the optimized scan angle.

By obtaining the orientation information of the DNA chain, we can also control the scan angle to maximize image accuracy. In this thesis, skeletonization algorithm is used to detect both location and orientation information. The notion of skeleton was introduced by H. Blum as a result of the Medial Axis Transform (MAT) or Symmetry Axis Transform (SAT) [63, 64]. The skeleton points are defined as centers of maximal circles contained in the original object. Three techniques have been developed to generate skeletons or medial axes, namely, morphological thinning [65], distance transform [66] and Voronoi diagram [67].

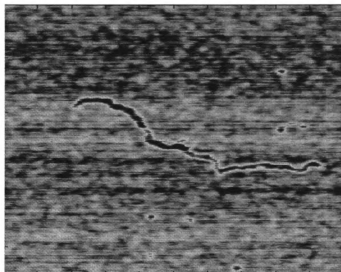


**Figure 3.5 AFM image of DNA structure, Courtesy J. Reed, UCLA**

Morphological thinning is a layer by layer erosion method, identifying points whose removal does not affect the object's topology. Although this technique is relatively straightforward, the skeleton generated by thinning methods does not always form a connected object. Distance transform method includes three steps. The data is first converted into a binary image with the object (1) and background (0). In the distance map, each pixel represents the distance to the nearest feature element (edge pixel). Skeleton points are defined along the singularities (ridges). However the detection of singularities in the distance map is difficult. A third class of methods calculate Voronoi diagram of the discrete samples of the boundary. The Voronoi diagram of a set of discrete points (defined as generating points) in a given space is a partition of the given space so that each partition contains only one generating points and all points which are nearer to this generating point than any other generating points. If we choose the boundary points as generating points and the number of the generating points goes near to infinite, the Voronoi diagram of the these boundary points converges to the skeleton. This method can generate an accurate connected skeleton. However it is complex to implement and is computationally expensive.

This research develops a skeletonization algorithm using the Contour-Pruned skeletonization algorithm [68]. Figure 3.6 shows the flow chart of the Contour-Pruned skeletonization algorithm.

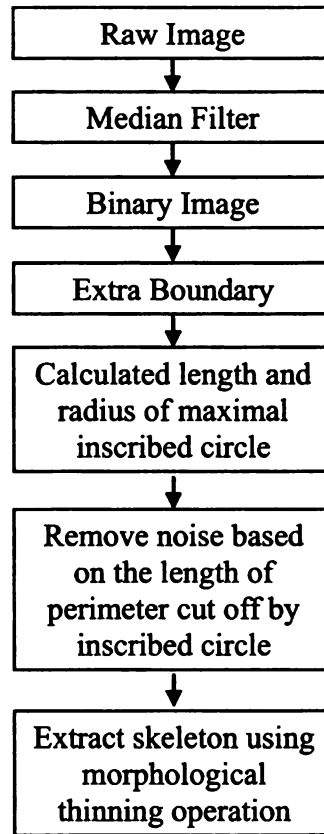


**Figure 3.6 Flow chart of the Contour-Pruned skeletonization algorithm**

A median filter is first used to remove the salt and pepper noise. The filtered image is then converted into the binary image in which the boundaries of the DNA chains are easily extracted. Inside the boundary of DNA chain, the distance of each pixel to the nearest edge pixel is calculated to obtain the radius of the maximal inscribed circle centered at that pixel. The boundary points of the object are labeled clockwise. The perimeter of the object is defined by the difference between the first and last boundary pixels which is the same as the number of boundary pixels. The length of perimeter cut by the inscribed circle is defined as the difference between the perimeter and the largest gap between the inscribed circle's contact points. Figure 3.7 shows an example of the inscribed circle in the object. In Figure 3.7, the length of the perimeter is equal to 20. The

inscribed circle has three contact points at boundary nodes 5, 9 and 17. The gaps between these contact points are 4, 8 and 8. The length of perimeter cut by the inscribed circle is defined as

$$P_{cutoff} = P_{boundary} - \max(gap) = 20 - 8 = 12 \quad (3-2)$$

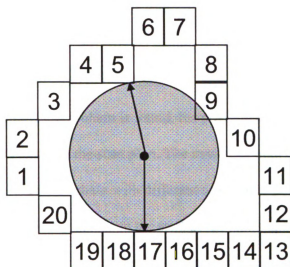


**Figure 3.7 Object and inscribed circle**

This procedure is repeated for each pixel inside the boundary and a new image is generated in which each pixel represents the length of perimeter inside the inscribed circle. Figure 3.8 (c) shows the map of the radius of the maximal inscribed circle in the DNA image and Figure 3.8 (d) shows the image of length of perimeter cut off by the inscribed circle in each pixel.

The pruning algorithm is implemented by using the length of the perimeter cut by the inscribed circle. In the image of length of perimeter cut by the inscribed circle, a threshold value is manually set to remove the noise pixel which typically has a small segment of the perimeter length within the circle. A morphological thinning operation is used to find the skeleton in the image of the perimeter lengths cut by each inscribed circle.

This is also the skeleton of the same DNA chain. Figure 3.8 (f) shows the skeleton superimposed on the DNA image.

The advantage of this method is the pruning technique, which is based on the length of perimeter cut by a maximal inscribed circle. This method makes it easy to prune noisy skeleton branches while leaving significant features intact. Figure 3.9 shows the results of skeletonization with and without the pruning technique. As is seen, the pruning technique provides a more accurate skeleton of the object.

Once the skeleton of the DNA chain is found, the position and orientation of the DNA chain can be defined in terms of the scan plan. The new scan plan then controls the tip to perform a scan around the DNA chain with different scan angle between the tip and DNA chain. The SPRM automatically moves to the start of the DNA chain, scans cross the DNA chain and provides continuous, high resolution information image data. By controlling tip scan angle as it crosses the DNA strand, the SPRM can provide more reliable and detailed information. However, as mentioned before in the case of multi scale off-line processing, this method cannot provide the reliable ROI coordinate information if the shape or location of target and hence ROI is continually changing.

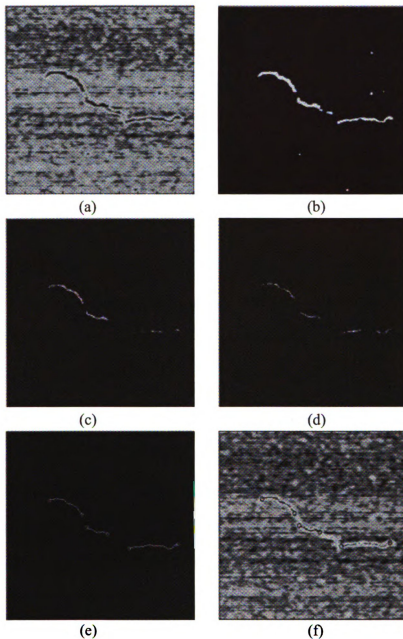


**Figure 3.8** Skeletonization results: (a) raw DNA image; (b) binary image; (c) radius of the maximum inscribed circle; (d) image of length of segmented perimeter; (e) skeleton image; (f) skeleton image shown in original DNA image.

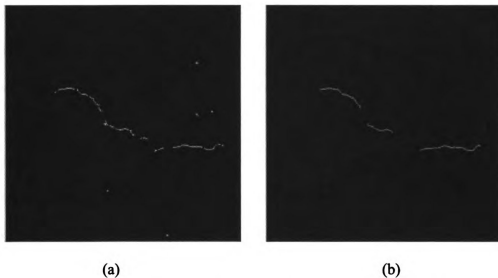


**Figure 3.9 Skeleton of the DNA image (a) without pruning (b) with pruning**

### **3.2 Online Scanning Mode**

Unlike the off-line processing mode which requires a low resolution pre-scan image of the entire scan area prior to identifying the ROI, the online scanning mode implements the recognition operation in real time. The ROI recognition algorithm and scan plan generation algorithm run in conjunction to adaptively detected features of the ROI and use these to control the tip motion to get high a resolution image of the ROI.

#### **3.2.1 Online Scan Plan Generation**

Unlike the off-line processing mode which require low resolution pre-scan image of the entire scan area before recognition of the ROI, the online scanning mode implements the recognition operation in the real time. The ROI recognition algorithm and scan plan generation algorithm run in conjunction to adaptively detect features of the ROI and to control the tip motion to get high a resolution image of the ROI.

In online scanning mode there are two types of scan commands, namely, fine resolution scan and coarse resolution scan. The fine resolution scan command controls are used when the tip scans inside the ROI where a fine or small step size and low scan rate are used to get a high resolution image. The coarse resolution scan control commands are used to scan the background region where a large step size and fast scan rate are used to save scan time. The resultant image will have high resolution in the ROI and low resolution in the background region [69, 70].

Two types of online scan plans are proposed for addressing specific applications.

1. Multi ROI scan plan
2. Single ROI scan plan

The first type of online scan plan is multi-ROI scan plan. The flow chart of the multi-ROI scan plan is shown in Figure 3.10. This scan plan also starts with the coarse resolution scan. The system begins from the top left corner of the scan area with the initial coarse resolution (rough) scan command. Data acquired in the coarse resolution scan is processed for ROI detection. Once the recognition algorithm detects an ROI, the system stops the rough scan, stores the coordinate of the last point on the coarse scan. The fine resolution scan procedure is started from the upper left corner and the fine scan command is used to get the high resolution image within the ROI. After completing the scan of the current ROI, the system resumes the coarse scan from the stored coarse scan point. When the system encounters the second ROI the above process is repeated to get the high resolution image of the second ROI. This multi resolution scan procedure continues until the tip reaches the scan size limit.

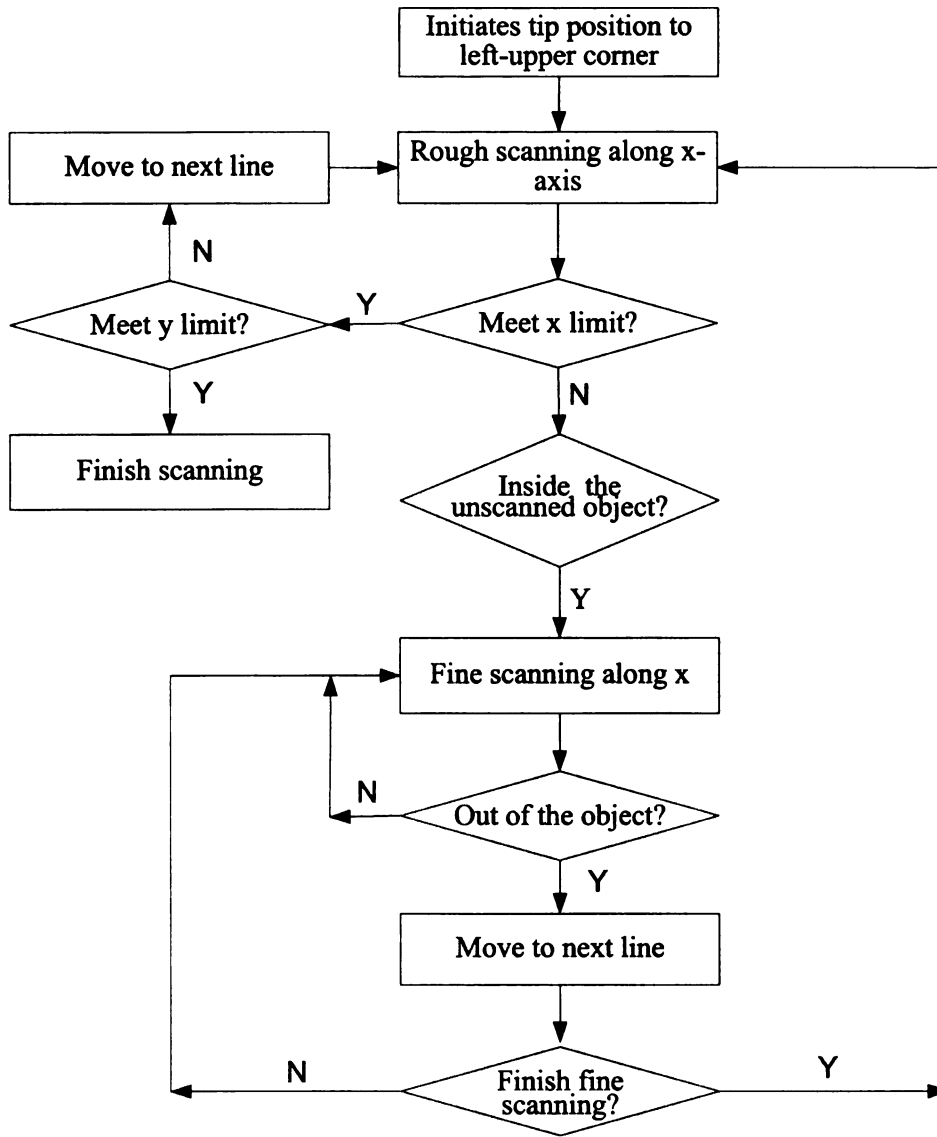
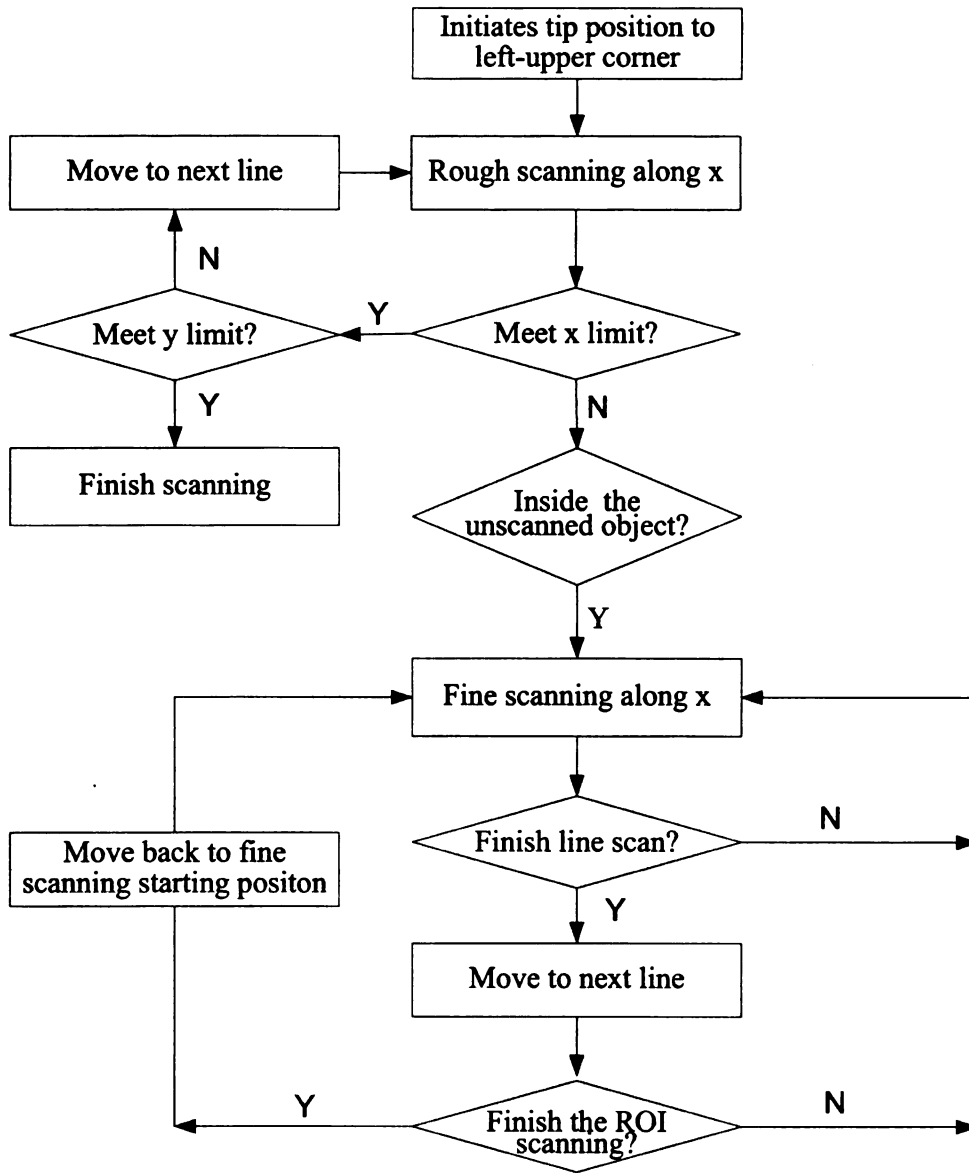


Figure 3.10 Online multi-ROI scan plan flowchart



**Figure 3.11 Schematic of single ROI scanning mode**

In order to study small dynamic changes in a specific site, for example, the dynamics of living cell structures, a single ROI scan plan is generated. In the single ROI mode, once the system detects an ROI, the scan will auto-track within the ROI and provides continuous reliable real-time detail information of the living cell's dynamic processes. Figure 3.11 shows the flow chart of the continuous dynamic scanning mode. In

the single ROI scan plan, the SPRM starts with coarse resolution scanning until the ROI (cell structure) is detected. Once the system detects the ROI, the SPRM will initiate the fine resolution scan within the ROI. After the ROI scan is completed, instead of resuming the coarse scan, system will re-scan the ROI in the reverse direction to continue collecting high resolution information inside the current ROI to track real time dynamic changes in the ROI. This process continues until a pre-set condition is reached.

### 3.2.2 Fine Resolution Scan Plan

In the fine resolution scan stage, the system uses a smaller step size and appropriate scan speed to control the SPM tip movement. The tip follows the raster scan pattern with variable fast axis length. Fine resolution scan plan is operated in two modes, namely with prediction and without prediction.

#### 3.2.2.1 Fine Scan without Prediction

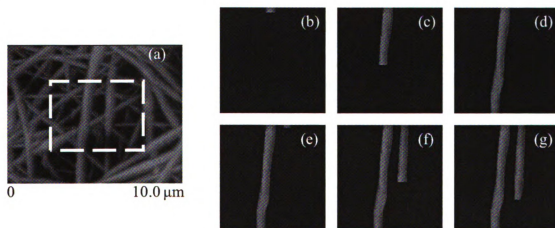


Figure 3.12 Fine scan without prediction (a) Conventional AFM image of the nanofiber (b) Coarse Scan picks up the first nanofiber; (c) Fine scan only on the first nanofiber (d) Finish the fine scan and return to coarse scan to find another region of interest; (e) Coarse Scan picks up the second nanofiber; (f) Fine scan only on the second nanofiber (g) Finish the high resolution fine scan only on the second nanofiber

In this mode, the ROIs are separated and there is no crossing over between two ROIs. Figure 3.12 shows the fine scan result of two ROIs which don't have crossing section. Once the system detects the ROI, it automatic focuses on the ROI and obtains a high resolution image of the ROI.

### 3.2.2.2 Fine Scan with Prediction

This scan mode is used in samples where the ROIs intersect each other. This is a particularly challenging problem where the tip is required to track a single fiber in a tissue scaffold, for example, as shown in Figure 3.13(a). In such a case we use the prior knowledge of the ROI to incorporate a prediction algorithm into the scan plan generation. Figure 3.13(a) shows a typical AFM image of the tissue scaffolding sample, where the ROIs are two intersecting nano fiber, identified by the arrow. Figure 3.13(b) shows the result of SPRM scan on one nanofiber passing through the intersection region and maintaining its original path.

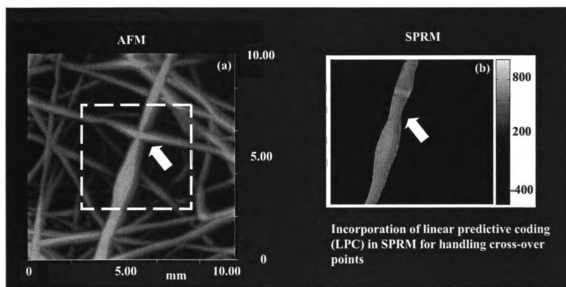


Figure 3.13 AFM image of the tissue scaffold sample with cross section area.

The prediction algorithm can, for example, be based on the linear regression of detected boundaries in the previous lines. The linear regression model is defined as

$$Y = aX + b + \varepsilon \quad (3-3)$$

where  $a$  is the slope,  $b$  is the intercept,  $\varepsilon$  is the “residual” random variable with zero mean and unknown variance  $\sigma^2$ ,  $\varepsilon \sim N(0, \sigma^2 I)$ . Using least squares method [71], we get the predicted boundary points in the next scan line.

Figure 3.14 shows SPRM image of tissue scaffold sample. 1(a)-(d) shows the SPRM scan plan generated without prediction. When the tip meets the intersection area, the scan plan in this case, jumps to the second fiber. While with the prediction algorithm the scan plan is as shown in 2(a)-(d). The tip scans past the intersection and stays on the original nano fiber to complete the data collection on the same nano fiber.

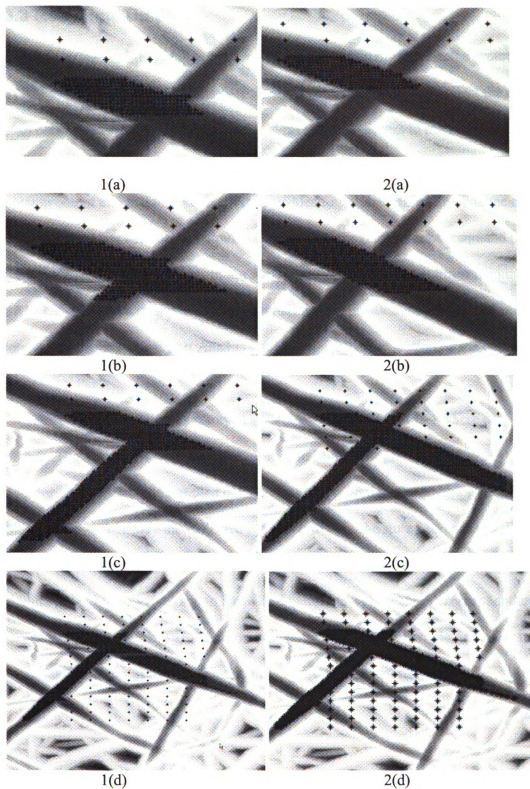


**Figure 3.14 SPRM scan plan of intersecting tissue scaffold sample. 1(a)-(d) shows SPRM scan without prediction; 2(a)-(d) shows corresponding SPRM scan with prediction**

### **3.3 Real Time Display**

When using the lithography command to control the tip movement, the prototype SPRM system uses the SAM to access the SPM controller system to collect the real time scan data as shown in Figure 3.1. The SAM provides the access to monitor most of the SPM signals such as set point, vertical deflection, lateral deflection, z position, STM preamp output etc. In addition, the SAM provides four user-defined low voltage analog output ports. User can set the output voltage in the lithography script command by using the command 'LithoSetOutput'. In our system we use the z position information. The SAM LV-Z output signal port is used to monitor the z position information. The SAM's low voltage output signal port Ana3 is used to trigger data collection by the data processing PC

The A/D card used in the prototype system is NI PCI-MIO-16E-4 where data length is 12 bits. The sampling rate is 1000 Hz. A custom Matlab program is used to control the A/D card and display the sampled data. Once the system finishes scanning the whole area, the program will display the collected data according to the stored coordinates file.

Figure 3.15 shows the SPRM scan image of tissue scaffold sample. Adaptive scanning enables SPRM to follow along an individual nanofiber even when it crosses another as shown in Figure 3.15 (b)-(g). Therefore, the three nanofibers, or whole nanofiber mesh becomes the region of interest. The output is generated in real time.

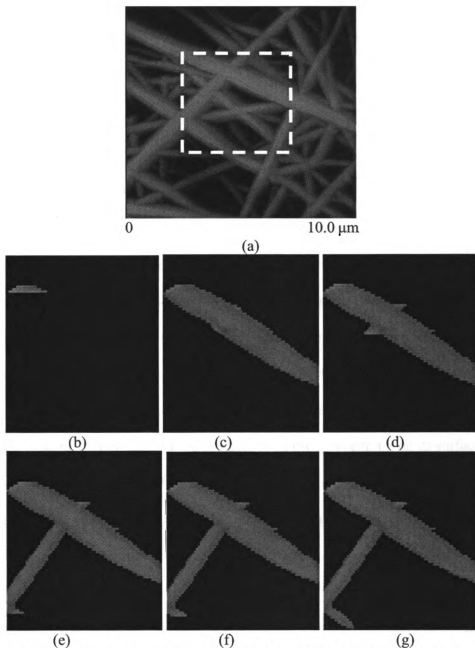


**Figure 3.15** SPRM scan image of the nanofiber. (a) Conventional AFM image of the nanofiber (b) Coarse Scan picks up the first nanofiber; (c) Finish high resolution fine scan only on the first nanofiber and return to coarse scan to find another region of interest; (d) Coarse Scan picks up the second nanofiber; (e) Finish the high resolution fine scan only on the second nanofiber and return to coarse scan to find another region of interest; (f) Coarse Scan picks up the third nanofiber; (g) Finish the high resolution fine scan only on the third nanofiber

## Chapter 4 Image Reconstruction Based on Geometric Deconvolution

In atomic force microscopy, a sharp tip is brought within nanometers of a sample surface by the z-motion of a piezoelectric scanner and held there by a z-feedback loop, as discussed in Chart1. The AFM tip-sample interaction is caused by the summation of all possible Coulomb forces between the tip and the sample, summed along the physical structure of the tip and over a local region of the sample surface. These forces can introduce distortions into the information that represents some given aspect of the sample surface. A tip shape introduces significant artifacts in the form of physically missed region information. In addition to missed regions, contact at any point other than the tip will result in an image smearing or dilation artifact. The sample surface may also contribute missing region and dilation artifacts of its own, depending on its surface roughness. In the case of a yielding sample, which is the case for cellular imaging, any deformation of the sample surface also dynamically changes the interaction. While this does not necessarily introduce a missed region artifact, it does mean that dynamic modeling of the contribution of each electrostatic force component in the tip-sample interaction becomes necessary [51-53]. The x-y raster motion takes place in the ambient environment within 10's of nanometers of the sample surface. A very common artifact is due to drag through a surface layer which introduces torsioning of the cantilever. When a tip is raised or lowered through the surface layer while maintaining its z-feedback condition, it feels vertical adhesive forces as well. Therefore, tip shape, surface roughness, surface environment and yielding surfaces can all result in information artifacts.

This chapter discusses the application of image processing techniques for deconvolving artifacts due to tip shape from the SPM measurements, whereas physics based methods for deconvolution are described in chapter 5.

## **4.1 Deconvolution in Atomic Force Microscopy**

In general, by modeling the AFM measured data as the output of a linear time invariant system, the surface measured by the AFM can be interpreted as the convolution of the sharp nanoscale surface features, with a transfer function that depends on the properties of the tip. When the tip properties are accurately known, the true image can be reconstructed by a linear deconvolution of the measured surface. Two of the most important factors that affect AFM resolution are the apex angle/radius and aspect ratio of the scanning tip. The first tips used by the inventors of the AFM were made by gluing sharply faceted diamond chips onto aluminum foil. Current tips are microfabricated from silicon or silicon nitride. Contact mode tips have an apex radius of curvature of about 25-30 nm and tapping or non contact mode tips have an apex radius of curvature of about 5-10 nm. Standard AFM research probes are tetrahedral with a  $35^\circ$  apex angle. The apex and aspect ratio may be modeled using a parabola to describe an overall tip shape. New tip shapes are under experimental development such as STING probe features additional narrow and long extratip provided by Mikromasch Corp. motivated by the issues discussed here. The redesign of the tip shape can reduce the imaging artifact but only deconvolution really addresses the problem.

This chapter concentrates on the effects of the tip shape convolved with the sample surface features, without considering the complexity introduced by the sample plasticity

or the surface environment. Two different classes of methods that are widely used in AFM image processing, namely, mathematical morphology [56] and Legendre transforms [57], are investigated. These techniques essentially serve to reconstruct, from the measured image, the sample surface if the tip geometry is known, or the tip geometry if the sample surface is known.

## 4.2 Morphological Processing Technique for Surface Reconstruction

The approach based on mathematical morphology for surface reconstruction, derived by Villarrubia [72] takes into account the effects of a finite probe tip size. It is assumed here that the image distortion is due to dilation of the image features by the finite area of the probe tip. The section below discusses the inherent relationship that exists between AFM image and the field of morphological image processing and describes a procedure to obtain the best possible reconstruction of the original sample surface using morphological deconvolution of the measured AFM image. The AFM image formation can be described in terms of morphological operations as below:

The notations in two dimensions are as follows:

- $s(x, y)$  : true sample surface
- $i(x', y')$  : measured AFM image surface
- $t(x-x', y-y')$  : arbitrary position of probe tip relative to the sample surface  $s(x, y)$ .

As the probe is moved, the height of the tip above the sample surface is the measured height data (Figure 4.1) and can be modeled as

$$i(x', y') = \min_x \{t(x - x', y - y') - s(x, y)\} \quad (4.1)$$

This is equivalent to the grayscale morphological operation of dilation

$$I = S \oplus P \quad (4.2)$$

where ‘ $\oplus$ ’ is dilation operator and set  $S = [(x,y,z) / z \leq s(x, y)]$ , is referred to as the ‘top’ of  $s(x, y)$ . Similarly  $I$  and  $P$  are sets corresponding to measured surface  $i(x', y')$  and the probe tip  $t(x, y)$ . When the probe apex is in contact with the sample, the AFM output measures the true height, i.e.  $i(x', y') = s(x, y)$ . However, when the point of contact is other than the probe apex, there is a distortion in the measured surface height and  $i(x', y') \neq s(x, y)$ . Figure 4.1 shows various translates of the parabolic tip,  $t(x-x', y-y')$  relative to the sample, the corresponding points of contact and the resultant measured surface. The dotted lines represent the simulated image obtained by the process of dilation which results in the rounding artifact seen in measured AFM data.

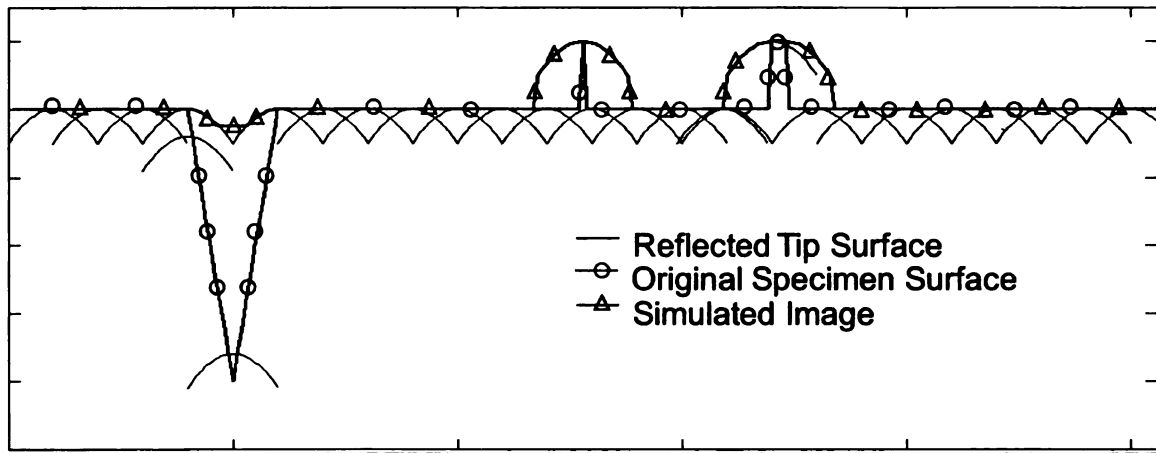


**Figure 4.1 Morphological dilation Model of AFM image data with sharp surface features ( Note : The tip surface is reflected about its origin in accordance with equation (4.3)) [73, 74]**

From the above image model, the algorithm for ‘deconvolving’ the distortion due to the tip shape can be obtained using a grayscale morphological erosion (inverse of dilation) operation defined as

$$S_e(x, y) = \min_{u,v} [i(x + u, y + v) - p(u, v)] \quad (4.3)$$

where the minimum operation is carried out over those coordinates where both tip and image are defined. In terms of the corresponding sets, defined above, equation (4.3) can be written as

$$S_r = I \ominus P \quad (4.4)$$

where  $\ominus$  denotes the morphological erosion operator and  $S_r$  is the reconstructed surface. Figure 4.2 depicts the process of erosion of measured surface with a parabolic tip surface. It is important to note that the reconstruction procedure described above can also be used for estimating an unknown tip surface from the measurement of a well characterized sample geometry as  $P_r = I \ominus S$ .

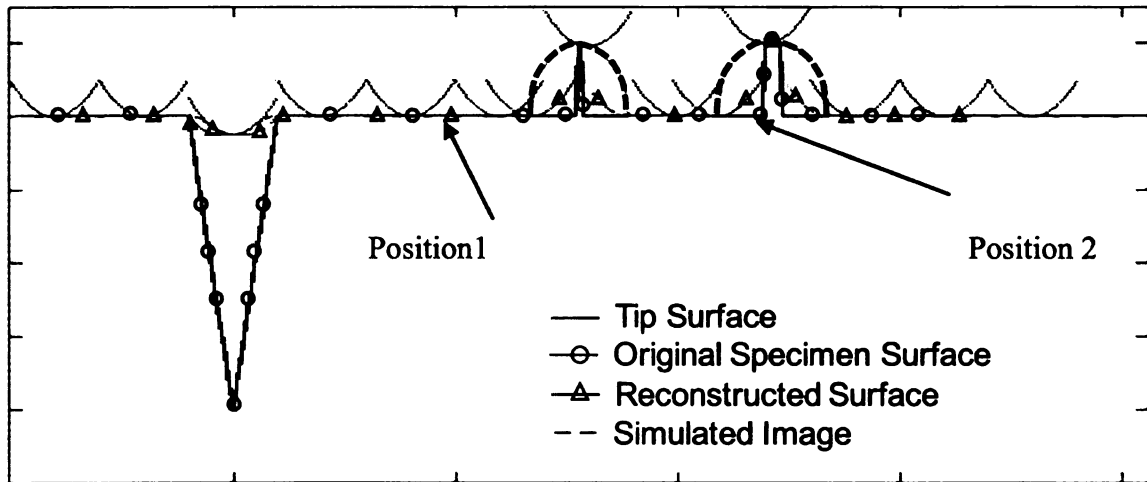


Figure 4.2 Surface reconstruction using grayscale morphological erosion[74].

Two properties from mathematical morphology are useful for showing that  $S_r$  is the least upper bound of  $S$ .

Property 1:  $(A \oplus B) \ominus B \supseteq A$

Property 2:  $(A \oplus B \ominus B) \oplus B = A \oplus B$

Property 1 implies that  $S_r \supseteq S$  and property 2 ensures that  $S_r$  is the least upper bound of  $S$ . Hence in the reconstructed image,  $S_r(x, y) = S(x, y)$  in some parts and  $S_r(x, y) >$

$S(x, y)$  in others. Figure 4.2 also indicates that narrow regions of the sample that are inaccessible to the tip cannot be reconstructed. In order to identify the regions in which the reconstruction is exact, Pingali and Jain [75] suggest procedures for constructing a certainty map  $c(x, y)$  as a measure of the confidence in the reconstructed surface. The certainty map  $c(x, y)$  is defined as below:

$$c(x, y) = 1 \text{ when } S_r(x, y) = S(x, y) \quad (4.5)$$

$$c(x, y) = 0 \text{ when } S_r(x, y) \neq S(x, y) \quad (4.6)$$

In Figure 4.2 we can see that at tip position 1,  $t(x, y)$  touches the reconstructed surface at one point,  $(x, y)$  where  $i(x, y) + t(u, v) = S_r(x + u, y + v)$ . Hence the certainty map in this location is set to 1. In position 2, the tip contacts the sample at multiple points and hence the certainty function is defined as  $c(x, y) = 0$  in this location. Figure 4.3 shows the performance of surface reconstruction obtained using morphological erosion on a simulated surface. The simulated AFM height image in Figure 4.3(b) was generated using morphological dilation operation on the known sample surface depicted in Figure 4.3(a).

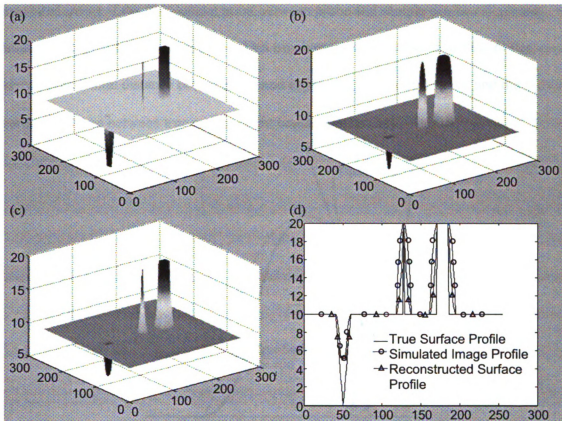


**Figure 4.3 Results of Morphological Processing (a) True (known) Specimen Surface (b) Simulated AFM Image (c) Reconstructed Specimen Surface (d) Profile Comparison**

### 4.3 Legendre Transform Technique for Sample Surface Reconstruction

An alternate approach for deconvolving the effect of tip shape/size is developed by Keller and is based on the Legendre transform of the measured image. This technique exploits the fact that the relationship between the measured surface and true surface is nonlinear as seen by the schematic in Figure 4.4. When the slope of the sample surface is large relative to that of the tip, the probe touches the sample at a point other than the nominal tip apex position. The AFM image consequently shows a surface that is smeared and corners that are more rounded. The true image can be reconstructed from the

measured image if the true contact point between probe and sample can be calculated from the image surface and tip shape. This involves the calculation of two quantities, namely, the lateral distance between true and apparent contact points ( $\Delta x$ ), and the vertical distance between true and apparent contact points ( $\Delta s$ ).

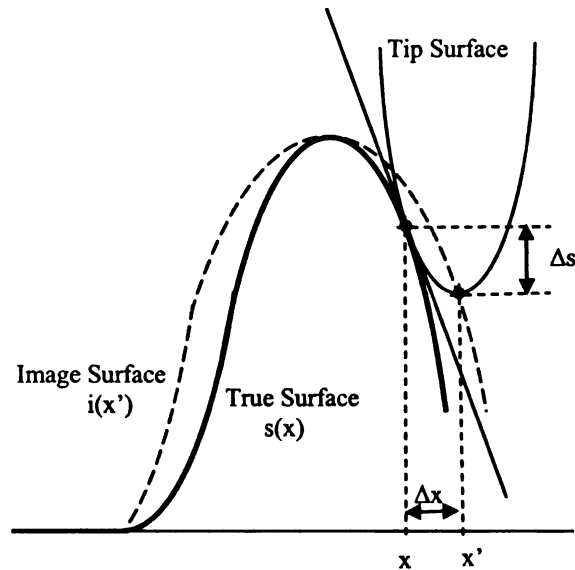


**Figure 4.4 A schematic of tip surface, sample surface and image surface [76]**

In one-dimension we define the following notation,

- $s(x)$  : true sample surface
- $i(x')$  : measured AFM image surface
- $\Delta x$  : lateral error between true point of contact  $x$  and apparent point of contact  $x'$
- $\Delta s$  : corresponding vertical error between  $x$  and  $x'$
- $t(\Delta x)$  : tip surface described as a function of  $\Delta x$

These equations can be easily extended to a two-dimensional image case in a straightforward manner. At the true point of contact the probe and sample surfaces have

the same tangent line so that the slope of the tip surface equals slope of the true sample surface, i.e.  $s(x)$  and  $t(\Delta x)$  have the same derivative at contact.

$$\frac{dt}{d\Delta x}(\Delta x) = \frac{ds}{dx}(x) \quad (4.7)$$

As the tip moves,  $x'$  changes and so does  $\Delta x$ , i.e.  $\Delta x \equiv \Delta x(x')$ .

Specifically,  $\Delta x = x - x'$  or  $x = x' + \Delta x(x')$ . Taking derivative of  $x$  w.r.  $t. x'$  we get

$$\frac{dx}{dx'} = 1 + \frac{d\Delta x}{dx'} \quad (4.8)$$

From the definition of true surface we have

$$s(x) = i(x') + \Delta s(x') \quad (4.9)$$

where  $\Delta s(x') = t(\Delta x(x'))$

The derivative of equation (4.9) w. r. t.  $x'$  is given by

$$\frac{ds}{dx'} = \frac{di(x')}{dx'} + \frac{d\Delta s(x')}{dx'} \quad (4.10)$$

Using equations (4.8) and (4.9) in (4.10), we get

$$\frac{di(x')}{dx'} = \frac{ds}{dx} \frac{dx}{dx'} - \frac{d\Delta s(x')}{dx'} = \frac{ds}{dx} \left( \frac{dx}{dx'} - \frac{d\Delta x}{dx'} \right)$$

which results in

$$\frac{di(x')}{dx'} = \frac{ds}{dx} \quad (4.11)$$

Equation (4.11) indicates that the slope of the measured image at apparent point of contact  $x'$  is equal to the slope of the true sample surface at the point of contact  $x$ .

Equation (4.11) can be inverted to determine  $\Delta x(x')$  and hence  $\Delta s(x')$  if  $t(\Delta x)$  is known.

These values are then substituted in Equation (4.9) to reconstruct the true surface  $s(x)$ . A

quantitative measure of the distortion due to probe surface is defined to be equal to  $\frac{d\Delta x}{dx'}$ ,

which can be calculated as

$$\frac{d\Delta x}{dx'} = \frac{d^2 i(x') / dx'^2}{d^2 t(\Delta x) / d\Delta x^2} \quad (4.12)$$

Equation (4.12) simply states that when the tip has a high curvature, the distortion is less and vice versa. In terms of Legendre transform the reconstruction can be expressed in a very simple manner. The Legendre Transform,  $L(f(x))$  of a function  $f(x)$  is defined as the intercept on y-axis made by the tangent to  $f(x)$  at  $x$  which can be expressed as [77]:

$$L(f(x)) = b(m) = f(x(m)) - mx(m) \quad (4.13)$$

where  $m$  is the slope defined by  $m = \frac{df(x)}{dx}$  and  $x(m)$  is the solution of  $m = \frac{df}{dx}(x(m))$ .

The inverse Legendre transform for computing  $f(x)$  from  $b(m)$  is then given by

$$f(x) = m(x)x + b(m(x)) \quad (4.14)$$

where  $x$  is found according to  $-x = \frac{db(m)}{dm}$  and  $m(x)$  is the solution of

$$-x = \frac{db}{dm}(m(x)).$$

From Figure 4.5 we can see that the Legendre transforms of true surface (bold), measured surface (dotted) and probe tip surface are related by

$$L[s(x)] = L[i(x')] + L[t(\Delta x)] \quad (4.15)$$

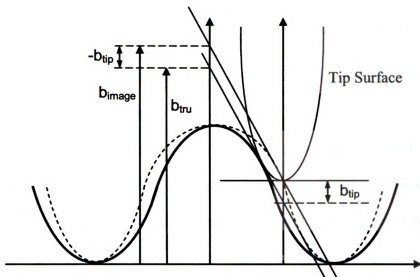


**Figure 4.5 Relationship between the Legendre Transform of the sample surface (black bold), image surface (dotted) and tip surface [73]**

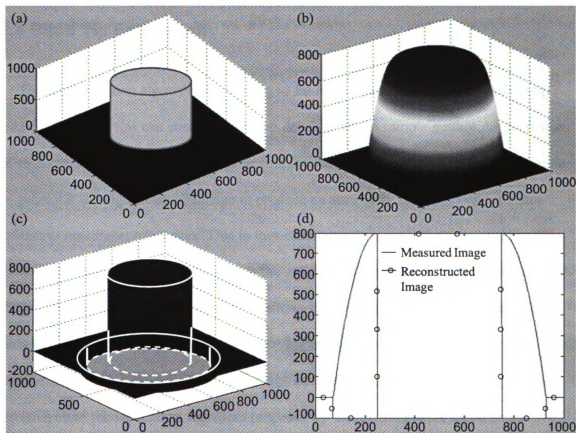


**Figure 4.6 Application of the Legendre transform to an artificial AFM height image(a) True surface image of a cylindrical structure of 500nm diameter and 800nm high. (b) Simulated AFM image using 20nm parabolic tip. (c) Reconstructed image. (d) Profiles of measured and reconstructed images [73].**

where all the transforms are evaluated at  $m = \frac{di}{dx'}$ . The true surface is therefore obtained simply by inverse Legendre transformation, which is equivalent to the operations in equations (4.7) through (4.11).

Figure 4.6 shows the surface reconstruction that results from applying the Legendre transform to simulated AFM height data of a known surface profile and a known tip geometry using linear interpolation in the inaccessible region. The simulated image in Figure 4.6 (b) is obtained by the morphological dilation procedure described in equation (4.2).

#### 4.4 Blind Tip Estimation

The reconstruction algorithms discussed so far require accurate knowledge of the tip surface. However tips can abrade or pick up debris from the sample surface during a scan. In such cases, the tip surface needs to be first estimated using a known calibration sample. In general it is a significant challenge to produce an accurately characterized reference artifact to nanometer tolerances. This in turn introduces an error in the estimated tip shape and hence we can at most estimate the upper and lower bounds of the actual tip shape. The upper bound of the tip surface allows the estimation of the lower bound of the sample surface with the measured image serving as the upper bound. Alternately the surface can be reconstructed using iterative blind deconvolution algorithms [78, 79]. The iterative blind reconstruction algorithm proposed by Villarrubia [78] is based on the rationale that the tip essentially serves to broaden any protrusion on the sample surface. Since the tip is assumed to be relatively narrow, independent features in the image can be

treated as separate images each of which sets an upper bound on the tip shape so that the true tip surface is sharper than the tightest of these bounds. Intersection of all the bounds results in the least blunt estimate of the tip that is consistent with the observed image. The iterative procedure for blind tip estimation is derived in [78] and is summarized below

Assume initial estimate for the probe tip surface  $P_0$ .

Locate features on the image surface.

$(i+1)^{th}$  iteration: Get a bound on the tip surface based on  $i^{th}$  image feature .

$P'_i(X) = P_i \cap (X - I)$  where  $x$  is the location of the feature of interest.

The  $(i+1)^{th}$  estimate is computed as

$$P_{i+1} = \bigcap [(I - x) \oplus P'_i(x)] \cap P_i \quad (4.16)$$

At convergence we have the resulting estimate for the tip surface as

$$P_R = \lim_{i \rightarrow \infty} P_i \quad (4.17)$$

The parameters involved in this algorithm are mainly the initial tip surface and initial values for the tip height, i.e. tip shape. It can be proved that each iteration produces a result that is smaller or equal to the preceding result. At convergence the final result gives a minimum upper bound of the true tip surface. Given an image and estimated tip geometry, the morphological erosion procedure is used for sample surface reconstruction according to equation (4.3). The performance of blind tip estimation depends strongly on the sharpness of the sample features.

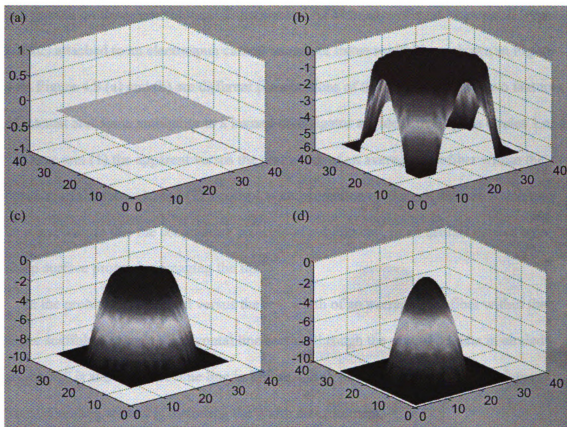


Figure 4.7 Blind tip estimation results at different iterations (a) initial guess,(b) 1st iteration,(c) 2<sup>nd</sup> iteration & (d) final estimate of the tip shape after convergence [73].

Typical results of blind tip estimation on synthetic data are shown in Figure 4.7. The coordinate system is chosen such that  $z = 0$  at the tip apex, hence setting all values to zero provides an initial upper bound as shown in Figure 4.7(a). Using features in the synthetic image in Figure 4.3(a), the blind estimation procedure results in the tip shape estimate shown in Figure 4.7(d).

#### 4.5 Example Applications of Deconvolution for Nanobiology

The application of the morphological deconvolution and Legendre transform approaches, without and with blind tip estimation are applied to an AFM measurement of

cell growth on tissue scaffolding. Experimental AFM images of a rat kidney cell (type NRK2) attached to an electrospun carbon nanofiber tissue scaffold are shown in Figure 4.8. Figure 4.8 (a) and (b) are different presentations of the same data set. Two features of interest and some ambiguity to a human investigator are identified by the circles 1 and 2. These are: (1) the apparent versus the real width of an average nanofiber within the tissue scaffold network, and (2) a conspicuous projection on the cell surface which may be a real feature due to the coagulating proteins of a dying cell, or an artifact caused by a sharp surface protrusion imaging the tip.

In the problem of apparent versus the real width of an average nanofiber within the tissue scaffold network, a horizontal line section through the raw AFM data in circled region “1” is shown as the blue line in Figure 4.9(a), and it indicates that a tip-shape based rounding artifact is distorting the width measurement.

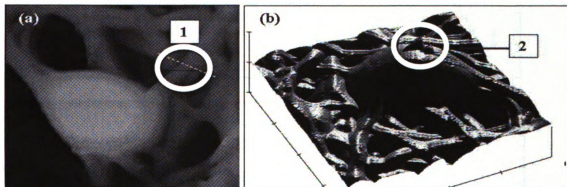


Figure 4.8 AFM images of NRK2 cell on polymer tissue scaffolding (a) top view and (b) surface plot. Two ambiguous features are circled (1) the actual width of the scaffold fibers and (2) a sharp feature on the cell surface [73].

Deconvolution of the image using both the (a) Legendre transform (LT) and (b) mathematical morphology (MM) methods was performed and the corresponding line sections through the nanofiber are shown next to the blue line in Figure 4.9(a). Legendre transform result is shown in black and the mathematical morphology deconvolution is in

red. The difference in the two results is due to the fact that in the LT method, the parabolic tip is of unlimited height, which gets wider with the height of the tip, whereas in MM the probe tip is of finite height. Consequently when the aspect ratio of feature is comparable with that of the tip, the two methods produce similar results but when the aspect ratio is larger than the tip's, the MM method produces a sharper estimate than the LT method as in the case of the nanofiber.

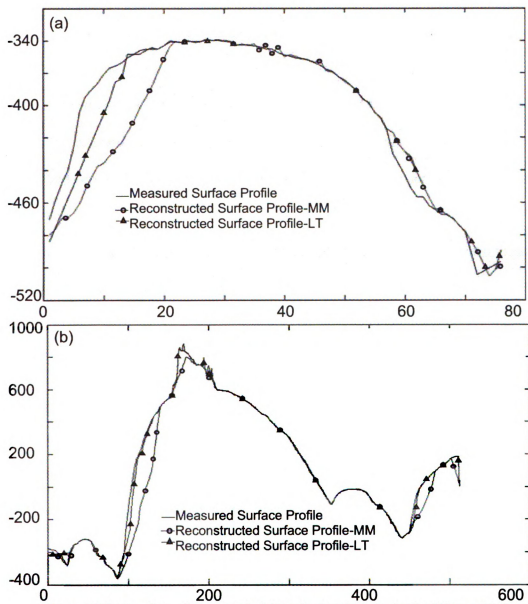


Figure 4.9 Comparison of line scans in (a) Region 1 and (b) Region 2 of Figure 4.8 showing deconvolution of fiber width [73].

The nanofiber widths were estimated as 354.25nm for the measured image, 334.01nm after deconvolution using LT and 328.42 nm after deconvolution using MM method.

Next we consider the conspicuous projection on the cell surface, circled region “2” in Figure 4.8. The Legendre transformation and the mathematical morphology deconvolutions are used in conjunction with blind tip estimation procedure to analyze the data. Figure 4.9 (b) shows horizontal line scans across region 2 in Figure 4.8 before and after deconvolution. The lack of improvement using LT deconvolution method implies that the feature is wider than the parabolic tip curvature estimated by the blind tip estimation procedure. Also, the difference in the LT and MM results indicate that the feature is taller than the assumed tip height (100nm). However the blind tip estimation described here is rather simplistic and yields a tip shape that depends on the sharpest feature in the image. Hence if the true tip shape is known, deconvolution would yield an impulse feature as the result, which in turn will resolve the ambiguity, stated in the beginning of this section.

## **4.6 Conclusions**

The restoration of image features in cellular and molecular images is a crucial problem in nanobiological investigations. The distortion of the measured image due to tip-sample interaction is a major challenge for nanoscale metrology and signal processing solutions are needed for increasing the accuracy and reliability of the data. Two existing approaches that are not physics based, have been described in detail for modeling the tip sample interaction from a topographical perspective, The approaches have been

implemented for reconstructing the sample surface, assuming the tip geometry. When the aspect ratio of feature is comparable with that of the tip, the two methods produce similar results but when the aspect ratio is larger than the tip's, the MM method produces a sharper estimate than the LT method. When the tip geometry is not known, blind tip estimations methods are needed for iterative estimations of tip and sample surfaces.

An alternate approach for AFM data restoration is physics based deconvolution. A key component of the physics based approach is the modeling and characterization of the tip and sample artifact sources for use in subsequent deconvolution algorithms. Attempts to model the tip sample interaction are presented in the next chapter.

## Chapter 5 Deconvolution based on the tip-sample interaction force model

The deconvolution methods discussed earlier focus mainly on effects due to tip size and geometry. For example, in contact mode AFM, the measured sample topography is assumed to depend only on the contact point between the tip and sample and independent of the geometry of the tip away the sample. However in atomic force microscopy, the AFM tip-sample interaction is caused by the summation of all possible Coulomb forces between the tip and the sample areas, summed along the physical structure of the tip and over a local region of the sample surface. Therefore a physics based model of the tip sample interaction should provide an estimate of the impulse response of the assumed linear, time invariant (LTI) system as summarized in Figure 5.1.

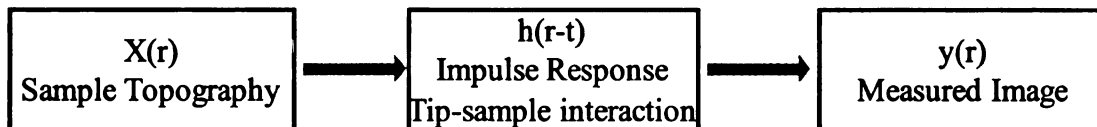


Figure 5.1 Schematic of the linear, time invariant system

The scanned image which is the output of the LTI system is shown as

$$y(r) = x(r) * h(r-t) \quad (5.1)$$

where \* represents the convolution operation.

A force model of the tip/sample interaction is used in the deconvolution algorithm described in this chapter.

### 5.1 Summary of Tip Sample Interaction

A variety of tip-surface interactions can be detected by an atomic force microscope, depending on the separation distance between tip and sample. The forces include the Van der Waals forces, electrostatic forces, mechanical contact force, capillary forces, and other variations of Coulomb forces. Coulomb forces are separation-dependent which translates into height-dependent in an SPM system. Figure 5.2 shows a force-distance curve which represents the force measured at different tip tip positions in z direction. In this figure, the tip-sample distance is divided broadly into to 3 regions. In region 1 or zero force region, the tip is far away from the sample and the mean value of the total force does not depend on the distance. Region 2 is the within 10's of nm of the sample surface before the tip contacts the sample. In this area the total force is attractive and the tip is pulled toward the sample surface. Van der Waals force is the dominant force in this region. The force curve situated to the left of contact point is region 3. The ion-ion interaction now dominates. The total force in this region is repulsive and the tip is pushed away the sample surface.

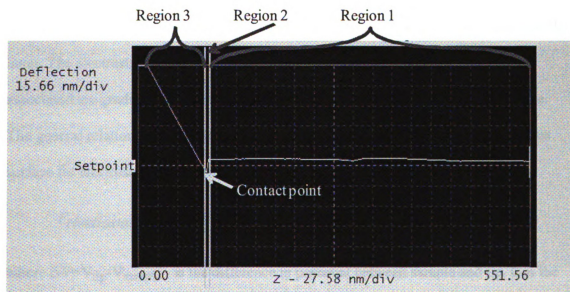


Figure 5.2 Force curve.

In Region 2 active Van der Waals force between atoms and /or molecules consists of three components: polarization, induction, and dispersion [6, 80]. Polarization refers to permanent dipole moments and is also known as the Keesom potential. Induction refers to the contribution of induced dipoles and is known as Debye potential. Dispersion is due to instantaneous fluctuations of dipoles on the tip and sample surfaces and is the most important contribution to Van der Waals force. The total Van der Waals force is the sum of the three terms. At distance of a few nanometers, Van der Waals forces are sufficiently strong to move macroscopic objects such as AFM cantilevers.

In Regions 2 and 3 electrostatic forces arise from the surface charges at interfaces. Ambient air use is the most common operation for AFM systems as there is almost no sample preparation required. However in ambient air condition, a humidity layer develops on the sample surface. Surface dissociation or adsorption of a charged species in water is very common due to the fact that water has a high dielectric constant. The surface charge is balanced by dissolved counter-ions which are attracted back to the surface by the electric field. Together the ions and the charged surface are known as the electric double layer. The electrostatic force is produced from the electrical double layers, and the associated ion gradients, as a charged probe is brought near a charged sample surface. The general relation describing the force experienced by a tip above the homogeneous surface for electrostatic interaction is described by

$$F_{electrostatic} = -\frac{1}{2}(\Delta V)^2 \frac{\partial C}{\partial z} \quad (5.2)$$

where  $\Delta V = V_{tip} - V_{sample}$ , is the difference in potential between sample and tip, C is the tip-sample capacitance as a function of separation z [6].

Capillary force is attributed to the water bridge between the tip and sample. Under ambient environmental conditions (room temperature, atmospheric pressure, and ambient air) the sample surface is invariably covered with a thin layer composed essentially of water and miscellaneous hydrocarbons. Considering the nano size contact region and assuming the tip end is a sphere of radius  $R$ , the adhesion capillary force can be calculated as [80]:

$$F \approx 4\pi R\gamma_L \cos \theta \quad (5.3)$$

where  $\gamma_L$  is the surface energy of the liquid,  $\theta$  is the angle of the tip-sample contact region.

After the tip ‘contacts’ the sample surface, meaning that the ion-ion repulsion now dominates the tip-sample interaction, the sample and/or tip are deformed. The force between the tip and sample may now be defined as mechanical contact force, which depends on both the material properties and geometry of the surface. Several theories describing the contact force have been developed by Hertz [81], Johnson-Kendall-Roberts (JKR) [82], and Derjaguin-Muller-Toporov (DMT) [83, 84]. The difference between the three models is the adhesion of the sample is neglected in the Hertz model whereas the DMT model considers it outside the contact region and JKR model calculates it inside the contact region.

In this work we consider only the attractive part of Van der Waals force as the main tip-sample interaction force which is applicable only in region 2 of the force-distance curve shown in Figure 5.2.

## 5.2 Van der Waals Force Model

D. Sarid [85] modeled the tip as a molecule, a sphere, or a cylinder in his work on Van der Waals force–distance relations. In Y. N. Moiseev et al published a paper [86], where the tip is modeled by a paraboloid. U. Hartmann [87] investigated the Van der Waals interaction between flat sample surface and sharp probes such as a cylinder, a paraboloid and a cone. J. L. Hutter and J. Bechhoefer [88] use the theoretical force–distance relation for a sphere above a plate which they compared with experimental data (although the tip in use is in fact close to a pyramid). In C. Argento and R. H. French’s paper [89] the tip images obtained from scanning electron microscopy suggests a parametric tip model which consists of a cylindrical part and a conical part covered by the spherical cap. The parametric tip model was also used for estimating the pyramidal tip shape. In this thesis, we use the same parametric tip model for calculating the Van der Waals force between the tip and sample.

If we only consider the attractive part of the Van der Waals force between the sample and tip, the potential energy of interaction  $w(d)$  is defined as:

$$w(d) = \frac{-C_{disp}}{d^6} \quad (5.4)$$

where  $C_{disp}$  is the interaction constant defined by London [90]. The interaction force between the sample and tip is given by the gradient of interaction potential defined as

$$\mathbf{f} = -\nabla w \quad (5.5)$$

Hamaker performed the integration of the interaction potential to compute the total interaction force between macroscopic bodies with three assumptions [91]:

- (1) Additivity: the total interaction can be obtained by the pairwise summation of the individual contributions;
- (2) Continuous medium: summation can be replaced by an integration over the volumes of the interacting bodies assuming that each 'molecule' occupies a volume  $dv$  with number density  $\rho$ ;
- (3) Constant material properties: the number density  $\rho$  and the interaction coefficient are constant over the volume of the bodies

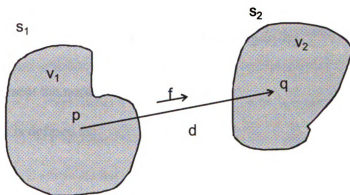


**Figure 5.3 Integration of the interaction force between two arbitrarily shaped bodies**

The total force between two arbitrary shaped bodies as shown in Figure 5.3 is given by:

$$F = \rho_1 \rho_2 \int_{V_2} \int_{V_1} f(d) dv_1 dv_2 = -\rho_1 \rho_2 \int_{V_2} \int_{V_1} \nabla w dv_1 dv_2 \quad (5.6)$$

where  $\rho_1$  and  $\rho_2$  are the number densities of bodies 1 and 2.

Details of the six-dimensional volume integration found in [92] is summarized below:

Using the gradient theorem ( $\int_V \nabla a dV = \oint_S a \mathbf{n} dS = \oint_S a \widehat{\mathbf{n}} dS$ ), we get

$$F = -\rho_1 \rho_2 \int_{V_2} \int_{V_1} \nabla w dv_1 dv_2 = -\rho_1 \rho_2 \int_{V_1} \int_{S_2} w \widehat{\mathbf{n}}_2 ds_2 dv_1 \quad (5.7)$$

where  $\mathbf{n}_2$  represents the normal to the body 2.

Let  $\mathbf{G}$  be a vector field defined as

$$\nabla \cdot \mathbf{G} = -w \quad (5.8)$$

Substituting equation (5.8) into (5.7), we get:

$$F = -\rho_1 \rho_2 \int_{V_2} \int_{V_1} \nabla w dv_1 dv_2 = -\rho_1 \rho_2 \int_{V_1} \int_{S_2} w \widehat{\mathbf{n}}_2 ds_2 dv_1 = \rho_1 \rho_2 \int_{V_1} \int_{S_2} (\nabla \cdot \mathbf{G}) \widehat{\mathbf{n}}_2 ds_2 dv_1 \quad (5.9)$$

Using the divergence theorem ( $\int_V \nabla \cdot \mathbf{A} dV = \oint_S \mathbf{A} \cdot d\mathbf{S} = \oint_S \mathbf{A} \cdot \widehat{\mathbf{n}} dS$ ), a double-surface integration is obtained as

$$F = \rho_1 \rho_2 \int_{V_1} \int_{S_2} (\nabla \cdot \mathbf{G}) \widehat{\mathbf{n}}_2 ds_2 dv_1 = \rho_1 \rho_2 \int_{S_2} \int_{S_1} (\mathbf{G} \cdot \widehat{\mathbf{n}}_1) \widehat{\mathbf{n}}_2 ds_1 ds_2 \quad (5.10)$$

where  $\mathbf{n}_1, \mathbf{n}_2$  represent the normals to bodies 1 and 2.

Hamaker constant is defined as:

$$A = \pi^2 C \rho_1 \rho_2 \quad (5.11)$$

Substituting equation (5.11) into (5.10), we get the Van der Waals force between two bodies as:

$$F = \rho_1 \rho_2 \int_{S_2} \int_{S_1} (\mathbf{G} \cdot \widehat{\mathbf{n}}_1) \widehat{\mathbf{n}}_2 ds_1 ds_2 = \frac{A}{c\pi^2} \int_{S_2} \int_{S_1} (\mathbf{G} \cdot \widehat{\mathbf{n}}_1) \widehat{\mathbf{n}}_2 ds_1 ds_2 \quad (5.12)$$

This integration calculates equivalent distributed forces over the surface of body 2 that represents a weighted average of the influence of the surface of body 1. The vector field  $\mathbf{G}$  is obtained from the interaction potential of two molecules. Consider the Van der Waals interaction potential

$$w(d) = \frac{-C_{disp}}{d^6} = \frac{-C_{disp}}{((\bar{x} \cdot \bar{x})^{1/2})^6} = \frac{-C_{disp}}{(\bar{x} \cdot \bar{x})^3} \quad (5.13)$$

where  $\vec{x}$  is the vector from a point in body 2 to a point in body 1. The solution of vector field  $\mathbf{G}$  in equation(5.8) is

$$\mathbf{G} = -\frac{C_{disp}\vec{x}}{3(\vec{x}\cdot\vec{x})^3} \quad (5.14)$$

The double surface integration is in general difficult to execute both analytically and numerically. To simply the problem, we will start with the simple sample, a flat sample surface and assume the parametric tip model.

### 5.2.1 Model Equation

The schematic of the tip model is shown in Figure 5.4.

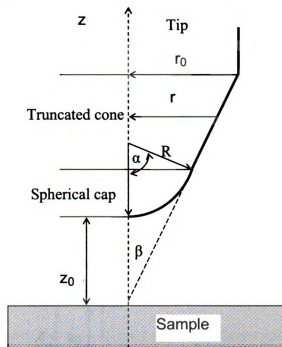


Figure 5.4 Schematic of the tip model.  $R$  is the radius of the spherical cap,  $\alpha$  is the angle include the spherical cap,  $\beta$  is the cone angle,  $z_0$  is the distance between the tip end and sample.

Let body 1 in equation (5.6) represents the sample and body 2, the tip. For a flat sample, we only need to calculate the vertical component of the interaction force since all

other components are zero due to symmetry of the problem. Therefore  $\mathbf{n}_1 = (0, 0, 1)$ ,

substituting equation (5.14) into equation (5.12)

$$F = \frac{A}{\pi^2} \int_{s_2} \left( \int_{s_1} \frac{z}{3(x^2 + y^2 + z^2)^3} dx dy \right) \widehat{\mathbf{n}}_2 ds_2 \quad (5.15)$$

In  $s_1$ , integrating over appropriate limits for  $x$  and  $y$ ,  $(-\infty, +\infty)$  yields

$$\int_{s_1} \frac{z}{3(x^2 + y^2 + z^2)^3} dx dy = \frac{\pi}{6z^3}, \quad (5.16)$$

Substituting the equation (5.16) into (5.15) we get the interaction force as:

$$F = \frac{A}{\pi^2} \int_{s_2} \frac{\pi}{6z^3} \widehat{\mathbf{n}}_2 ds_2 \quad (5.17)$$

Considering symmetry of the problem, we only need to integrate the vertical component of equation (5.17) over the tip surface. The integration over the surface is the sum of two parts, spherical cap and truncated cone.

For the spherical cap,  $z$  can be written as a function of  $z_0$  and  $\omega$  as shown in Figure 5.5:

$$z = z_0 + R - R \cos \omega \quad (5.18)$$

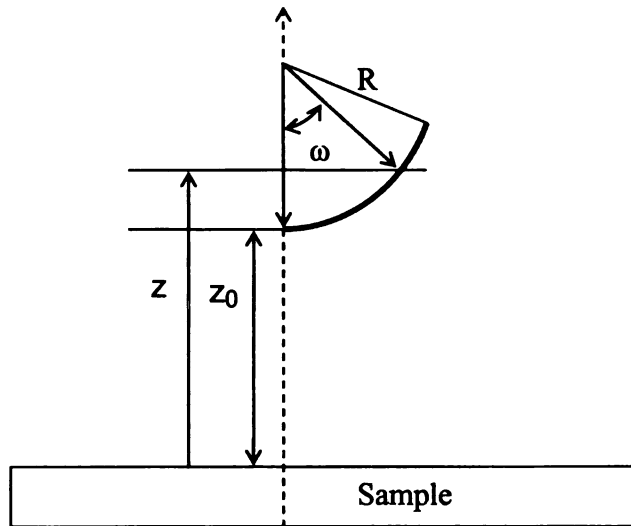


Figure 5.5 Schematic of the spherical cap

The component of the normal  $\mathbf{n}_2$  along the z direction is

$$n_{2z} = -\cos \omega \quad (5.19)$$

The infinitesimal element of the surface  $dS_2$  on the spherical surface is

$$dS_2 = 2\pi r R d\omega = 2\pi R^2 \sin \omega d\omega \quad (5.20)$$

The force contributed by the spherical cap is

$$F_z^{SC} = \frac{A}{\pi^2} \int_{S_2} \frac{\pi}{6z^3} \widehat{\mathbf{n}}_2 ds_2 = \frac{A}{\pi^2} \int_0^\alpha \frac{\pi}{6(z_0 + R - R \cos \omega)^3} (-\cos \omega) 2\pi R^2 \sin \omega d\omega$$

$$F_z^{SC} = \frac{AR^2(1 - \cos \alpha)(R \cos \alpha - z_0 \cos \alpha - R - z_0)}{6z_0^2(R + z_0 - R \cos \alpha)^2} \quad (5.21)$$

The second part is the force contributed by the cone area. Figure 5.6 shows the schematic of the truncated cone part.

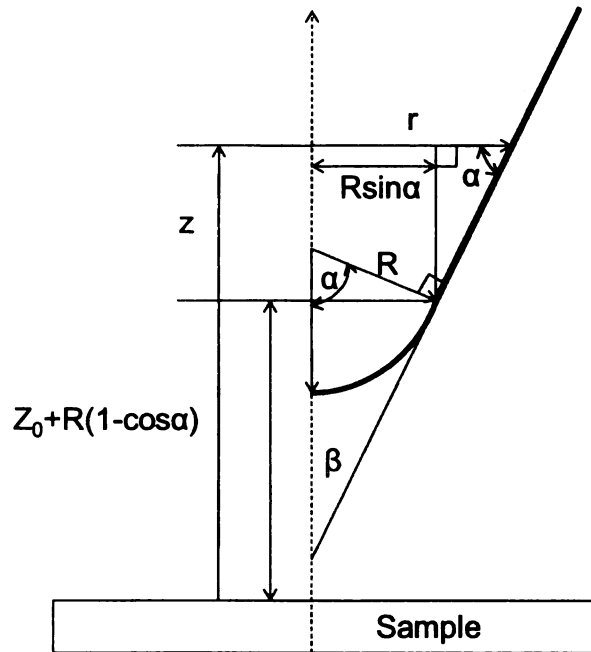


Figure 5.6 Schematic of the truncated cone

Expressing  $z$  as a function of  $r$  and  $z_0$

$$z = z_0 + R(1 - \cos \alpha) + \tan \alpha(r - R \sin \alpha) \quad (5.22)$$

The component of the normal  $\mathbf{n}_2$  along the z direction is

$$n_{2z} = -\cos \alpha \quad (5.23)$$

The infinitesimal element of surface  $dS_2$  on the spherical surface is

$$dS_2 = \frac{2\pi r}{\cos \alpha} dr \quad (5.24)$$

Substituting equation (5.22)-(5.24) into equation (5.17), we get the force contribution of the cone as:

$$F_z^{cone} = \frac{-A[z_0 \cos \alpha + R \cos \alpha - R(\cos 2\alpha)]}{6 \tan \alpha \sin \alpha (z_0 + R - R \cos \alpha)^2} \quad (5.25)$$

Adding equations (5.21) and (5.25), the total force between the tip and sample can be calculated as:

$$F_z = F_z^{sc} + F_z^{cone} = \frac{AR^2(1 - \cos \alpha)(R \cos \alpha - z_0 \cos \alpha - R - z_0)}{6z_0^2(R + z_0 - R \cos \alpha)^2} + \frac{-A[z_0 \cos \alpha + R \cos \alpha - R(\cos 2\alpha)]}{6 \tan \alpha \sin \alpha (z_0 + R - R \cos \alpha)^2} \quad (5.26)$$

where the Hamaker constant - A and the distance between the tip end and sample -  $z_0$  are unknown parameters. Reference [93] lists different methods proposed to calculate the Hamaker constant for different materials and configurations.

## 5.2.2 Parameter Estimation and Model Validation

In the final expression for tip-sample interaction force there are two unknown parameters. One unknown parameter is Hamaker constant  $A$  that depends on both the

sample and tip material properties. Another unknown parameter is the distance between the tip and sample,  $z_0$ . The distance between the tip and sample can be expressed as

$$z_0 = z - d_0 \quad (5.27)$$

where  $d_0$  is the position of contact point, and  $z$  is the position of the tip as illustrated in Figure 5.7. The unknown parameters are therefore  $A$  and  $d_0$  and equation (5.26) can be written as:

$$F_z = F_z^{SC} + F_z^{cone}$$

$$= \frac{AR^2(1 - \cos \alpha)[R \cos \alpha - (z - d_0) \cos \alpha - R - (z - d_0)]}{6(z - d_0)^2(R + z - d_0 - R \cos \alpha)^2} + \frac{-A[(z - d_0) \cos \alpha + R \cos \alpha - R(\cos 2\alpha)]}{6 \tan \alpha \sin \alpha (z - d_0 + R - R \cos \alpha)^2} \quad (5.28)$$

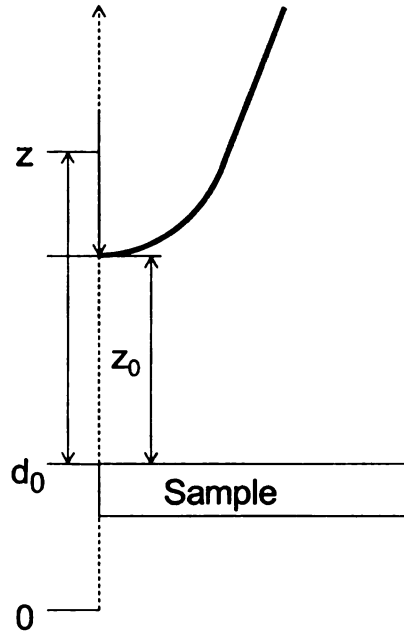


**Figure 5.7 schematic of the tip and sample position in z direction**

In this work, we use a least squares estimation procedure to determine  $A$  and  $z_0$  by minimizing the error in equation (5.29) with respect to unknown parameters  $A$  and  $z_0$

$$\sigma = \sqrt{\frac{1}{N} \sum_{i=1}^N (F_{van}^{th} - F_{van}^{exp})^2} \quad (5.29)$$

where sigma is the rms error,  $- F_{van}^{exp}$  is the measured force in region 2 and  $F_{van}^{th}$  is the model predicted force in equation (5.28).

Experiments for measurement and characterization of Van der Waals force with different tip-sample systems are reviewed for different systems in [94] and [95]. Here we follow the same measuring procedure as described in reference [96]. The experiment was performed using Veeco Instruments Nanoscope IIIa operated in ambient air with a standard silicon nitride tip. A gold layer was selected for evaluating the model since this is a standard surface used by many groups. The gold layer was a (500nm X 500 nm) photolithographically generated pattern of about 25 nm thickness, with about 5 nm buffer layer of Titanium on a silicon wafer surface with oxide layer. The sample was mounted on the scan stage. Then the piezoelectric scanner was extended along z-axes with an applied voltage, decreasing sample distance until contact. A plot of cantilever deflection is obtained as a function of sample displacement. The force corresponding to each value of deflection is calculated using Hooke's law. The above procedure was repeated 10 times to get 10 force curves at same position as shown in Figure 5.8(a). Each force curve contains 2048 experimental data points. In the experimental force curve, data points in region 1 are used to calculate the zero force as shown in Figure 5.8(b). The data points in region 2 shown in Figure 5.8(c) are used to estimate and validate the force equation (5.28).

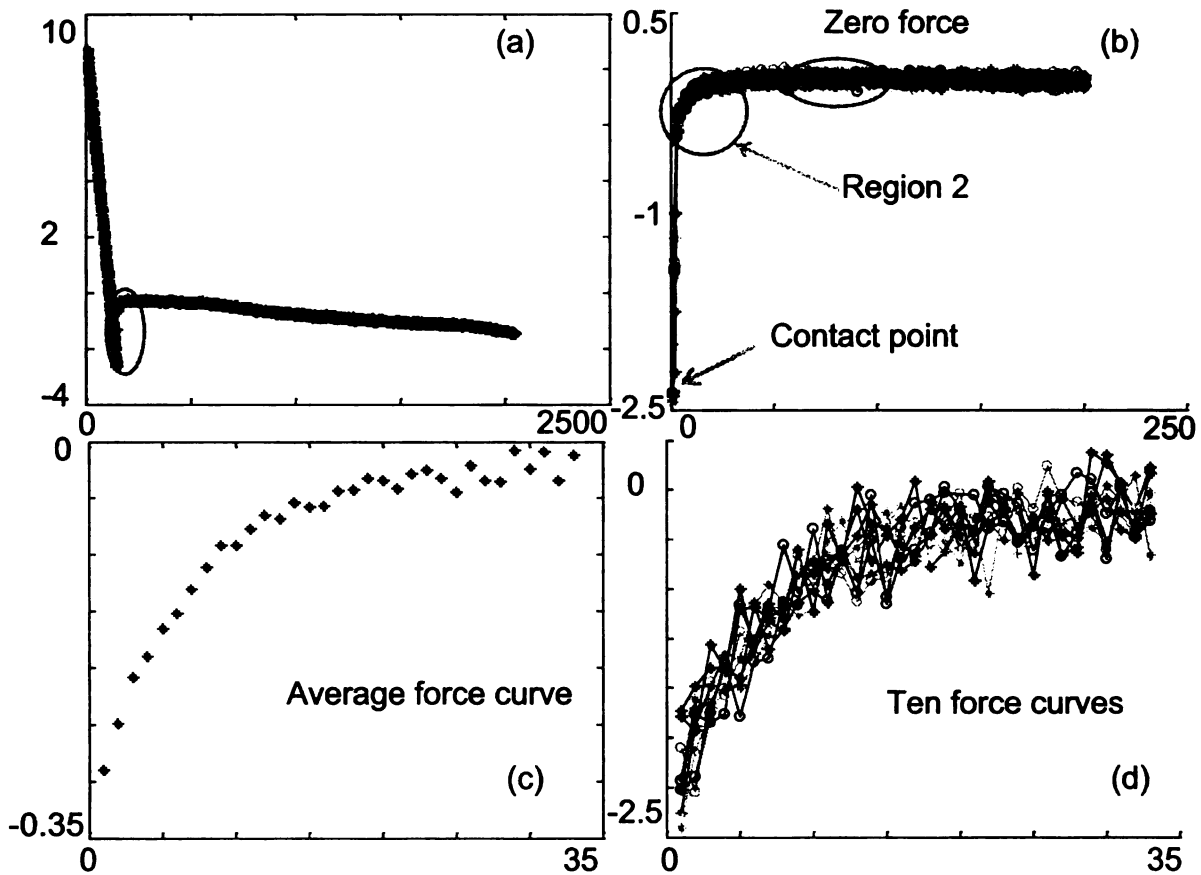


**Figure 5.8 Ten experimental force curves in same sample position.**

Ten force curves are averaged at each sample position and a total of 33 data points are obtained in region 2. Six data points are used to estimate the unknown parameters  $A$  and  $d_0$  in equation (5.28) as shown in Figure 5.9(b). The radius of the spherical cap,  $R$ , was set to 100nm and angle  $\alpha$ , to  $35^\circ$ . The RMS values estimated are Hamaker constant  $A = 0.01867\text{nNm}$  and position of the contact point  $d_0 = 37.56\text{nm}$ . For model validation, these parameter values are used in equation (5.28) to calculate the force at the remaining 28 points. The validation results are presented in Figure 5.9 (c).

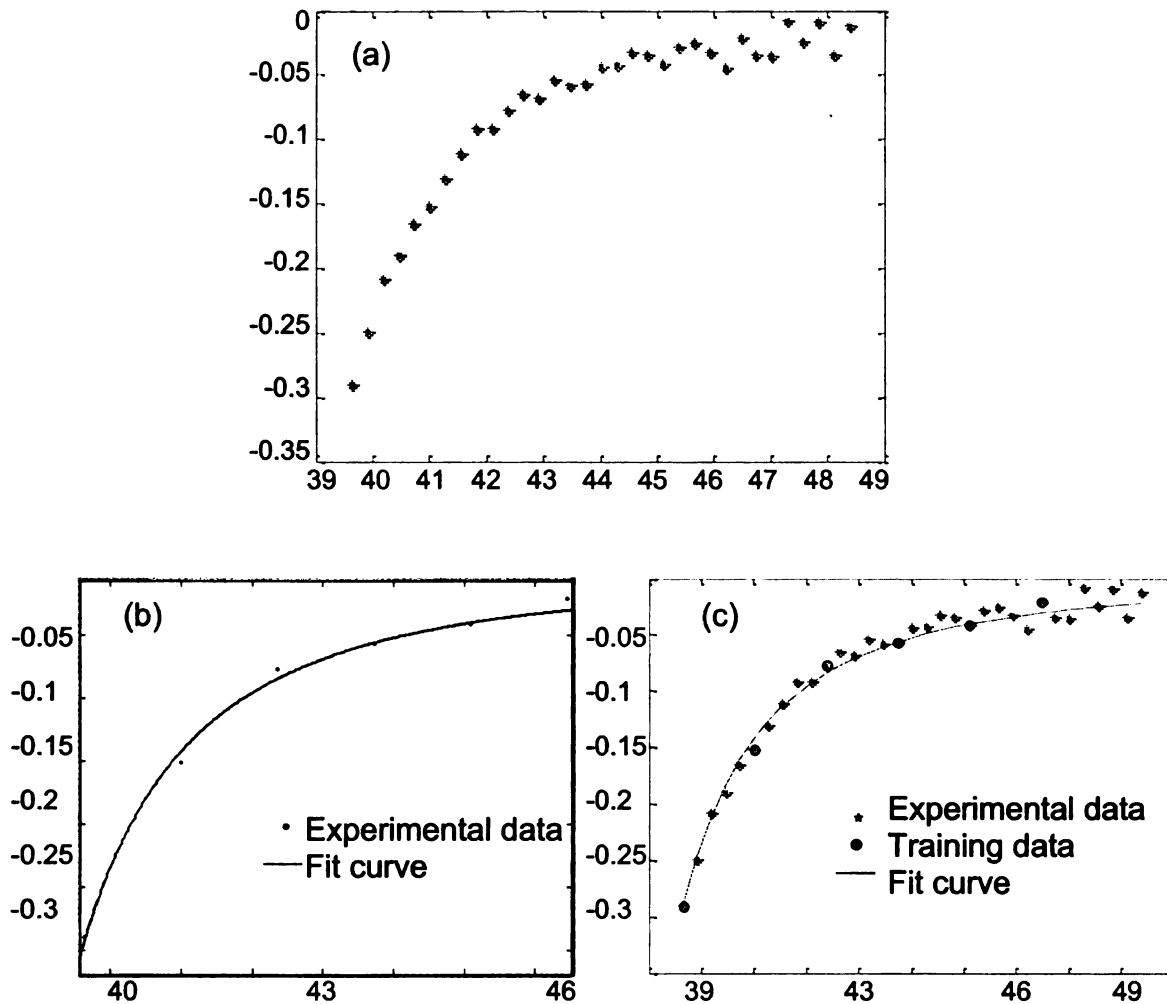


**Figure 5.9** A scheme showing the estimation of the unknown parameters and comparison of the theoretical force curve with the experimental data

The theoretical Van der Waals force is shown in red and the experimental data are shown as blue stars. The red stars are the data used for estimating the unknown parameters. From Figure 5.9(c) we can see the theoretical model predictions agree with the experimental data very well which validates the Van der Waals model in equation (5.28).

### 5.3 Numerical Result of Van der Waals (VDW) Force Model

The analytical model for Van der Waals force between a parametric tip and a flat sample has been calculated and validated using the experimental AFM data. The next step is to extend the VDW model for interactions between a parametric tip and a non-flat sample. In the case of a non-flat sample, the double surface integration is very difficult to evaluate analytically and numerical methods must be developed for generating a model of the Van der Waals force as outlined in Figure 5.10.

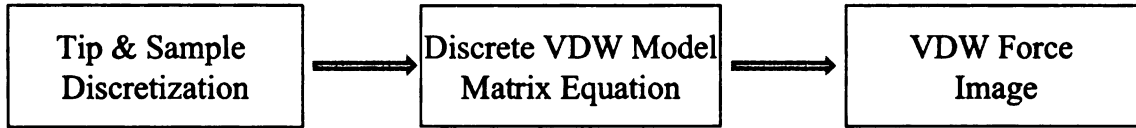


**Figure 5.10 Schema of Van der Waals force calculation**

As defined previously in section 5.2, let  $s_1$  represent the surface of sample, and  $s_2$  represent the tip surface. The parametric tip surface can be divided into two parts:  $s_{21}$  - surface of spherical cap and  $s_{22}$ - the surface of truncated cone. The integration in equation (5.12) can be expressed as the sum of two double surface integrations as:

$$F = \frac{A}{c\pi^2} \int_{s_2} \int_{s_1} (G \cdot \hat{\mathbf{n}}_1) \hat{\mathbf{n}}_2 ds_1 ds_2 = \frac{A}{c\pi^2} \left( \int_{s_{21}} \int_{s_1} (G \cdot \hat{\mathbf{n}}_1) \hat{\mathbf{n}}_{21} ds_1 ds_{21} + \int_{s_{22}} \int_{s_1} (G \cdot \hat{\mathbf{n}}_1) \hat{\mathbf{n}}_{22} ds_1 ds_{22} \right) \quad (5.30)$$

The surfaces of the tip and sample are first discretized into a finite number of small square elements. The double surface integration can then be calculated as double sum of the pairwise interaction forces between each element on sample surface  $s_1$  and tip surface  $s_2$  as shown below:

$$\begin{aligned}
F &= \frac{A}{c\pi^2} \sum_{s1} \sum_{s2} (G_{1,2} \cdot \widehat{\mathbf{n}}_1) \widehat{\mathbf{n}}_2 s_1 s_2 \\
&= \frac{A}{c\pi^2} \sum_{s1} \sum_{s21} (G_{1,21} \cdot \widehat{\mathbf{n}}_1) \widehat{\mathbf{n}}_{21} s_1 s_{21} + \frac{A}{c\pi^2} \sum_{s1} \sum_{s22} (G_{1,22} \cdot \widehat{\mathbf{n}}_1) \widehat{\mathbf{n}}_{22} s_1 s_{22}
\end{aligned} \tag{5.31}$$

### 5.3.1 Surface Discretization

The discretization of spherical cap and truncated cone surfaces are described below.

i). Spherical cap: Figure 5.12 shows a schematic of the spherical cap. The  $(x, y, z)$  coordinates of each point  $(x, y, z)$  on the spherical cap surface, is expressed as:

$$x = x_0 + R \cdot \sin(\omega_z) \cdot \cos(\omega_{xy}) \tag{5.32}$$

$$y = y_0 + R \cdot \sin(\omega_z) \cdot \sin(\omega_{xy}) \tag{5.33}$$

$$z = z_0 + R - R \cdot \cos(\omega_z) \tag{5.34}$$

where  $(x_0, y_0, z_0)$  is the tip apex coordinate,  $\omega_z$  varies from 0 to  $\alpha$  and  $\omega_{xy}$  varies from 0 to  $2\pi$ .

Consider four points,  $a_{11}$ ,  $a_{12}$ ,  $a_{21}$ ,  $a_{22}$  on the spherical cap surface as illustrated in Figure 5.12 (a). The coordinates of these four points are expressed as below.

$a_{11}$ :

$$\begin{cases}
x_{a11} = x_0 + R \cdot \sin(\omega_{za11}) \cdot \cos(\omega_{xya11}) \\
y_{a11} = y_0 + R \cdot \sin(\omega_{za11}) \cdot \sin(\omega_{xya11}) \\
z_{a11} = z_0 + R - R \cdot \cos(\omega_{za11})
\end{cases} \tag{5.35}$$

$a_{12}$ :

$$\begin{cases}
x_{a12} = x_0 + R \cdot \sin(\omega_{za12}) \cdot \cos(\omega_{xya12}) \\
y_{a12} = y_0 + R \cdot \sin(\omega_{za12}) \cdot \sin(\omega_{xya12}) \\
z_{a12} = z_0 + R - R \cdot \cos(\omega_{za12})
\end{cases} \tag{5.36}$$

a21:

$$\begin{cases} x_{a21} = x_0 + R \cdot \sin(\omega_{za21}) \cdot \cos(\omega_{xya21}) \\ y_{a21} = y_0 + R \cdot \sin(\omega_{za21}) \cdot \sin(\omega_{xya21}) \\ z_{a21} = z_0 + R - R \cdot \cos(\omega_{za21}) \end{cases} \quad (5.37)$$

a22:

$$\begin{cases} x_{a22} = x_0 + R \cdot \sin(\omega_{za22}) \cdot \cos(\omega_{xya22}) \\ y_{a22} = y_0 + R \cdot \sin(\omega_{za22}) \cdot \sin(\omega_{xya22}) \\ z_{a22} = z_0 + R - R \cdot \cos(\omega_{za22}) \end{cases} \quad (5.38)$$

where  $\omega_{za11} = \omega_{za12}$ ,  $\omega_{za21} = \omega_{za22}$ ,  $\omega_{xya11} = \omega_{xya21}$  and  $\omega_{xya12} = \omega_{xya22}$ . Figure 5.11

shows the tessellation of the spherical cap.

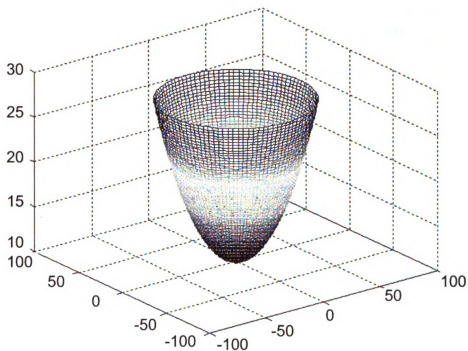
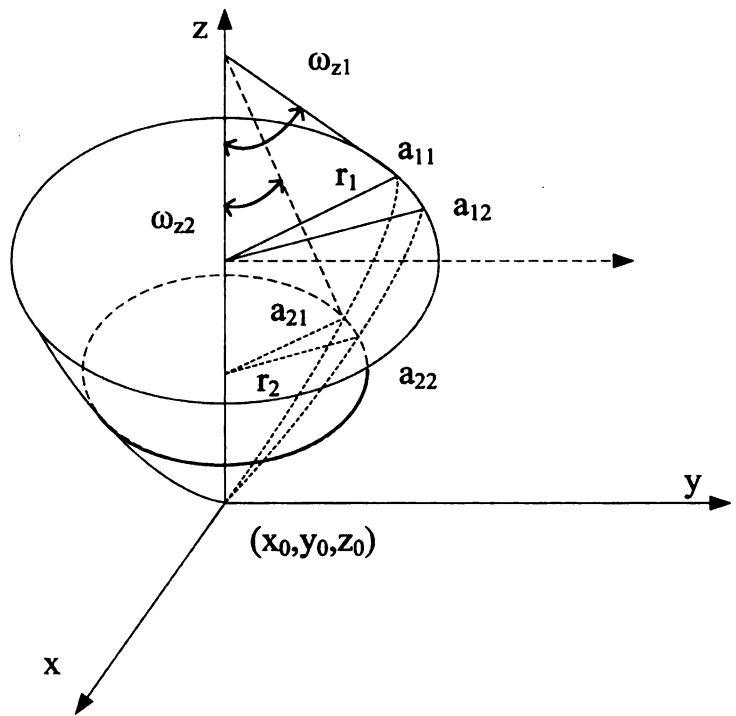
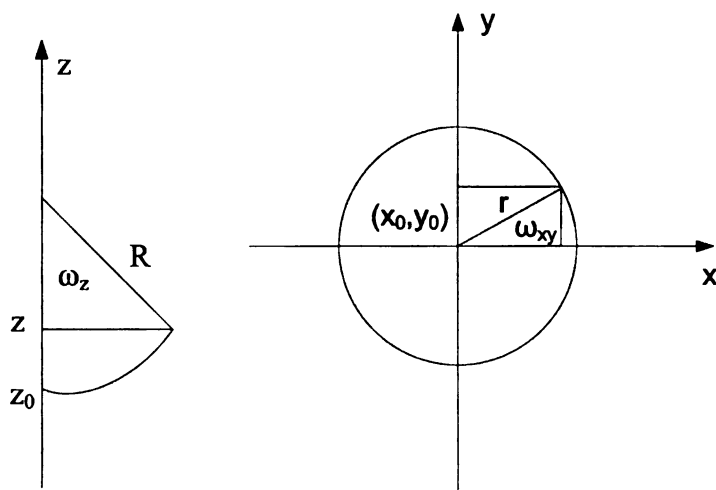


Figure 5.11 Discretization of spherical cap.



(a)



(b)

(c)

**Figure 5.12 (a) Schematic of elements in spherical cap (b) Cross section of spherical cap in  $x$ - $z$  plane (c) Cross section of spherical cap in  $x$ - $y$  plane.**

ii). Truncated Cone:

A schematic of the truncated cone is shown in Figure 5.14. As illustrated in Figure 5.14

(b) and (c), the  $(x, y, z)$  coordinate of each point on the truncated cone surface is expressed as:

$$x = x_0 + r \cdot \cos(\omega_{xy}) \quad (5.39)$$

$$y = y_0 + r \cdot \sin(\omega_{xy}) \quad (5.40)$$

$$z = z_0 + R(1 - \cos \alpha) + \tan \alpha(r - R \sin \alpha) \quad (5.41)$$

where  $(x_0, y_0, z_0)$  is the tip apex coordinate,  $r$  is the cone radius and  $\omega_{xy}$  varies from 0 to

$2\pi$ . Consider four points (a11, a12, a21, a22) on the truncated cone surface. From Figure

5.14 (a), the coordinates of these four points are defined as:

a11:

$$\begin{cases} x_{a11} = x_0 + r_{a11} \cdot \cos(\omega_{xya11}) \\ y_{a11} = y_0 + r_{a11} \cdot \sin(\omega_{xya11}) \\ z_{a11} = z_0 + R(1 - \cos \alpha) + \tan \alpha(r_{a11} - R \sin \alpha) \end{cases} \quad (5.42)$$

a12:

$$\begin{cases} x_{a12} = x_0 + r_{a12} \cdot \cos(\omega_{xya12}) \\ y_{a12} = y_0 + r_{a12} \cdot \sin(\omega_{xya12}) \\ z_{a12} = z_0 + R(1 - \cos \alpha) + \tan \alpha(r_{a12} - R \sin \alpha) \end{cases} \quad (5.43)$$

a21:

$$\begin{cases} x_{a21} = x_0 + r_{a21} \cdot \cos(\omega_{xya21}) \\ y_{a21} = y_0 + r_{a21} \cdot \sin(\omega_{xya21}) \\ z_{a21} = z_0 + R(1 - \cos \alpha) + \tan \alpha(r_{a21} - R \sin \alpha) \end{cases} \quad (5.44)$$

a22:

$$\begin{cases} x_{a22} = x_0 + r_{a22} \cdot \cos(\omega_{xya22}) \\ y_{a22} = y_0 + r_{a22} \cdot \sin(\omega_{xya22}) \\ z_{a22} = z_0 + R(1 - \cos \alpha) + \tan \alpha (r_{a22} - R \sin \alpha) \end{cases} \quad (5.45)$$

where  $r_{a11} = r_{a12}$ ,  $r_{a21} = r_{a22}$ ,  $\omega_{xya11} = \omega_{xya21}$  and  $\omega_{xya12} = \omega_{xya22}$ . Figure 5.13 shows a mesh of the truncated cone.

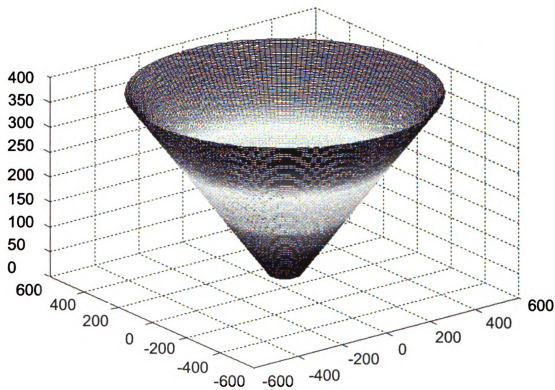


Figure 5.13 Mesh in truncated cone



### 5.3.2 Numerical Model Validation

In order to establish the validity of the model we first compare the numerical model simulation result with the analytical result, obtained for a flat sample same as in section 5.2.

Ideally, the double sum in the VDW model equation (5.31) should be calculated numerically on the entire surface of sample and tip to obtain the most accurate result. However, since the force between tip and sample decreases as distance increasing, regions of the sample and tip that are very far from each other can be neglected. We define the area where the force between tip and sample cannot be ignored as valid integration areas of both tip and sample. Hence in order to save computation time without affecting accuracy of the calculated force, equation (5.31) needs to be calculated only within the valid integration area.

In order to find the optimal size of valid integration area on the sample and tip surfaces, the double sum VDW models equation (5.31) is evaluated with gradually increasing areas of integration. Figure 5.15 shows the mesh of the integration tip and a square area on the sample surface. Figure 5.16 (a) shows a plot of Van der Waals force calculated with different size of integration area on sample surface for a fixed tip surface. The x-axis represents side of the square integration area on sample surface. The plot in Figure 5.16 (b) shows that the force increases with the integration area and saturates at a square of size 1500nm. Further increase in the area of integration does not change the force value significantly. In this thesis, we set the width of the valid integration area on sample surface to be 1500nm.

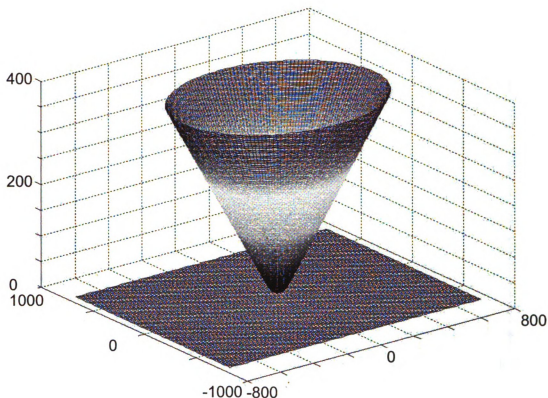


**Figure 5.15. Mesh of the tip and sample**

Similarly, the optimal integration area on tip surfaces estimated. Starting with initial area that includes the whole spherical cap, the maximum radius of the truncated cone represents the size of the integration area of tip surface. Figure 5.17 (a) shows Van der Waals force calculated with gradually increasing integration areas of tip surface. The x-axis represents the radius at the truncated end of cone,  $r_{con\_end}$ . Figure 5.17 (b) shows that the force increases with increasing  $r_{con\_end}$ . When the maximum radius cone is larger than 900nm, the force increase is negligible. In this research, we choose the  $r_{con\_end}$  as 900nm.

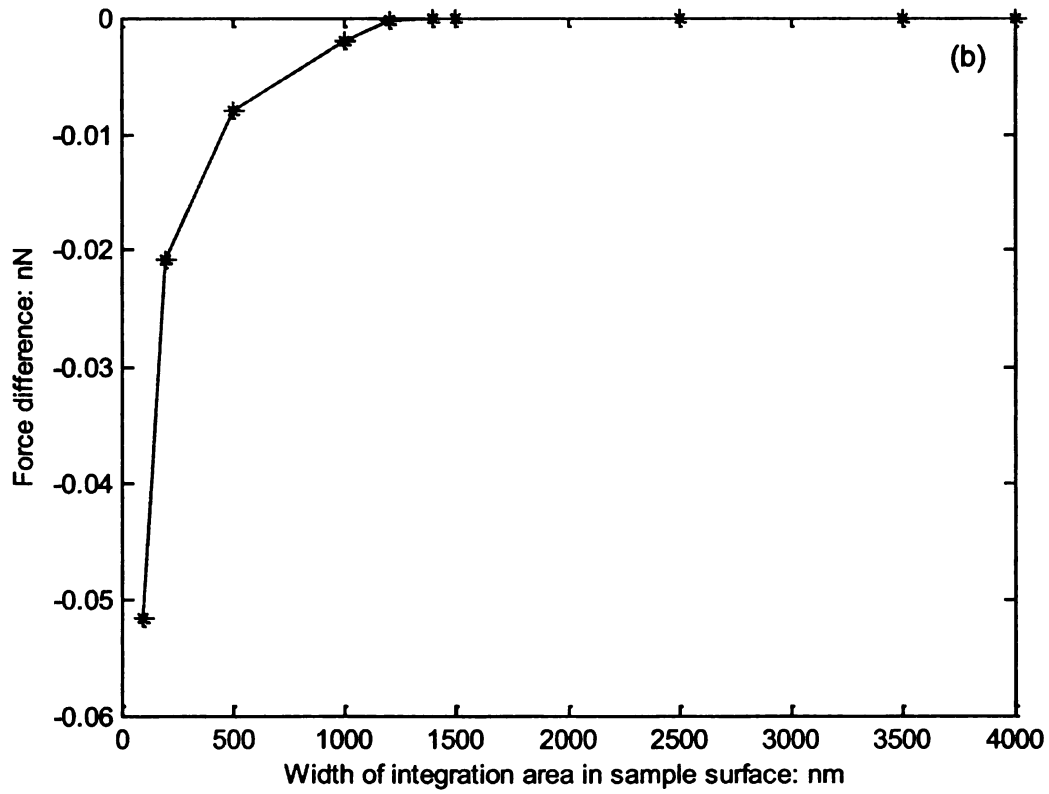
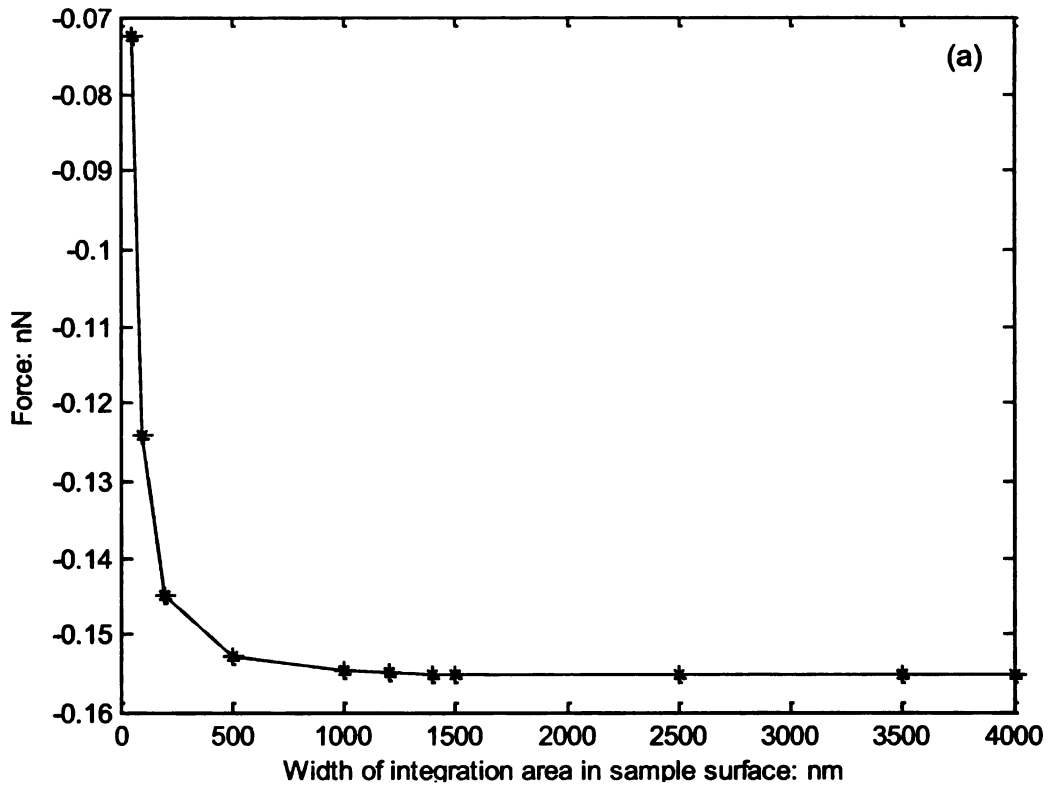


**Figure 5.16 Force vs. Size of integration area in sample surface**

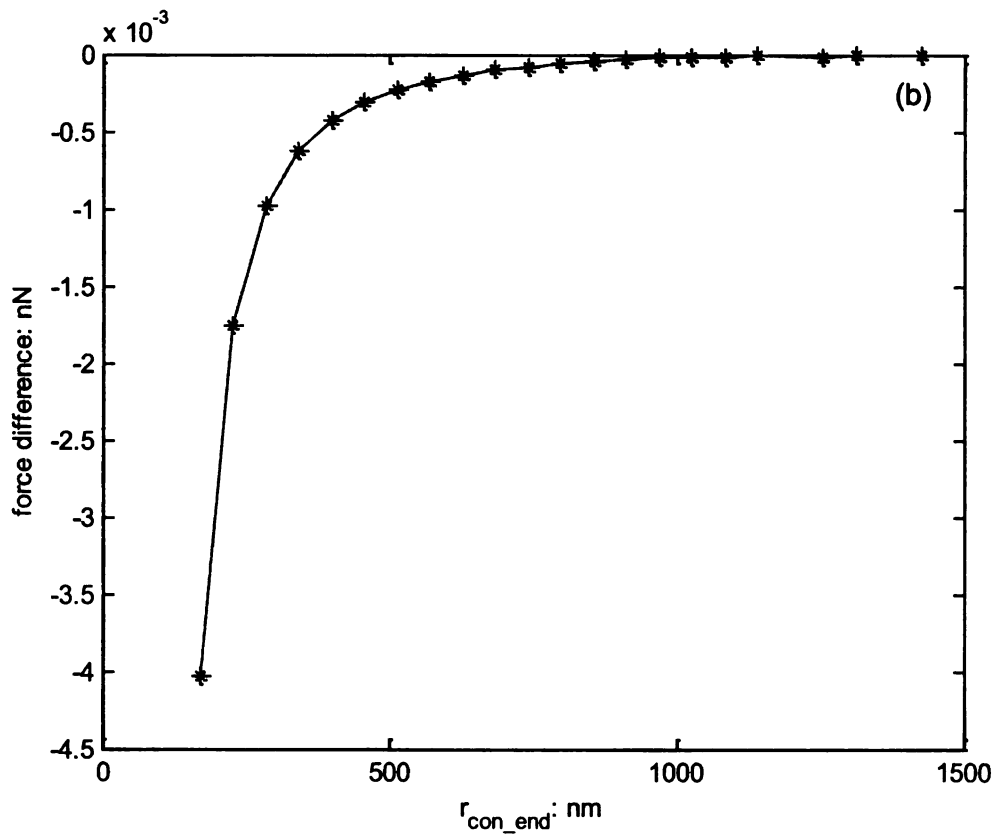
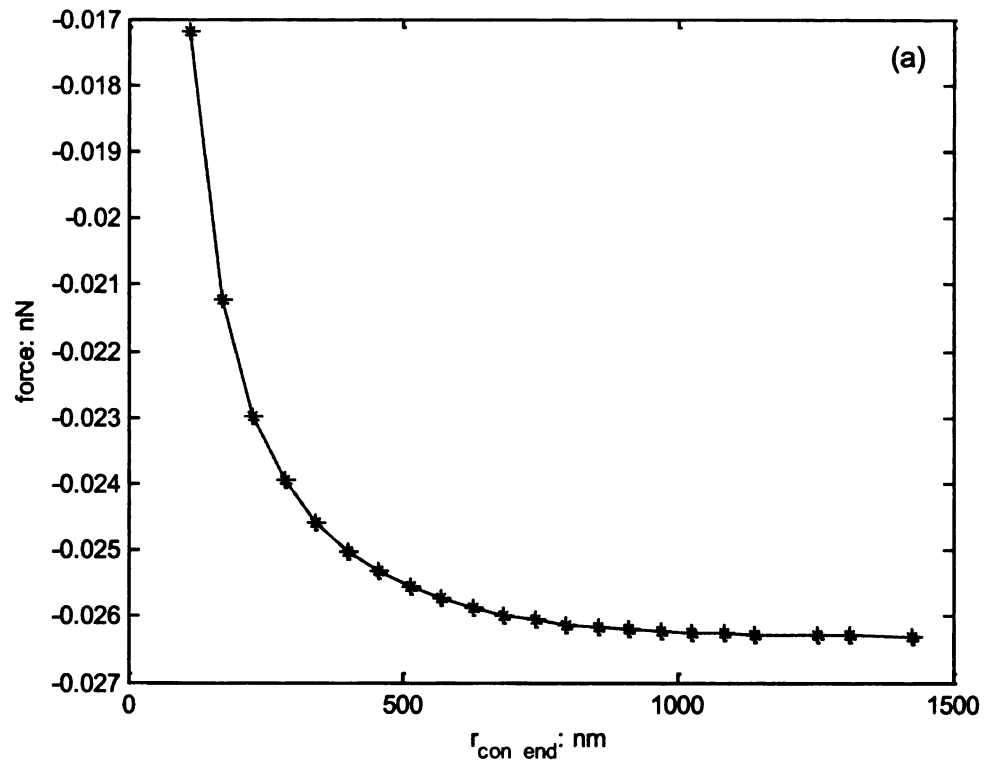
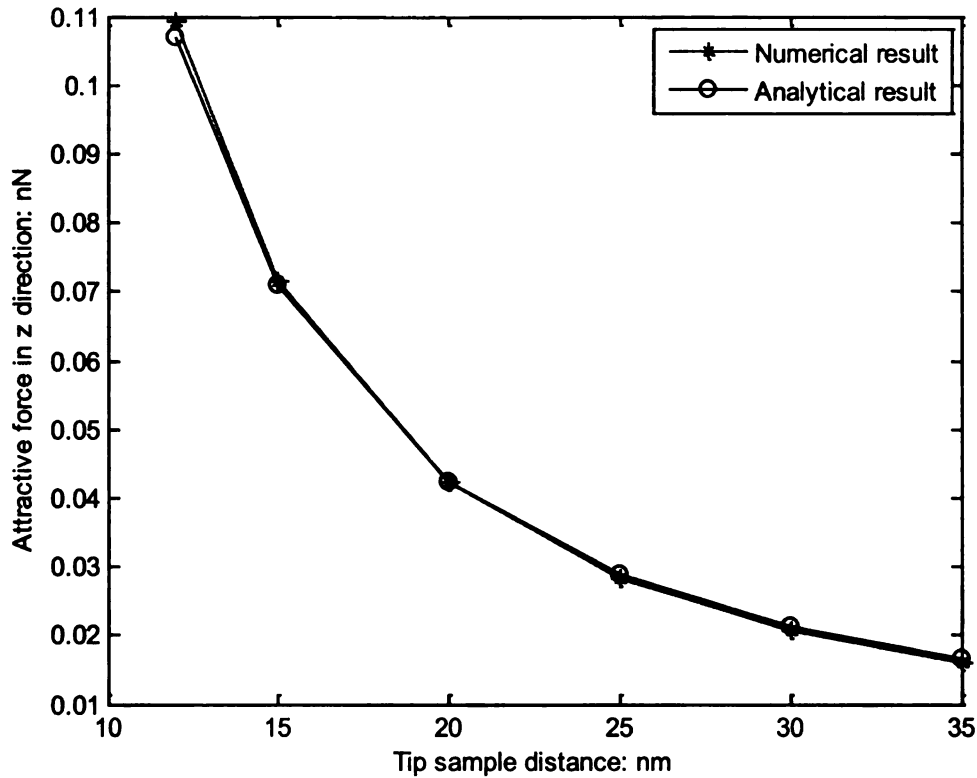


Figure 5.17 Force vs. Size of integration area in tip surface



**Figure 5.18 Force vs. tip-sample distance**

The numerical model is validated by comparing the simulation results of the same geometry using the numerical double sum VDW model equation (5.31) and analytical VDW model equation (5.28). Figure 5.18 shows the result of validation. The x-axis is the distance between the tip apex and sample and the y-axis is the corresponding force in z direction.

## 5.4 Model Based Deconvolution of AFM Image

Once the Van der Waals model is validated, the model can be used for a physics based deconvolution of the AFM image data. Figure 5.19 shows a schematic of the AFM image deconvolution procedure using the Van der Waals force model.

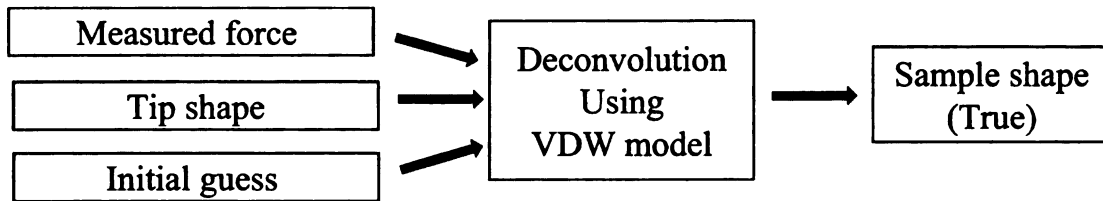


**Figure 5.19 Schematic of AFM image deconvolution using force model**

First the tip is positioned at a distance from sample surface so that the force detected will fall in region 2 dominated by the attractive part of Van der Waal force (Figure 5.2). Then the contact mode AFM is used to scan the sample to acquire the force measurements that yield sample topography with artifacts. With the Van der Waals force model and tip model, AFM image deconvolution can be formulated as an inverse problem which can be solved using the forward Van der Waals force model in an iterative framework as shown in Figure 5.20.

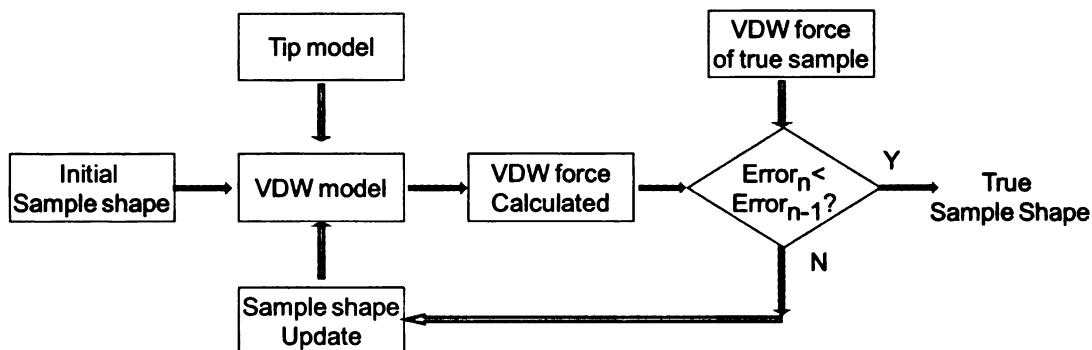


**Figure 5.20 Procedure of AFM image deconvolution using force model.**

1. The measured image data is used to derive the initial guess of the true sample shape  $s^{(0)}$ .

*Iteration n*

2. With the sample shape  $s^{(n)}$  and tip model, we calculate the VDW force using the validated forward model.

A  
P  
d  
be  
di

3. The error between the model calculated force and the measured force of the true sample is determined. If the error is within a prescribed threshold – STOP and  $s^{(n)}$  is the true shape of the sample.

4. Otherwise, the sample shape is updated to  $s^{(n+1)}$  so the error in step 3 is minimized. Since we know *a priori* that the measured image is dilation of the true shape by tip shape, the updating procedure simply involves sharpening the edge. Go to step 2.

## 5.5 Implementation Results

The above procedure for deconvolution is applied to a sample with an edge and corresponding AFM data generated using morphological dilation to introduce the artifacts. To simplify the overall procedure the error between model prediction and measurement is computed using the values at one position of the tip. Figure 5.21 shows a schematic of the tip and true sample topography for calculating the VDW force using the forward model. We use the parametric tip model as discussed before. The tip is placed above the sample at the distance of 10nm. Figure 5.22 shows the mesh of the sample surface.

The initial guess for the true sample shape was generated using the simulated AFM data and is shown in Figure 5.23. The edge was parameterized using a single parameter, namely the slope of the edge. Figure 5.24 shows the results of the image deconvolution using iterative deconvolution procedure. Figure 5.24 (a) shows the error between model and measured force values at single position in each iteration with different updated sample shapes. The successive updated sample edge shape in each

iteration and the final converged deconvolved sample edge shape are shown in Figure 5.24 (b) and compared with deconvolution result obtained using mathematic morphology described in Chapter 4.

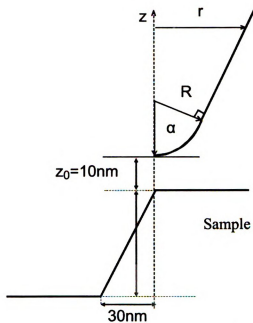


Figure 5.21 Schematic of the tip and sample surface

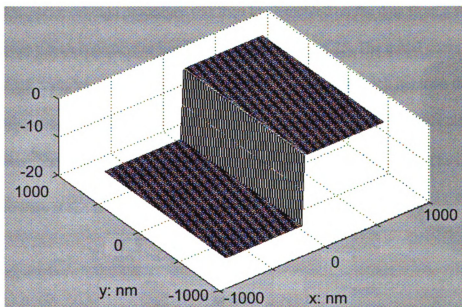


Figure 5.22 Mesh of the sample surface

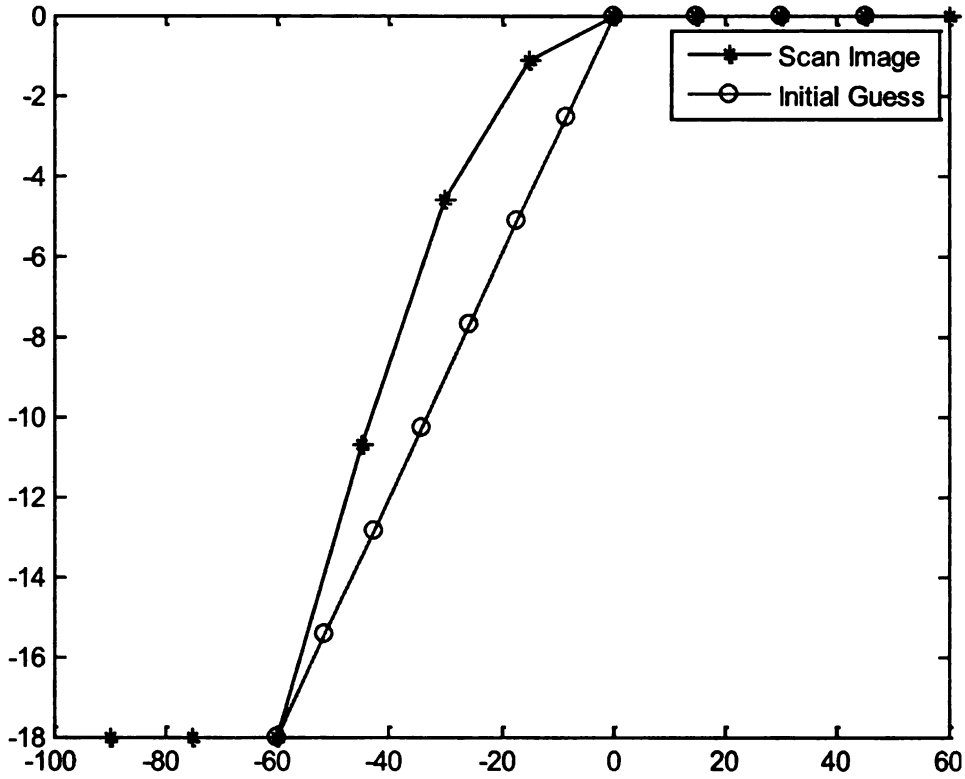


Figure 5.23 Line scan of the scan image and initial guess image

The deconvolution procedure was then implemented on the data from a second sample edge which is piecewise linear as shown in Figure 5.25. The initial guess is derived from samples of the (measured) simulated AFM data. In each iteration the error is calculated using the model prediction and measured force values at a single position of the tip. In  $n^{th}$  iteration, the sample shape is defined as  $s^n = (z_0^n, z_1^n, \dots, z_m^n)$ . The updating of sample edge shape is carried out as below:

$$z_m^n = \begin{cases} z_m^{n-1} - \frac{R - \sqrt{R^2 - (x_m^{n-1})^2}}{3} & m > n \\ 0 & m < n \end{cases} \quad (5.46)$$

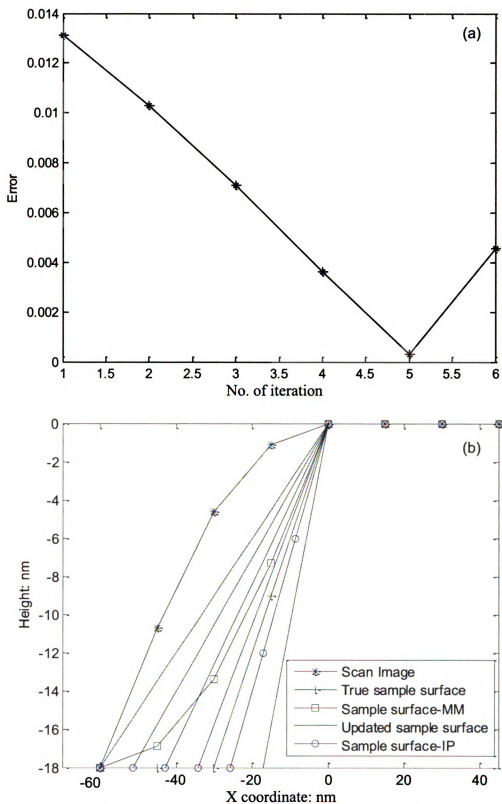
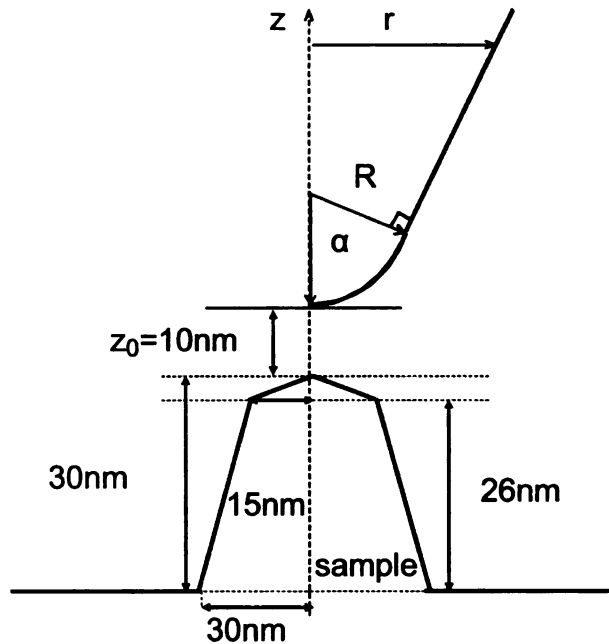


Figure 5.24 Result of the image deconvolution using VDW force model



**Figure 5.25 Schematic of the tip and sample**

Figure 5.26 shows the results of the image deconvolution using iterative deconvolution procedure. The error between model predicted and measured force values at single position in each iteration with different updated sample shapes are shown in Figure 5.26 (a). Figure 5.26 (b) shown the updated sample edge shape in each iteration, the final converged deconvolved sample edge shape and compared with deconvolution result obtained using mathematic morphology described in Chapter 4.

The force-model based deconvolution algorithm has been developed and initial results show the feasibility of the method for determining true topographic shapes of the sample. However currently, the algorithm is applied to minimizing the error between model and measurement data at one position of the tip. The results will be much more accurate if the error is computed using VDW force calculations and measurements on a larger scan area centered at each point.

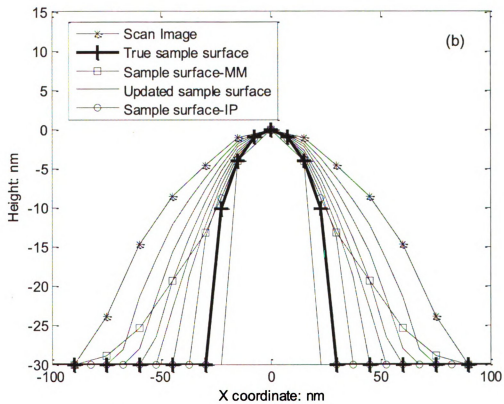
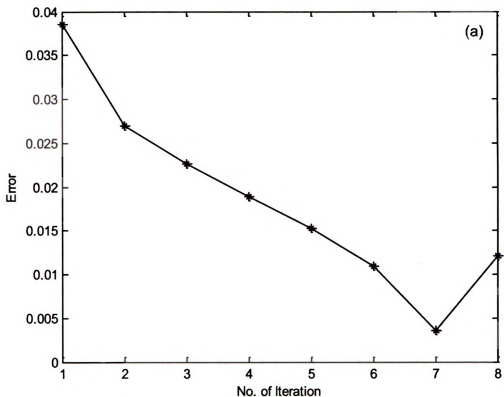


Figure 5.26 Result of the image deconvolution using VDW force model

# **Chapter 6 Application of SPRM to Tissue Engineering**

## **6.1 Introduction**

From its inception, SPRM was developed within an application framework for two reasons. One was to challenge the instrument development with real versus ideal problems. As will be discussed in detail in this chapter, the evaluation of the properties of tissue scaffolds used for regenerative medicine provided a challenging example which contributed greatly to the development of SPRM. The second reason was to introduce the large potential users community to the newly available SPRM capability. This is best accomplished by demonstrating the power of the technique to investigate significant research problems in new and better ways.

Tissue scaffold engineering is an active and successful research field [97-99] in biological studies. Tissue engineering is the use of a combination of cells, engineering materials, and suitable biochemical factors to improve or replace biological functions [100]. The field of tissue engineering merges the expertise of life sciences, physical sciences, and engineering to develop functional tissues that can maintain, restore, or improve damaged organs [101]. Biomaterials have played a crucial role in the development of tissue engineered organs. Cells are 'seeded' into an artificial structure capable of supporting three-dimensional tissue formation. These artificial structures, usually referred to as scaffolds, allow the cell attachment and migration. The scaffolds deliver entrained growth and can even exert certain mechanical and biological influences to modify the behavior of the cell phase. The success of tissue engineering has helped in

clinical implant work within complex tissues such as bladders [97] and cartilage [98]. However, despite such successes much fundamental understanding is still needed to design scaffolds with the most appropriate mechanical, topographical and chemical properties for particular cells or cell classes.

Actin-based cells can actively probe their environment through lamellipodia and filopodia extension. The leading edge of such extensions corresponds to tens of nanometers sensing area at the cell's extremities. The environmental triggers that cause extension/retraction/re-direction through actin polymerization/depolymerization should therefore be assessed on a comparable scale. With nanometer-scale resolution, atomic force microscopy is suitable to be used to investigate minimally conductive biological surfaces [51].

Recently two important mechanical properties, surface roughness and elasticity, are found to be important for cell growth. Deligianni et al have published the effect of surface roughness of hydroxyapatite on human bone marrow cell grow [102]. Their experiment discovered that surface roughness affected cellular response, cell adhesion and proliferation. Engler A.J. et al investigated the correlations between substrate stiffness and cell adhesion [103]. Their experimental result shows that the adhesive spreading of cells correlates broadly with the effective stiffness of substrate tissues and stiffer materials tend to promote spreading of smooth muscle cells. These two mechanical properties are investigated using SPRM in this work.

## 6.2 Materials and Methods

### (A) Tissue Scaffold Samples

Tissue scaffolds fabricated from electrospun [104, 105] carbon nanofibers was obtained from the Donaldson Company. The nanofibers were electrospun using an adapted electrospinning probe procedure described in Reference [106]. No further information about the tissue scaffolds samples was provided.

### (B) Nanoscope IIIa Special SPRM Modification

The scanning probe microscopy (SPM) experiments were performed using a Veeco Instruments Nanoscope IIIa operated in atomic force microscopy contact mode in ambient air [4, 6, 41, 51]. The system has a special modification developed by our research group in partnership with Veeco Instruments. SPRM system is used to scan the sample. The SPM system itself is given the ability to auto-focus on regions of interest through incorporation of recognition-based tip control, described as Scanning Probe Recognition Microscopy (SPRM). The recognition capability of SPRM is realized using algorithms and techniques in computer vision, pattern recognition and signal processing fields. Adaptive learning and prediction are also implemented to make detection and recognition procedure quicker and more reliable. The integration of recognition makes the SPRM system more powerful and flexible in investigating specific properties of samples.

### 6.3 Surface Roughness

The surface roughness of the substrate has been shown to influence cell attachment. It is therefore important to obtain this information accurately and conveniently along tissue scaffold nanofibers. In the majority of studies, the surface roughness is the Root Mean Square (RMS) of height values in a region of interest as defined in equation (6.1).

$$RMS = \sqrt{\frac{\sum_{i=1}^N (Z_i - Z_{ave})^2}{N}} \quad (6.1)$$

For AFM-based measurements,  $N$  is the number of total pixilated data points in this region;  $Z_i$  is the height value at each pixel and  $Z_{ave} = \frac{1}{N} \sum_{i=1}^N Z_i$  is the average value of all height values.

In conventional atomic force microscopy, the surface roughness information is acquired through manual application of a rectangular region of interest box [107]. The surface roughness within the box is then calculated using equation (6.1). There are several problems with the conventional approach to surface roughness investigation when the sample is a tissue scaffold nanofiber.

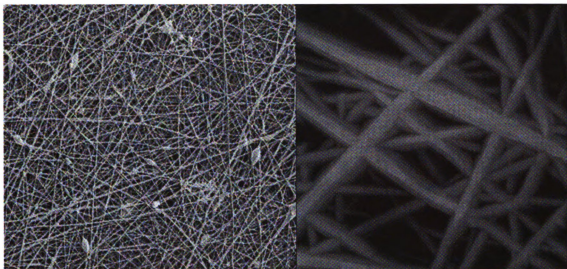
(1) The shape of the region of interest (ROI) may not be rectangular, necessitating the application of several small ROI boxes which follow the curvature of the nanofiber.

(2) Only a single value is provided for each time of operation. Therefore, in order to get surface roughness along a nanofiber, this operation would need to be repeated for many times.

(3) Height data,  $Z$ , is used to calculate the surface roughness. This is acceptable for samples whose surfaces are relatively flat because then the variation in height data will reflect the variation in their surface roughness. This assumption is no longer appropriate for tissue scaffolds because the nanofibers have a cylinder shape. Therefore, the variation of height data,  $Z$ , includes not only its surface roughness variation, but also the variation caused by the shape.

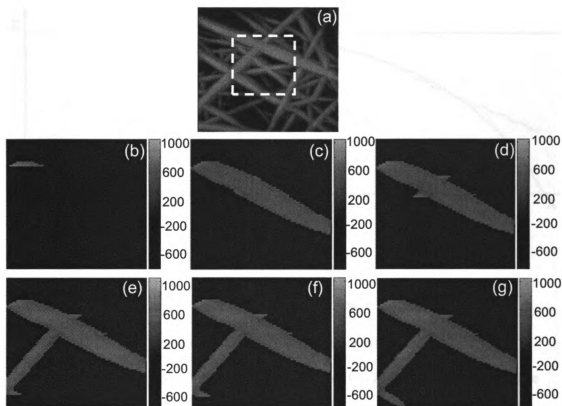
In the SPRM system, a recognition-based scan plan can be generated to auto-focus tip motion along an individual nanofiber [69, 108]. Adaptive scanning enables SPRM to follow along an individual nanofiber even when it crosses another as shown in Figure 3.13. Therefore, the whole nanofiber, or whole nanofiber mesh becomes the region of interest.

Figure 6.1 (a) shows the Atomic force microscope (AFM) images of tissue scaffold sample. Figure 6.1 (b) shows the scanning electron microscope (SEM) images to ensure that the AFM results were representative over larger scaffold areas. SPRM were then used to scan the same sample to provide more reliable and accurate surface roughness detail.



**Figure 6.1** (a) AFM image of electrospun carbon nanofiber tissue scaffold. The scan area is 5 square microns and the z-height projection is 1500 nanometers. (b) SEM image of electrospun carbon nanofiber tissue scaffold. The scan area is 20 square microns, images by Q. Chen and Y. Fan [70].

In the SPRM system, a recognition-based scan plan can be generated to auto-focus tip motion along an individual nanofiber as discussed in chapter 3. Figure 6.2 shows the conventional AFM image of the nanofiber and the SPRM scan image of the nanofiber. The SPRM system starts with coarse scan and picks up the first nanofiber as shown in Figure 6.2 (b). During the fine scanning, adaptive scanning algorithm enables SPRM to follow along an individual nanofiber even when it crosses another nanofiber as shown in Figure 6.2 (d). Therefore, the whole nanofiber, or the whole nanofiber mesh becomes the region of interest. After finishing high resolution fine scan only on the first nanofiber, SPRM system returns to coarse scan to find another region of interest. This coarse-fine-coarse scan procedure will keep going on until SPRM system finish scanning the whole region.



**Figure 6.2** SPM scan image of the nanofiber. (a) Conventional AFM image of the nanofiber (b) Coarse Scan picks up the first nanofiber; (c) Finish high resolution fine scan only on the first nanofiber and return to coarse scan to find another region of interest; (d) Coarse Scan picks up the second nanofiber; (e) Finish the high resolution fine scan only on the second nanofiber and return to coarse scan to find another region of interest; (f) Coarse Scan picks up the third nanofiber; (g) Finish the high resolution fine scan only on the third nanofiber. Images by Y. Fan and Q. Chen [109].

In Scanning Probe Recognition Microscopy, distance data,  $D$ , instead of height data,  $Z$ , was used to get the real roughness of the sample surface. The Kåsa circle fit method [110] was implemented to get the center  $(x_{center}, z_{center})$  of the most fitted circle as shown in Figure 6.3. Then the distance  $D_i$  between each point on the surface and the fitted circle center was evaluated and used to calculate the surface roughness maps and histograms.

$$D_i = \sqrt{(Z_i - Z_{center})^2 + (X_i - X_{center})^2} \quad (6.2)$$

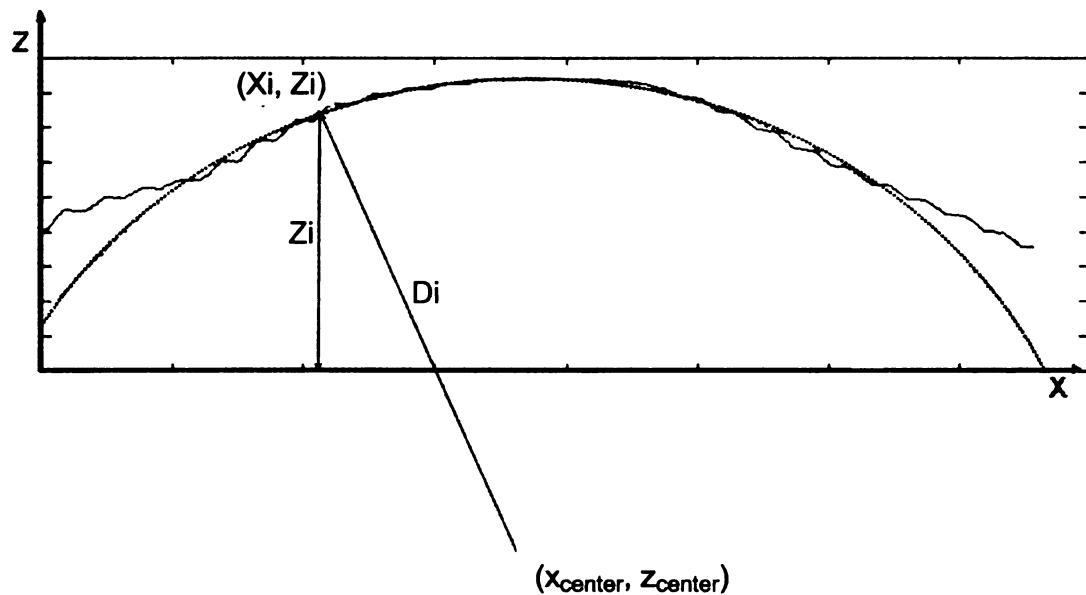


**Figure 6.3 Circle fit based on Kasa method [70]**

Only the center part of the height data was used to find the best fit circle. The boundary regions are unreliable due to tip-shape dilation effects. Dilation, or broadening of the image, is a result of the side of the tip coming into contact with the curved side of the nanofiber [72, 76]. When an SPRM scan is focused on an individual nanofiber, both the edge and center data is acquired. However, only the center part of the nanofiber provides reliable data because of the tip convolution effect [56, 73]. The ideal AFM would have an infinitely sharp tip to reach as much of the surface as possible and an infinitely sharp impulse response in its feedback system to instantly adjust the height of the tip as it is scanned over the surface. However in reality, the tip has a pyramidal or conical shape with some finite end radius so it is durable enough to withstand the surface interaction forces. The effects of the tip shape cannot be avoided and these result in characteristic tip-dilation artifacts, as shown in Figure 6.4 (a). The nanofiber properties evaluations are restricted to regions of reliable data through the use of an erosion

operation [111]. This is an important consideration when analyzing tissue scaffold nanofiber geometries using AFM-based methods (instead of planar substrates).

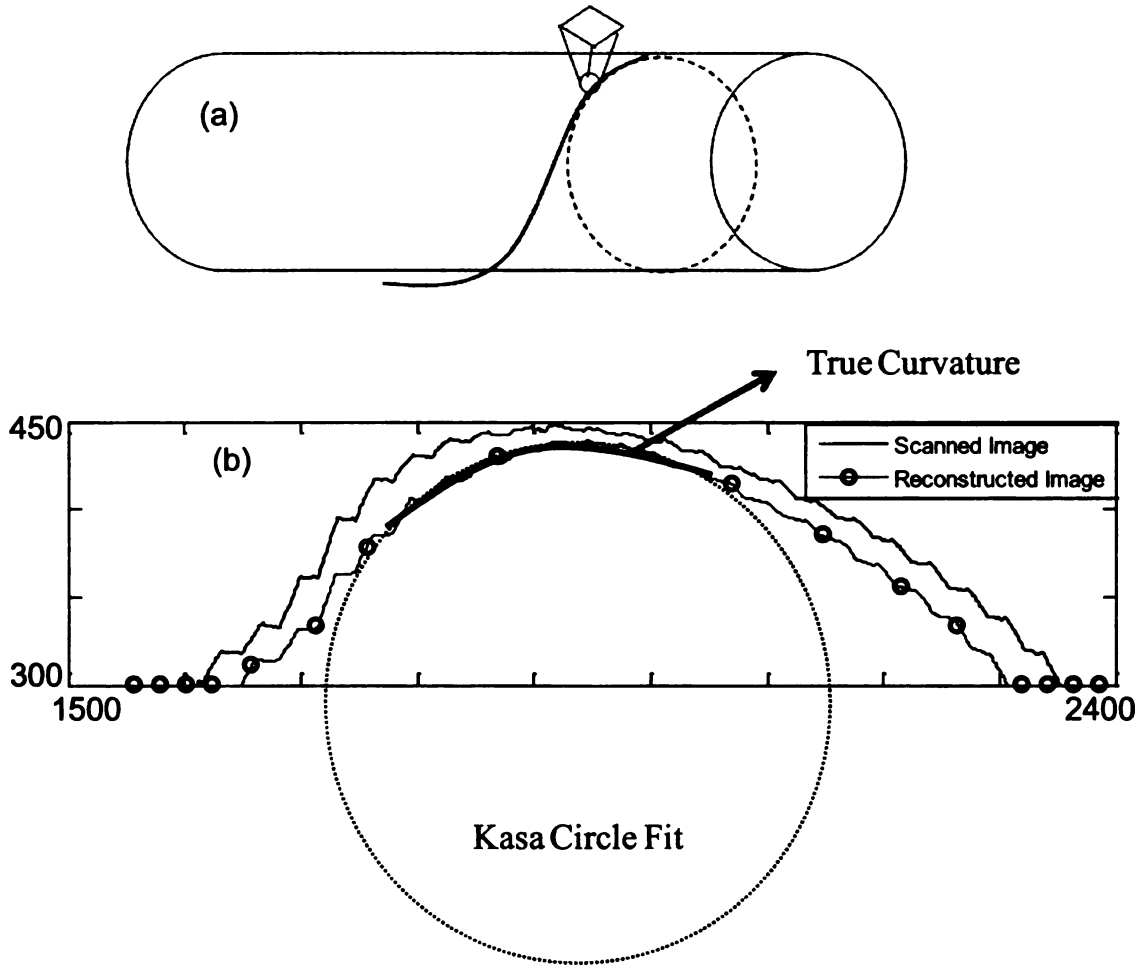


**Figure 6.4 (a) Characteristic tip-dilation artifacts (b) The cross section of a real AFM nano fiber image and the best fit circle [70]**

Using data obtained by SPRM along individual nanofibers, the surface roughness was calculated on each pixel based on a local neighborhood region using below equations:

$$Roughness = \sqrt{\frac{\sum_{i=1}^N (D_i - \bar{D})^2}{N}} \quad (6.3)$$

$$\text{and } \bar{D} = \frac{1}{N} \sum_{i=1}^N D_i \quad (6.4)$$

The shape and size of the local neighborhood region can be adjusted by the user, which makes the system adaptable to different sample shapes. In this research, a rectangular box around each pixel is chosen as the local neighborhood region, with a width of box size of 219.76 nm (close to the nanofiber diameter) [108]. Multiple sets of overlapping surface roughness information were generated, with the provision that any box that extended outside the nanofiber boundaries was automatically truncated. Total 564267 data points are used to calculate the surface roughness map. A surface roughness map along individual nanofiber was then generated as shown below.

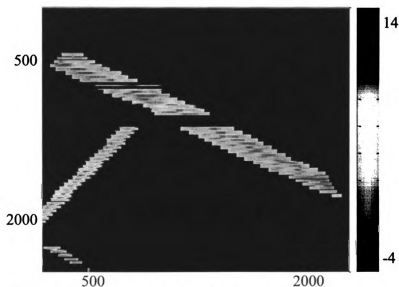


Figure 6.5 Surface roughness map along individual fiber [109]

The histogram of the surface roughness map is shown in Figure 6.6. From the histogram, we can get the mean value as 4.57nm, the mode value as 2.0nm, the variance value as  $7.15 \text{ nm}^2$ , and the range is 0.8nm~19.7nm. The histogram also shows the distribution of the surface roughness while an individually applied ROI box would be most likely to return the mode value. When comparing the surface roughness of different

samples, the mode value may not show the true difference. However, the variances and distributions will show the true difference between surface roughness of the samples [70, 108].

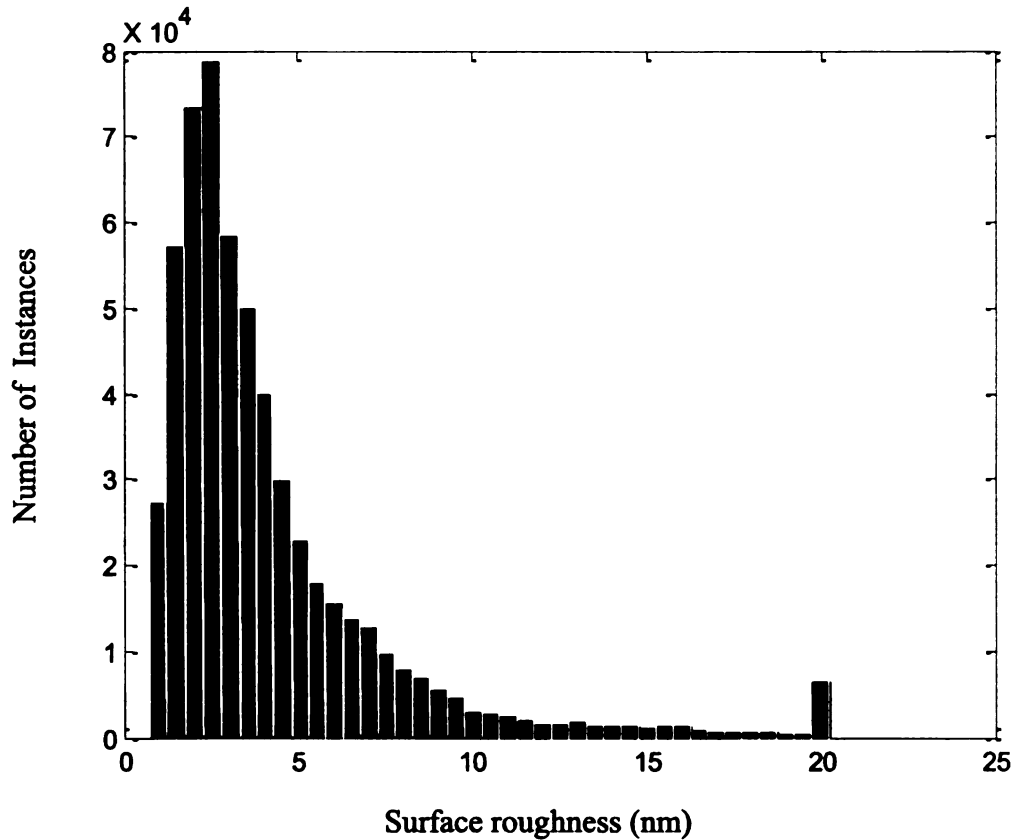
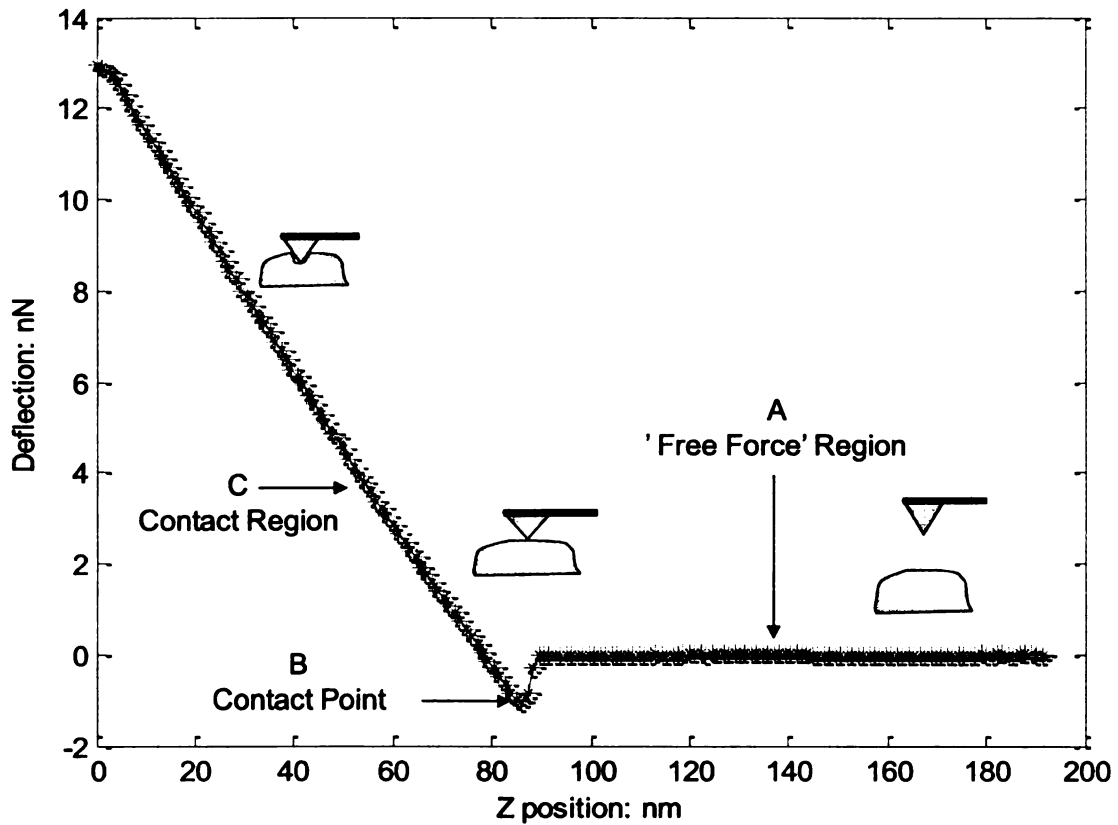


Figure 6.6 Histogram of surface roughness map [109]

## 6.4 Elasticity

Atomic force microscopy can be used to measure elastic properties by collecting force curves over points on the surface of the sample. AFM has been used to study the elasticity of cells [53, 112-116], bacteria [117], monkey eyes [27], gelatin films [118], human platelet [119] and tissue scaffold [70, 109, 120]. Analyzing the collected force curve with theoretical models can provide quantitative information on sample elasticity (i.e. Young's modulus, spring constant).

Force curve measurement consists in approaching and withdrawing an AFM tip from a surface and measuring the cantilever deflection that is induced by the interaction force between the tip and the sample surface. Figure 6.7 shows the approach force curve and corresponding tip sample position. In Figure 6.7, x axis is the tip position in z direction which is movement of electrical piezo in z direction. The y axis is the interaction force between the tip and sample. As introduced in chapter 1, the force is given by the measured cantilever deflection multiplied by the force constant of the cantilever. The approach curve starts with the tip far away from the surface. At these large distances the attractive long-range interaction between the tip and the sample is extremely small and there is no detectable deflection of the cantilever. This is the so-called 'force free' region shown as region 'A' in Figure 6.7. When the tip moves toward the sample in z direction, the tip will 'jump' to contact the sample due to the attractive Van der Waals force shown as contain point B in figure. When tip moves further toward the sample, the tip will indent into the ample surface shown as contact region 'C' in the Figure 6.7.



**Figure 6.7 Approach force curve and corresponding tip sample distance**

An array of force curves can be collected across the sample surface at regular intervals and this is known as force volume imaging. Figure 6.8 shows a traditional force volume imaging.

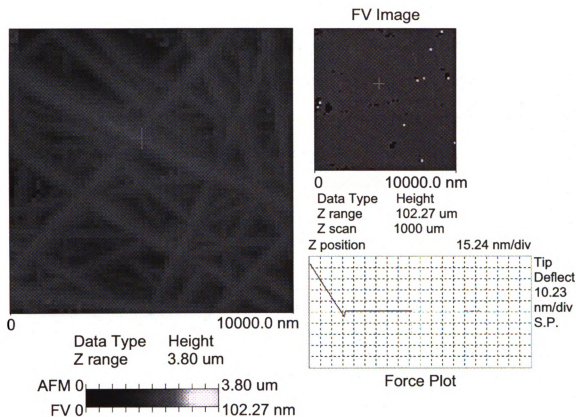


Figure 6.8 Traditional AFM force volume image

There are several serious problems when using the conventional force volume imaging in the nanofiber sample to collect the force curve for analyzing the elasticity property.

- (1) In conventional atomic force microscopy, the force volume imaging scans the entire scan area irrespective of the shape of the region of interest. This mode is slow and wasteful.
- (2) In conventional force volume imaging applied to tissue scaffolds, force curves acquired at regular intervals may not always be on a nanofiber. It will hit anywhere inside the scan region where may be not inside the region of interest which in tissue scaffold sample is the nanofiber.

- (3) The cross-section of the nanofiber is a circle shape. When the tip scans a point on the side of the nanofiber the sample surface normal is at an angle to the direction of the tip-sample interaction force.

In order to get a reliable measurement of the elasticity, the force curve must be collected at the top of the nanofiber where the force vector is exactly normal to the sample surface as shown in Figure 6.9.

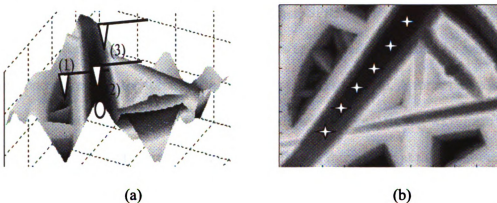


**Figure 6.9 (a) Tissue scaffold surface the tip contact point (b) 6 points were acquired along the individual nanofiber**

Force volume imaging using SPRM overcomes all of these difficulties. SPRM will provide capability to collect a wealth of surface roughness information extracted along many individual nanofibers using an automatic procedure that maintains uniformity of experimental conditions. SPRM will also provide the first capability to acquire force curves directly along an individual nanofiber so that the applied force is exactly normal to the curved nanofiber surface, therefore fulfilling conditions for appropriate use of the Hertz model elasticity analysis.

The SPRM system will first recognize the left and right edges of the nanofiber during the fine scanning and then detect the highest position in the section of nanofiber. Then tip is moved to that position. The tip position in z direction is recorded as the

sample surface height at that x-y location. After turning off the z-feedback loop, the tip is controlled to move in z direction to generate the force curve at this location. In the current experiment, the tip is first moved up from the normal tip sample contact point to a tip 'free-force' position where there is no strong interaction between the tip and sample. The system then sends a trig signal to inform the second PC to start collect the force and z position information. Tip is first brought down to the sample in z direction. After tip hits the sample surface and moves 5nm further, SPRM system will move the tip back to the 'free-force' position. When the tip moves toward and away from the sample, the second pc records the force in the tip and z position of the tip. A force curve is then generated at that x-y location. Figure 6.10 shows the signal timing waveform recorded by the second PC. Figure 6.11 shows the collected force curve at that location. The red one is the approach force curve which collected when the tip is brought down to the sample surface and the blue one is retract force curve which is collected when the tip is moving away from the sample. Using the same procedure, a set of force curves along the most reliable area in the nanofiber can thus be collected for calculating elasticity.

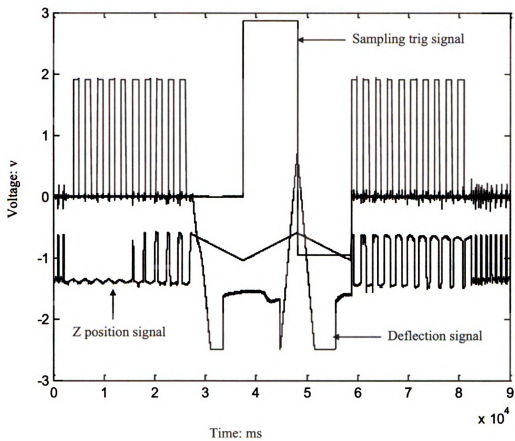


Figure 6.10 SPM force curve signal timing waveform

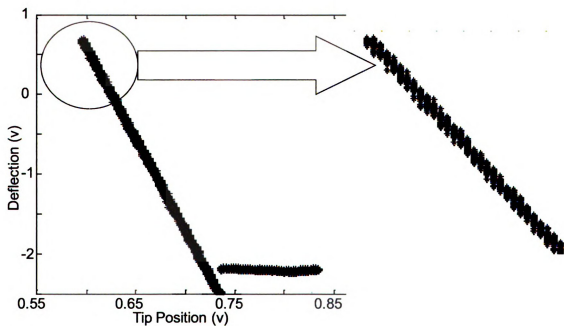


Figure 6.11 Force curve collected by the second PC

Figure 6.11 shows one recorded force curve collected in the reliable region. As we can see, in the same  $z$  position several deflection values are collected because of the limited resolution in the  $z$  position. The force curve is first passed the average filter which takes the average deflection value in each  $z$  position. The collected raw deflection value is the voltage output signal of the detection photodiode as introduced in chapter 1. By multiplying the sensitive constant, the voltage signal can be converted to the tip deflection in nm. Figure 6.12 shows the collected average force curve.

The force curves collected record the cantilever deflection versus the  $z$  position of the tip. Rather than using the tip  $z$  position, it is more useful to use the distance ( $D$ ) which is the relative separation between the tip and the sample surface, and this is known as a force-distance curve. A force-distance curve (FD) is defined as the cantilever deflection force versus the absolute distance ( $D$ ) between the tip and sample surface.

Figure 6.13 shows force-distance curve collected in the reliable region.

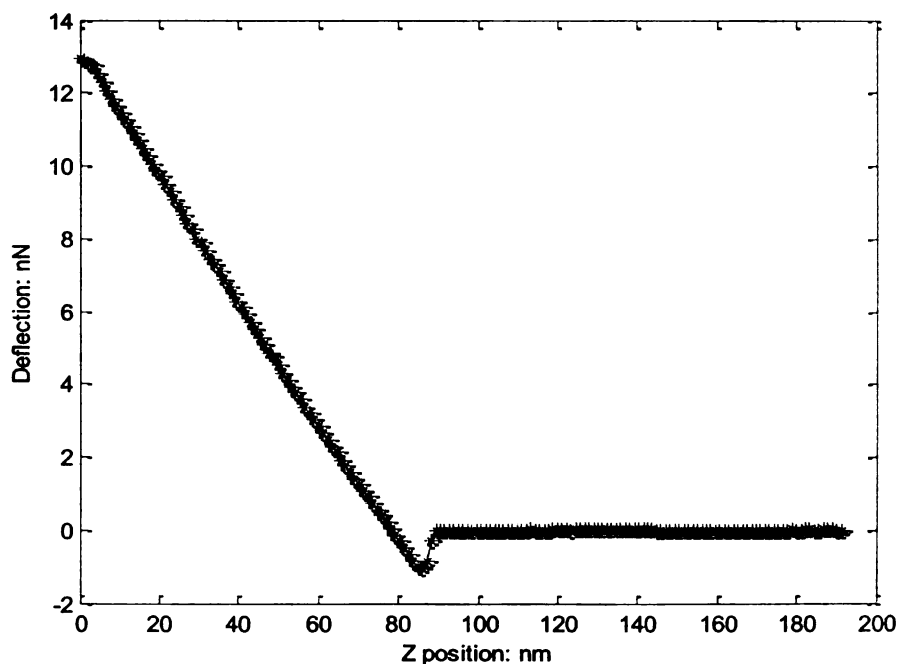
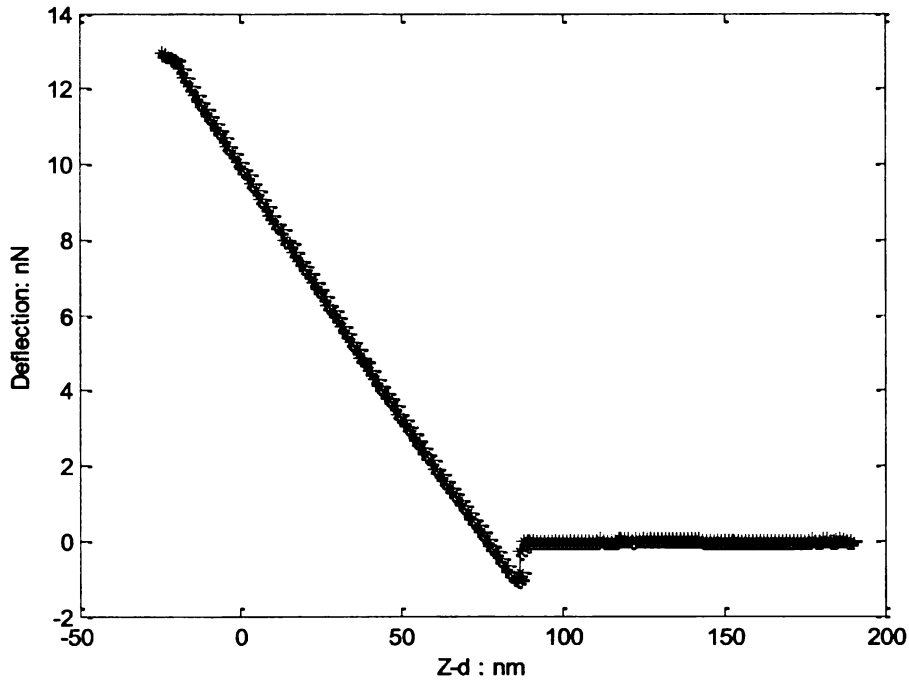


Figure 6.12 Approach force curve after average filter



**Figure 6.13 Force-distance curve and corresponding force-distance curve**

To analysis the elasticity property, different methods have been developed to interpret the force-distance curve.

The simplest way is to use the slop of the force curve in the contact region. In this method, the elastic response of the ample is assumed linear and an effective force constant, spring constant, then can be defined to characterize the elasticity of the sample. The spring constant of the sample  $K_s$  is defined as

$$K_s = \frac{K_C s}{1 - s} \quad (6.5)$$

where  $K_C$  is the spring constant of the cantilever,  $s$  is the slope of the force curve [121, 122].

Another method is called Force Integration to Equal Limits (FIEL) proposed by A-Hassan [69, 116, 117, 120]. FIEL method uses the Hertz model [81] to calculate the force between the tip and sample. If the tip of an AFM is approximated by a sphere, then the

force on the cantilever ( $F$ ) can be defined from the indentation ( $\delta$ ), elastic modulus ( $E$ ), Poisson ration ( $\nu$ ) and radius of the probe sphere

$$F_c = \frac{4E\sqrt{R}}{3(1-\nu)} \delta^{3/2} \quad (6.6)$$

To compare the elastic properties at two different positions, a pair of force-distance curves is collected at positions P1 and P2 using the relative trigger mode [59]. At these points, the force  $F_1$  equals force  $F_2$ . The work done by the cantilever at each position is the area under a force-distance curve, and is given by

$$w = \int_0^{\delta_t} Force \cdot d\delta = \frac{8}{15} \frac{\sqrt{R}}{\pi k} \delta_t^{5/2} \quad (6.7)$$

Therefore, the relationship between the elasticity and the force-distance curve at two different data positions is

$$\frac{w_1}{w_2} = \left( \frac{k_1}{k_2} \right)^{2/3} \quad (6.8)$$

where  $k = \frac{1-\nu}{\pi E}$  is inversely proportional to  $E$ , the elastic constant which represents the local elasticity of the sample. The area under the force-distance curve can be calculated and used to represent the inverse relative elasticity of the tissue scaffolding.

This method has the advantage of being independent of the tip-sample contact point, and of not requiring calibration of the AFM cantilever's spring force constant. However this method requires each force curve has the same force value at the end of indentation which is hard to achieve. FIEL method can provide the comparison result between different samples only if each sample is tested in same experimental conditions.

In this research, the widely used Hertz (or Sneddon) model [27, 53, 103, 112, 118, 119, 123] is applied to quantify the contact part of force curve (region 'c' in Figure 6.7). Since the tip is much harder than the sample, the elastic deformation of the sample can be related to its Young's modulus in the contact part of the force curve. The Hertz model describes the elastic deformation of two surfaces touching under a load force which was first treated by Hertz in 1881 [81]. The general force-indentation relation can be expressed as [95, 124]:

$$F = \lambda \delta^\beta \quad (6.9)$$

where  $F$  is the loading force and  $\delta$  is the indentation depth. The term  $\lambda$  and exponent  $\beta$  are parameters decided by the two touching surfaces. The sample surface can be considered as a flat soft sample. Two different geometries seem to be appropriate to describe the AFM tip.

1. Tip as a sphere of radius  $R$ , Hertz model is defined as [53, 124]:

$$F_{sphere} = \frac{4}{3} \frac{E}{(1-\mu^2)} \sqrt{R} \delta^{3/2} \quad (6.10)$$

where  $F_{sphere}$  is the measured force,  $E$  is the Young's modulus,  $\mu$  is the Poisson's ratio and  $\delta$  is the indentation depth.

2. Tip as a cylindrical cone of opening angle  $2\alpha$ , hertz model is defined as [53, 113, 125]:

$$F_{cone} = \frac{2}{\pi} \frac{E}{(1-\mu^2)} \tan(\alpha) \delta^2 \quad (6.11)$$

where  $F_{cone}$  is the measured force,  $E$  is the Young's modulus,  $\mu$  is the Poisson's ratio and  $\delta$  is the indentation depth.

As we discussed in chapter 5, we assume the tip end is sphere with the radius 100nm, the Hertz model we used is equation (6.10). The indentation  $\delta$  was calculated as follows:

$$\delta = (z - z_0) - (d - d_0) \quad (6.12)$$

Where  $z$  is the sample height,  $z_0$  is the contact point where tip touches the sample,  $d$  is the cantilever deflection and  $d_0$  is the deflection of the free cantilever when the cantilever is far from sample surface. To simplify the problem, the nonlinear force ( $F_{sphere}$ ) and indentation ( $\delta$ ) equation can be converted to linear equation of ( $F_{sphere}$ )<sup>2/3</sup> and  $\delta$  by substituting equation (6.12) to equation (6.10):

$$F_{sphere}^{2/3} = \left( \frac{4}{3} \frac{E}{(1-\mu^2)} \sqrt{R} \right)^{2/3} [(z - z_0) - (d - d_0)] \quad (6.13)$$

In equation(6.13),  $F_{sphere}$ ,  $z$ ,  $d$  and  $d_0$  can be obtained from the experimental force curves. As we discussed in chapter 5 the radius of the sphere in the tip's end can be chosen as 100nm. Typically, the Poisson's ration can be assumed as 0.5 for soft materials [124-127]. The unknown parameters are Young's modulus  $E$  and the tip-sample contact point  $z_0$ . In this work, we use a least squares estimation procedure to determine  $E$  and  $z_0$  by minimizing the error in equation (6.14) w.r.t unknown parameters  $E$  and  $z_0$

$$\sigma = \sqrt{\frac{1}{N} \sum_{i=1}^N ((F_{sphere}^{th})^{2/3} - (F_{sphere}^{exp})^{2/3})^2} \quad (6.14)$$

Where  $\sigma$  is the rms error,  $F_{sphere}^{exp}$  is the measured force in contact region 'c' and  $F_{sphere}^{th}$  is the force calculated using equation(6.13). Figure 6.14 shows the contact part force curve and the fitting result using equation (6.13) and (6.14). Figure 6.15 is the box plot of the Young's modulus ( $E$ ) estimated from six experiment force curves which shows the lower quartile, median, and upper quartile  $E$  values. The mean value of Young's modulus along the nanofiber is about 4675 Pa.

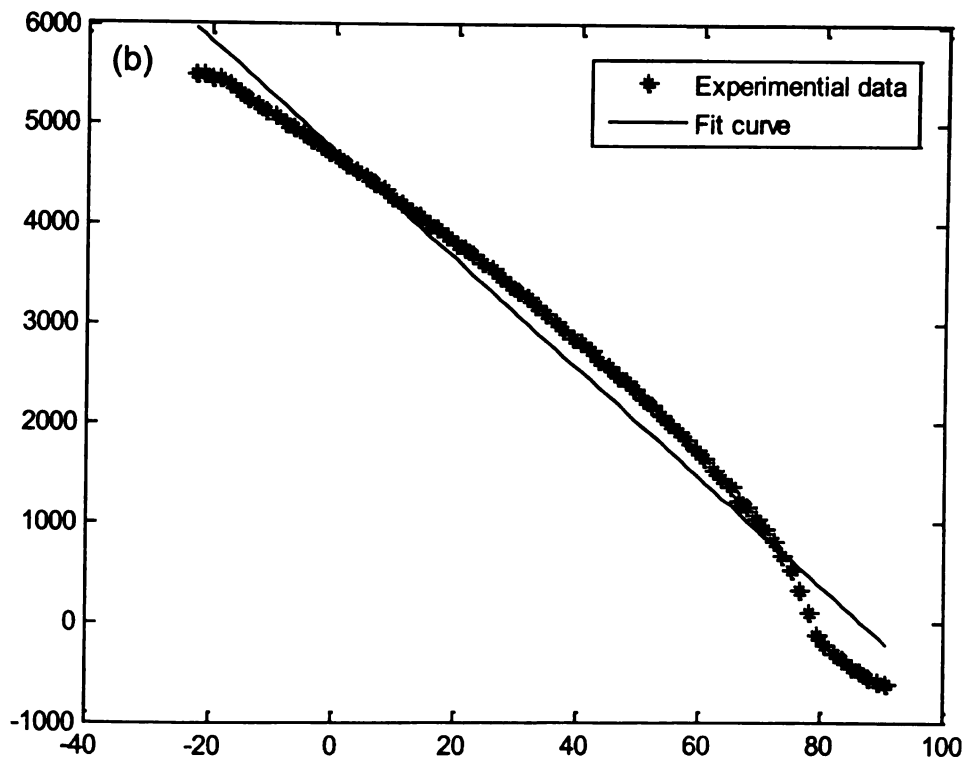
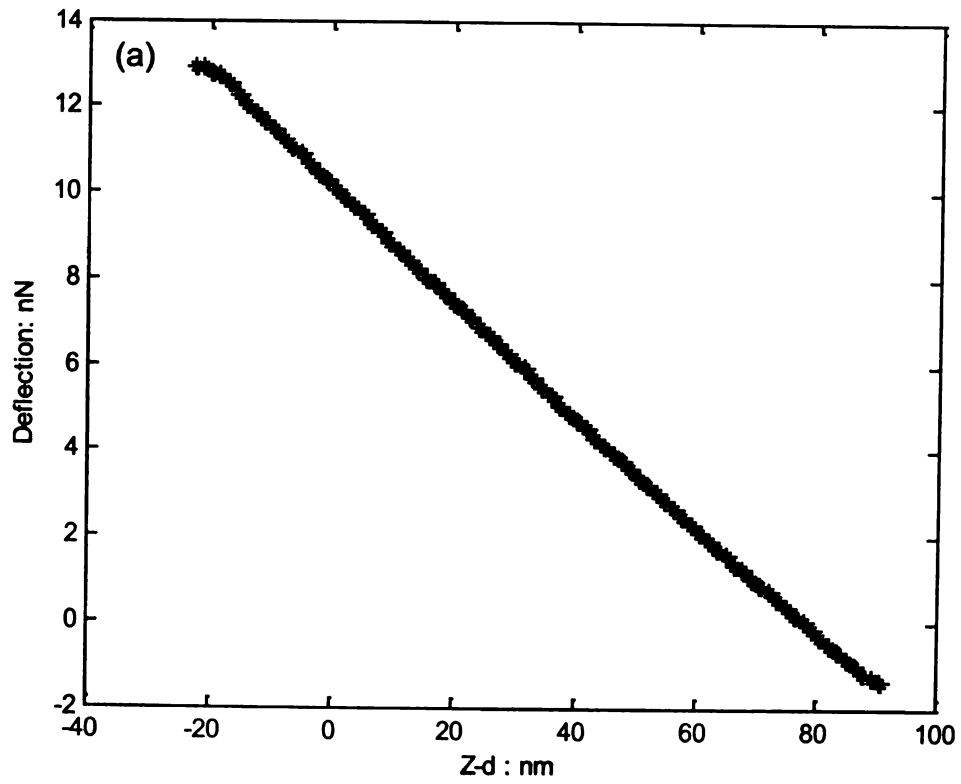
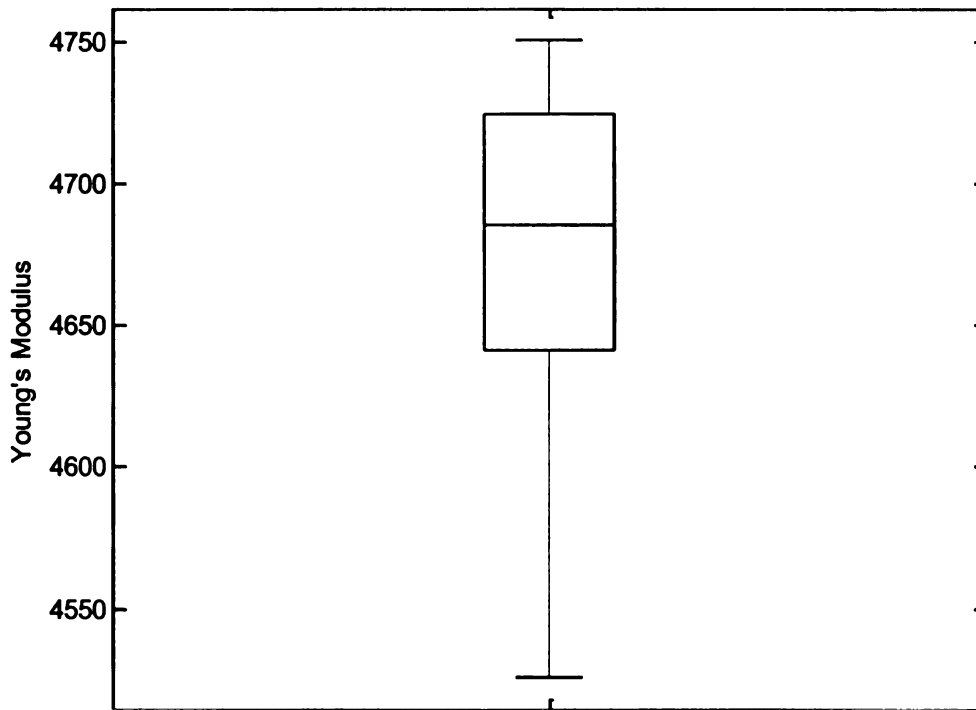


Figure 6.14 Force curve in contact region (a) and corresponding fitting result (b)



**Figure 6.15** Box plot of the estimated Young's modulus

## 6.5 Discussion

SPRM provided the first capability to collect statistically meaningful surface roughness information extracted along many individual nanofibers using an automatic procedure that maintained uniformity of experimental conditions. More importantly, histograms showing the distribution in the surface roughness values as well as the mode value were generated from the analysis of many individual nanofibers. The usual AFM individually applied ROI box would be most likely to return the mode value. However, the variances and distributions between samples under investigation can prove to be the real difference between them [70].

SPRM also provided the first capability to acquire force curves directly along an individual nanofiber under conditions such that the applied force was exactly normal to the curved nanofiber surface, therefore closing to conditions for appropriate use of the Hertz model elasticity analysis. This method is presently being refined and calibrated by our group and will lead to the statistically meaningful elasticity information extracted along many individual nanofibers using an automatic procedure that maintains uniformity of experimental conditions.

## **Chapter 7 Summary of Results and Future Work**

Scanning Probe Recognition Microscopy (SPRM) is an innovative and valuable extension of the capabilities of existing scanning probe microscopes. The SPRM allows adaptively track along individual structures within the scan area and provides statistically significant data for multiple properties by fine resolution scan restricted to the region of interest. Two implementation methods, namely, off-line processing scheme and an on-line dynamically adaptive multi-resolution scanning mode, are developed.

SPRM has the obvious advantage of saving operation time by scanning only regions of interest and ignoring other parts of the sample. This is especially useful for investigations of tissue scaffold properties, as a scaffold is composed of many individual nanofibers.

First-time SPRM investigations of tissue scaffold properties were performed directly along individual nanofibers. The results of a SPRM investigation of the surface roughness and elasticity of tissue scaffolds are presented. These investigations on curved nanofiber surfaces were enabled by the new SPRM ability to auto-track a restricted region of interest (ROI). For the surface roughness investigation, the ROI is the top area of the nanofiber. For the elasticity investigation, the ROI is only the central line of the nanofiber where the force applied by the tip is norm to the nanofiber surface thus providing meaningful force curves.

Deconvolution methods were developed and used for data accuracy along curved nanofiber surfaces. Geometric deconvolution, specifically the mathematical morphology method, was applied to the problem of surface roughness extraction. This was essential

for extraction of the true surface roughness along the nanoscale curved surface. An alternate approach for AFM data restoration, physics based deconvolution which includes the modeling and characterization of the tip and sample artifact sources, is also developed and applied to model systems. Initial results show the feasibility of the method for determining true topographic shapes of the sample.

The SPRM approach provided a wealth of data. Statistical methods based on histograms were developed to analyze the surface roughness and elasticity properties of the tissue scaffold nanofibers. The mode, mean, variance and distribution of surface roughness and elasticity were analyzed. This is the first time that statistically meaningful information has been extracted along individual nanofibers using an automatic procedure that maintains uniformity of experimental conditions.

#### **Future work**

One of the key components in the SPRM system is automatic detection of ROI. In this thesis, the height information alone is used to recognize an area of interest. In any SPM system many additional pieces of information are also provided. These include deflection, lateral force, phase etc. Based on the sample properties, these additional pieces of information can also be used to detect the ROI with greater accuracy and guide the SPM scan.

The SPRM can also be used in a purely recognition mode to study the conformational changes of features such as the 'open' and 'closed' state of ion channels. This feature can be extremely helpful in providing greater flexibility for handling a wide array of nanobiological investigations that involve conformational changes.

In the present work on surface roughness calculations, a Kasa circle fit method is used to acquire the true surface roughness on a curved surface. Deconvolution operation based on mathematical morphology methods was applied as the inverse operation to reverse the tip-shape dilation artifacts observed in AFM section measurements. In future work, the mathematical morphology deconvolution operation may be replaced by the force model based deconvolution procedure introduced in chapter 5.

The force-model based deconvolution algorithm has been developed and initial results show the feasibility of the method for determining true topographic shapes of the sample. However currently, the algorithm is applied to minimizing the error between model and measurement data at one position of the tip. The results will be much more accurate if the error is computed using VDW force calculations and measurements on a larger scan area centered at each point.

In this thesis, the force-model based deconvolution was performed on synthetic data due to lack of a calibration sample with well characterized shape information that can be used for generating measurements. The force based deconvolution should be validated with actual experimental data for which the true sample and tip shape information is available. Finally the force based model should be extended to include other components of the overall force that contribute to the tip sample interaction.

SPRM also provides the first capability to acquire force curves directly along an individual nanofiber under optimal conditions where the tip and hence applied force is exactly normal to the curved nanofiber surface. Methods for computing accurate values of the Young's modulus are currently under development. In particular two issues need to be addressed. The force-curve collected by SPRM is modeled to extract Young's modulus.

The model used in this work is the simple Hertz model which assumes the tip to be a sphere of radius = 100nm. The first issue is that the Hertz model does not consider the adhesion force between the tip-sample contact regions. In Hertz model, the sample surface is assumed to be flat which is not always true for tissue scaffold samples which nanofibers. Future work should be focused on a more accurate model of the force curve for estimating the Young's modulus. The second issue is calibration. In order to get accurate results, the model should be calibrated with a standard elastic sample.

Any property that can be investigated by scanning probe microscopy can be investigated by Scanning Probe Recognition Microscopy with auto-track on a region of interest. Work is also in progress to develop SPRM-based surface chemistry investigations, as this is known to be an important property for characterizing cell motility and adhesion [128]. Future work will develop data fusion methods that combine surface roughness, elasticity and surface chemistry information into a composite picture more truly representative of a cell's perception its environment.

## Reference:

- [1] G. Binnig and H. Rohrer, "Scanning tunnelling microscopy," *Helvetica Physica Acta*, vol. 55, pp. 726-735, 1982.
- [2] G. Binnig, H. Rohrer, C. Gerber, and E. Weibel, "Surface Studies by Scanning Tunneling Microscopy," *Physical Review Letters*, vol. 49, p. 57, 1982.
- [3] G. Binnig, H. Rohrer, C. Gerber, and E. Weibel, "7 x 7 Reconstruction on Si(111) Resolved in Real Space," *Physical Review Letters*, vol. 50, p. 120, 1983.
- [4] G. Binnig, C. F. Quate, and C. Gerber, "Atomic Force Microscope," *Physical Review Letters*, vol. 56, p. 930, 1986.
- [5] B. Drake, C. B. Prater, A. L. Weisenhorn, S. A. Gould, T. R. Albrecht, C. F. Quate, D. S. Cannell, H. G. Hansma, and P. K. Hansma, "Imaging crystals, polymers, and processes in water with the atomic force microscope," *Science*, vol. 243, pp. 1586-1589, March 24, 1989.
- [6] D. A. Bonnell, *Scanning probe microscopy and spectroscopy : theory, techniques, and applications*, 2nd ed. New York: Wiley-VCH, 2001.
- [7] C. M. Mate, G. M. McClelland, R. Erlandsson, and S. Chiang, "Atomic-scale friction of a tungsten tip on a graphite surface," *Physical Review Letters*, vol. 59, pp. 1942-1945, 1987.
- [8] G. Meyer and N. M. Amer, "Simultaneous measurement of lateral and normal forces with an optical-beam-deflection atomic force microscope," *Applied Physics Letters*, vol. 57, pp. 2089-2091, 1990.
- [9] U. D. Schwarz, P. Koster, and R. Wiesendanger, "Quantitative analysis of lateral force microscopy experiments," *Review of Scientific Instruments*, vol. 67, pp. 2560-2567, 1996.
- [10] D. Rugar, H. J. Mamin, P. Guethner, S. E. Lambert, J. E. Stern, I. McFadyen, and T. Yogi, "Magnetic force microscopy: General principles and application to longitudinal recording media," *Journal of Applied Physics*, vol. 68, pp. 1169-1183, 1990.

- [11] Y. Martin, D. W. Abraham, and H. K. Wickramasinghe, "High-resolution capacitance measurement and potentiometry by force microscopy," *Applied Physics Letters*, vol. 52, pp. 1103-1105, 1988.
- [12] J. E. Stern, B. D. Terris, H. J. Mamin, and D. Rugar, "Deposition and imaging of localized charge on insulator surfaces using a force microscope," *Applied Physics Letters*, vol. 53, pp. 2717-2719, 1988.
- [13] F. Muller, A. D. Muller, M. Hietschold, and S. Kammer, "Applications of scanning electrical force microscopy," *Microelectronics and Reliability*, vol. 37, pp. 1631-1634, 1997.
- [14] J. R. Matey and J. Blanc, "Scanning capacitance microscopy," *Journal of Applied Physics*, vol. 57, pp. 1437-1444, 1985.
- [15] C. D. Bugg and P. J. King, "Scanning capacitance microscopy," *Journal of Physics E: Scientific Instruments*, vol. 21, p. 147, 1988.
- [16] C. C. Williams, W. P. Hough, and S. A. Rishton, "Scanning capacitance microscopy on a 25 nm scale," *Applied Physics Letters*, vol. 55, pp. 203-205, 1989.
- [17] M. Nonnenmacher, M. P. O'Boyle, and H. K. Wickramasinghe, "Kelvin probe force microscopy," *Applied Physics Letters*, vol. 58, pp. 2921-2923, 1991.
- [18] J. M. R. Weaver and D. W. Abraham, "High resolution atomic force microscopy potentiometry," *Journal of Vacuum Science & Technology B: Microelectronics and Nanometer Structures*, vol. 9, pp. 1559-1561, 1991.
- [19] H. Sugimura, K. Hayashi, N. Saito, N. Nakagiri, and O. Takai, "Surface potential microscopy for organized molecular systems," *Applied Surface Science*, vol. 188, pp. 403-410, 2002.
- [20] A. Noy, D. V. Vezenov, and C. M. Lieber, "Chemical Force Microscopy," *Annual Review of Materials Science* vol. 27, pp. 381-421, 1997.
- [21] A. Hammiche, D. J. Hourston, H. M. Pollock, M. Reading, and M. Song, "Scanning thermal microscopy: Subsurface imaging, thermal mapping of polymer blends, and localized calorimetry," 1996, pp. 1486-1491.

- [22] A. Majumdar, "Scanning Thermal Microscopy," *Annual Review of Materials Science*, vol. 29, pp. 505-585, 1999.
- [23] R. C. Reddick, R. J. Warmack, D. W. Chilcott, S. L. Sharp, and T. L. Ferrell, "Photon scanning tunneling microscopy," *Review of Scientific Instruments*, vol. 61, pp. 3669-3677, 1990.
- [24] U. Durig, D. W. Pohl, and F. Rohner, "Near-field optical-scanning microscopy," *Journal of Applied Physics*, vol. 59, pp. 3318-3327, 1986.
- [25] D. Sarid, *Scanning force microscopy : with applications to electric, magnetic, and atomic forces*. New York: Oxford University Press, 1991.
- [26] F. J. Giessibl, "Advances in atomic force microscopy," *Reviews of Modern Physics*, vol. 75, pp. 949-35, 2003.
- [27] N. M. Ziebarth, E. P. Wojcikiewicz, F. Manns, V. T. Moy, and J. M. Parel, "Atomic force microscopy measurements of lens elasticity in monkey eyes," *Molecular Vision*, vol. 13, pp. 504-10, 2 April 2007.
- [28] Y. Martin, C. C. Williams, and H. K. Wickramasinghe, "Atomic force microscope--force mapping and profiling on a sub 100-[Å-ring] scale," *Journal of Applied Physics*, vol. 61, pp. 4723-4729, 1987.
- [29] Q. Zhong, D. Inniss, K. Kjoller, and V. B. Elings, "Fractured polymer/silica fiber surface studied by tapping mode atomic force microscopy," *Surface Science*, vol. 290, pp. L688-L692, 1993.
- [30] R. Garcia and R. Perez, "Dynamic atomic force microscopy methods," *Surface Science Reports*, vol. 47, pp. 197-301, 2002.
- [31] T. R. Albrecht, P. Grutter, D. Home, and D. Rugar, "Frequency modulation detection using high-Q cantilevers for enhanced force microscope sensitivity," *Journal of Applied Physics*, vol. 69, pp. 668-673, 1991.
- [32] G. Mahieu, P. Condette, B. Grandidier, J. P. Nys, G. Allan, D. Stievenard, E. Ph, H. Shimizu, and M. Tanaka, "Compensation mechanisms in low-temperature-grown Ga<sub>1-x</sub>Mn<sub>x</sub>As investigated by scanning tunneling spectroscopy," *Applied Physics Letters*, vol. 82, pp. 712-714, 2003.

- [33] N. D. Jager, E. R. Weber, K. Urban, and P. Ebert, "Importance of carrier dynamics and conservation of momentum in atom-selective STM imaging and band gap determination of GaAs(110)," *Physical Review B (Condensed Matter and Materials Physics)*, vol. 67, pp. 165327-10, 2003.
- [34] K. Thurmer, J. E. Reutt-Robey, and E. D. Williams, "Nucleation limited crystal shape transformations," *Surface Science*, vol. 537, pp. 123-133, 2003.
- [35] V. V. Prokhorov and K. Nitta, "AFM comparison of conformations acquired on mica by single molecules of polystyrene and polyethylene," *Physics of Low Dimensional Structures*, pp. 233-242, 2003.
- [36] B. Grévin, P. Rannou, R. Payerne, A. Pron, and J. P. Travers, "Scanning Tunneling Microscopy Investigations of Self-Organized Poly(3-hexylthiophene) Two-Dimensional Polycrystals," *Advanced Materials*, vol. 15, pp. 881-884, 2003.
- [37] K. Eom, P. C. Li, D. E. Makarov, and G. J. Rodin, "Relationship between the Mechanical Properties and Topology of Cross-Linked Polymer Molecules: Parallel Strands Maximize the Strength of Model Polymers and Protein Domains," *J. Phys. Chem. B*, vol. 107, pp. 8730-8733, August 28, 2003 2003.
- [38] K. Hajin, J. Lee, S. J. Kahng, Y. W. Son, S. B. Lee, C. K. Lee, J. Ihm, and K. Young, "Direct Observation of Localized Defect States in Semiconductor Nanotube Junctions," *Physical Review Letters*, vol. 90, p. 216107, 2003.
- [39] P. Thordarson, R. Atkin, W. H. J. Kalle, G. G. Warr, and F. Braet, "Developments in Using Scanning Probe Microscopy To Study Molecules on Surfaces -- From Thin Films and Single-Molecule Conductivity to Drug-Living Cell Interactions," *Australian Journal of Chemistry*, vol. 59, pp. 359-375, 2006.
- [40] L. Bozec and M. Horton, "Topography and Mechanical Properties of Single Molecules of Type I Collagen Using Atomic Force Microscopy," *Biophysical Journal*, vol. 88, pp. 4223-4231, June 1, 2005 2005.
- [41] A. Andrea and F. Paolo, "AFM: a versatile tool in biophysics," *Measurement Science and Technology*, vol. 16, pp. R65-R92, June 2005.
- [42] S. Myhra, "A review of enabling technologies based on scanning probe microscopy relevant to bioanalysis," *Biosensors and Bioelectronics*, vol. 19, pp. 1345-1354, 2004.

- [43] N. Gadegaard, "Atomic force microscopy in biology: technology and techniques," *Biotechnic & Histochemistry*, vol. 81, pp. 87-97, 2006.
- [44] A. L. Weisenhorn, P. K. Hansma, T. R. Albrecht, and C. F. Quate, "Forces in atomic force microscopy in air and water," *Applied Physics Letters*, vol. 54, pp. 2651-2653, 1989.
- [45] Z. Shao and J. Yang, "Progress in high resolution atomic force microscopy in biology," *Quarterly Reviews of Biophysics*, vol. 28, pp. 195-251, 1995.
- [46] I. C. Gebeshuber, J. H. Kindt, J. B. Thompson, Y. Del Amo, H. Stachelberger, M. A. Brzezinski, G. D. Stucky, D. E. Morse, and P. K. Hansma, "Atomic force microscopy study of living diatoms in ambient conditions," *Journal of Microscopy* vol. 212, pp. 292-299, 2003.
- [47] H. G. Hansma, "Surface biology of DNA by atomic force microscopy," *Annual Rev. of Phys. Chem.*, vol. 52, pp. 71-92, 2001.
- [48] S. Kasas, N. H. Thomson, B. L. Smith, H. G. Hansma, X. Zhu, M. Guthold, C. Bustamante, E. T. Kool, M. Kashlev, and P. K. Hansma, "*Escherichia coli* RNA Polymerase Activity Observed Using Atomic Force Microscopy," *Biochemistry*, vol. 36, pp. 461-468, January 21, 1997 1997.
- [49] Z. Shao, "Probing Nanometer Structures with Atomic Force Microscopy," *News in Physiological Sciences*, vol. 14, pp. 142-149, August 1 1999.
- [50] E. L. Florin, V. T. Moy, and H. E. Gaub, "Adhesion Forces between individual ligand-receptor pairs," *Science*, vol. 265, pp. 415-417, 1994.
- [51] P. C. Braga and D. Ricci, *Atomic Force Microscopy: Biomedical Methods and Applications* vol. 242. New Jersey: Humana Press, 2003.
- [52] Y. Jiao and T. E. Schaffer, "Accurate Height and Volume Measurements on Soft Samples with the Atomic Force Microscope," *Langmuir*, vol. 20, pp. 10038-10045, November 9, 2004 2004.
- [53] A. Touhami, B. Nysten, and Y. F. Dufrene, "Nanoscale Mapping of the Elasticity of Microbial Cells by Atomic Force Microscopy," *Langmuir*, vol. 19, pp. 4539-4543, May 27, 2003 2003.

- [54] A. P. Gunning, A. R. Kirby, A. R. Mackie, P. Kroon, G. Williamson, and V. J. Morris, "Watching molecular processes with the atomic force microscope: dynamics of polymer adsorption and desorption at the single molecule level," *Journal of Microscopy*, vol. 216, pp. 52-56, 2004.
- [55] A. E. Pelling, S. Sehati, E. B. Gralla, J. S. Valentine, and J. K. Gimzewski, "Local Nanomechanical Motion of the Cell Wall of *Saccharomyces cerevisiae*," *Science*, vol. 305, pp. 1147-1150, August 20 2004.
- [56] J. S. Villarrubia, "Algorithms for scanned probe microscope image simulation, surface reconstruction, and tip estimation," *Journal of Research of the National Institute of Standards and Technology*, vol. 102, pp. 425-454, Jul-Aug 1997.
- [57] D. Keller, "Reconstruction of STM and AFM images distorted by finite size tips," *Surface Science*, vol. 253, pp. 353-364, 1991.
- [58] C. Le Grimmellec, E. Lesniewska, M.-C. Giocondi, E. Finot, V. Vie, and J.-P. Goudonnet, "Imaging of the Surface of Living Cells by Low-Force Contact-Mode Atomic Force Microscopy," *Biophys Journal*, vol. 75, pp. 695-703, August 1 1998.
- [59] "MultiMode SPM Instruction Manual," Veeco Instruments Inc.
- [60] *NanoScope Signal Access Module (SAM)-Description & Use*. Santa Barbara, CA: Digital Instruments, 1997.
- [61] F. Landousy and E. L. Cam, "Probing DNA-Protein Interactions with AFM," *Veeco Instruments Application Note*.
- [62] Q. Chen, Y. Fan, L. Udpa, and V. M. Ayres, "Cell Classification by Moments and Continuous Wavelet Transform Methods," *Int. J. Nanomedicine* vol. 2, 2007.
- [63] H. Blum, "A transformation for extracting new descriptors of shape," in *Models for the Perception of Speech and Visual Form*, W. Wathen-Dunn, Ed. Cambridge: MIT Press, 1967, pp. 362-380.
- [64] H. Blum and R. N. Nagel, "Shape description using weighted symmetric axis features," *Pattern Recognition*, vol. 10, pp. 167-180, 1978.

- [65] L. Lam, S. W. Lee, and C. Y. Suen, "Thinning methodologies-a comprehensive survey," *Pattern Analysis and Machine Intelligence, IEEE Transactions on*, vol. 14, pp. 869-885, 1992.
- [66] Y. Ge and J. M. Fitzpatrick, "On the generation of skeletons from discrete Euclidean distance maps," *Pattern Analysis and Machine Intelligence, IEEE Transactions on*, vol. 18, pp. 1055-1066, 1996.
- [67] R. Ogniewicz and M. Ilg, "Voronoi skeletons: theory and applications," in *Computer Vision and Pattern Recognition, 1992. Proceedings CVPR '92., 1992 IEEE Computer Society Conference on*, 1992, pp. 63-69.
- [68] N. R. Howe, "<http://maven.smith.edu/~nhowe/research/code/>."
- [69] Y. Fan, Q. Chen, V. M. Ayres, L. Udpa, and A. F. Rice, "Scanning Probe Recognition Microscopy Investigation of Cell Elastic Properties," in *2005 APS March Meeting Los Angeles, CA*, 2005.
- [70] Y. Fan, Q. Chen, V. M. Ayres, A. D. Baczewski, L. Udpa, and S. Kumar, "Scanning Probe Recognition Microscopy Investigation of Tissue Scaffold Properties," *Int. J. Nanomedicine*, vol. 2, 2007.
- [71] K. S. Arun, T. S. Huang, and S. D. Blostein, "Least-squares fitting of two 3-D point sets," *IEEE Trans. Pattern Anal. Mach. Intell.* , vol. 9, pp. 698-700, September 1987.
- [72] J. S. Villarrubia, "Morphological estimation of tip geometry for scanned probe microscopy," *Surface Science*, vol. 321, pp. 287-300, 1994.
- [73] L. Udpa, V. M. Ayres, F. Yuan, C. Qian, and S. A. Kumar, "Deconvolution of atomic force microscopy data for cellular and molecular imaging," *Signal Processing Magazine, IEEE*, vol. 23, pp. 73-83, 2006.
- [74] S. A. Kumar, "Deconvolution of Atomic Force Microscopy Image Data," in *Electrical & Computer engineering*. vol. Master of Science East Lansing: Michigan State University, 2007.

- [75] G. S. Pingali and R. Jain, "Restoration of scanning probe microscope images," in *IEEE Workshop on Applications of Computer Vision*, Palm Springs, CA, USA, 1992, pp. 282-289.
- [76] D. Keller, "Reconstruction of STM and AFM images distorted by finite-size tips," *Surface Science*, vol. 253, pp. 353-364, 1991.
- [77] H. B. Callen, *Thermodynamics*, 2nd ed. New York: Wiley, 1985.
- [78] J. S. Villarubia, "Morphological Estimation of tip geometry for Scanned probe Microscopy," *Surface Science*, pp. 287-300, 1994.
- [79] P. M. Williams, K. M. Shakesheff, M. C. Davies, D. E. Jackson, C. J. Roberts, and S. J. B. Tendler, *J. Vac. Sci Technology*, p. 1557, 1996.
- [80] J. Israelachvili, *Intermolecular and surface forces*, 2nd ed. London: Academic Press London, 1991.
- [81] H. Hertz, "Über den Kontakt elastischer Körper," *J. Reine Angew. Mathematik*, vol. 92, p. 156, 1881.
- [82] K. L. Johnson, K. Kendall, and A. D. Roberts, "Surface Energy and the Contact of Elastic Solids," *Proceedings of the Royal Society of London. Series A, Mathematical and Physical Sciences*, vol. 324, pp. 301-313, 1971.
- [83] B. V. Derjaguin, V. M. Muller, and Y. P. Toporov, "Effect of contact deformations on the adhesion of particles," *Journal of Colloid and Interface Science*, vol. 53, pp. 314-326, 1975.
- [84] V. M. Muller, B. V. Derjaguin, and Y. P. Toporov, "On two methods of calculation of the force of sticking of an elastic sphere to a rigid plane," *Colloids and Surfaces*, vol. 7, pp. 251-259, 1983.
- [85] D. Sarid, *Scanning force microscopy : with applications to electric, magnetic, and atomic forces*, Rev. ed. New York: Oxford University Press, 1994.

- [86] Y. N. Moiseev, V. M. Mostepanenko, V. I. Panov, and I. Y. Sokolov, "Force dependences for the definition of the atomic force microscopy spatial resolution," *Physics Letters A*, vol. 132, pp. 354-358, 1988.
- [87] U. Hartmann, "van der Waals interactions between sharp probes and flat sample surfaces," *Physical Review B*, vol. 43, p. 2404, 1991.
- [88] J. L. Hutter and J. Bechhoefer, "Measurement and manipulation of van der Waals forces in atomic-force microscopy," in *The 1993 international conference on scanning tunneling microscopy*, Beijing, China, 1994, pp. 2251-2253.
- [89] C. Argento and R. H. French, "Parametric tip model and force--distance relation for Hamaker constant determination from atomic force microscopy," *Journal of Applied Physics*, vol. 80, pp. 6081-6090, 1996.
- [90] F. London, "The general theory of molecular forces," *Trans. Faraday Soc.*, vol. 33, 1937.
- [91] H. C. Hamaker, "The London-van der Waals attraction between spherical particles," *Physica (Amsterdam)*, vol. 4, pp. 1058-1072, 1937.
- [92] C. Argento, A. Jagota, and W. C. Carter, "Surface formulation for molecular interactions of macroscopic bodies," *Journal of the Mechanics and Physics of Solids*, vol. 45, pp. 1161-1183, 1997.
- [93] H. D. Ackler, R. H. French, and Y.-M. Chiang, "Comparisons of Hamaker Constants for Ceramic Systems with Intervening Vacuum or Water: From Force Laws and Physical Properties," *Journal of Colloid and Interface Science*, vol. 179, pp. 460-469, 1996.
- [94] B. Cappella and G. Dietler, "Force-distance curves by atomic force microscopy," *Surface Science Reports*, vol. 34, pp. 1-104, 1999.
- [95] H.-J. Butt, B. Cappella, and M. Kappl, "Force measurements with the atomic force microscope: Technique, interpretation and applications," *Surface Science Reports*, vol. 59, pp. 1-152, 2005.
- [96] S. I. Zanette, A. O. Caride, V. B. Nunes, G. L. Klimchitskaya, F. L. Freire, and R. Prioli, "Theoretical and experimental investigation of the force-distance relation

- for an atomic force microscope with a pyramidal tip," *Surface Science*, vol. 453, pp. 75-82, 2000.
- [97] A. Atala, "Technology insight: Applications of tissue engineering and biological substitutes in urology," *Nat Clin Pract Urol*, vol. 2, pp. 143-9, Mar 2005.
- [98] J. C. Hu and K. A. Athanasiou, "A self-assembling process in articular cartilage tissue engineering," *Tissue Eng*, vol. 12, pp. 969-79, Apr 2006.
- [99] M. Xu, P. K. Kreeger, L. D. Shea, and T. K. Woodruff, "Tissue-Engineered Follicles Produce Live, Fertile Offspring," *Tissue Eng*, vol. 12, pp. 2739-2746, Jun 1 2006.
- [100] "Tissue\_engineering," in *Wikipedia*:  
[http://en.wikipedia.org/wiki/Tissue\\_engineering](http://en.wikipedia.org/wiki/Tissue_engineering), 2007.
- [101] R. Langer and J. P. Vacanti, "Tissue engineering," *Science*, vol. 260, pp. 920-926, May 14, 1993 1993.
- [102] D. D. Deligianni, N. D. Katsala, P. G. Koutsoukos, and Y. F. Missirlis, "Effect of surface roughness of hydroxyapatite on human bone marrow cell adhesion, proliferation, differentiation and detachment strength," *Biomaterials*, vol. 22, pp. 87-96, 2001.
- [103] A. J. Engler, L. Richert, J. Y. Wong, C. Picart, and D. E. Discher, "Surface probe measurements of the elasticity of sectioned tissue, thin gels and polyelectrolyte multilayer films: Correlations between substrate stiffness and cell adhesion," *Surface Science*, vol. 570, pp. 142-154, 2004.
- [104] Y. Dzenis, "Spinning Continuous Fibers for Nanotechnology," *Science*, vol. 304, pp. 1917-1919, June 25 2004.
- [105] G. Taylor, "Electrically Driven Jets," *Proceedings of the Royal Society of London. Series A, Mathematical and Physical Sciences*, vol. 313, pp. 453-475, 1969.
- [106] H. Y. Chung, J. R. B. Hall, M. A. Gogins, D. G. Crofoot, and T. M. Weik, "Polymer, polymer microfiber, polymer nanofiber and applications including filter structures," United States Patent No. 6743273: Donaldson Company, Inc 2004.

- [107] Digital, "Chapter 14.6," in *Command Reference Manual*, Instruments 2003, pp. 381-400.
- [108] Q. Chen, "Scanning Probe Recognition Microscopy: Recognition Strategies," in *Electrical & Computer Engineering Department*. vol. Ph. D East Lansing: Michigan State University, 2007.
- [109] Y. Fan, Q. Chen, S. Kumar, A. D. Baczewski, L. Udpa, V. M. Ayres, and A. F. Rice, "Scanning Probe Recognition Microscopy Investigation of Nanoscale Mechanical and Surface Roughness Properties Along Nanofibers," in *Surface and Interfacial Nanomechanics* edited by R.F. Cook, W. Ducker, I. Szlufarska, R.F. Antrim (Mater. Res. Soc. Symp. Proc. Volume 1021E, Warrendale, PA, 2007), 2007, pp. 1021-HH05-26.
- [110] I. Kasa, "A curve fitting procedure and its error analysis," *IEEE Trans. Inst. Meas.*, vol. 25, pp. 8-14, 1976.
- [111] R. C. Gonzalez and R. E. Woods, *Digital image processing*, 2nd ed. Upper Saddle River, N.J.: Prentice Hall, 2002.
- [112] T. Svaldo-Lanero, S. Krol, R. Magrassi, A. Diaspro, R. Rolandi, A. Gliozzi, and O. Cavalleri, "Morphology, mechanical properties and viability of encapsulated cells," *Ultramicroscopy*, vol. In Press, Corrected Proof, 2007.
- [113] H. Haga, S. Sasaki, K. Kawabata, E. Ito, T. Ushiki, and T. Sambongi, "Elasticity mapping of living fibroblasts by AFM and immunofluorescence observation of the cytoskeleton," *Ultramicroscopy*, vol. 82, pp. 253-258, 2000.
- [114] M. Lekka, P. Laidler, D. Gil, J. Lekki, Z. Stachura, and A. Z. Hryniewicz, "Elasticity of normal and cancerous human bladder cells studied by scanning force microscopy," *European Biophysics Journal*, vol. 28, pp. 312-316, 1999.
- [115] N. Almqvist, R. Bhatia, G. Primbs, N. Desai, S. Banerjee, and R. Lal, "Elasticity and Adhesion Force Mapping Reveals Real-Time Clustering of Growth Factor Receptors and Associated Changes in Local Cellular Rheological Properties," *Biophysical Journal*, vol. 86, pp. 1753-1762, March 2004.
- [116] E. A-Hassan, W. F. Heinz, M. D. Antonik, N. P. D'Costa, S. Nageswaran, C.-A. Schoenenberger, and J. H. Hoh, "Relative Microelastic Mapping of Living Cells

- by Atomic Force Microscopy," *Biophys. J.*, vol. 74, pp. 1564-1578, March 1, 1998 1998.
- [117] P. Schaer-Zammaretti and J. Ubbink, "Imaging of lactic acid bacteria with AFM--elasticity and adhesion maps and their relationship to biological and structural data," *Ultramicroscopy*, vol. 97, pp. 199-208, 2003.
- [118] M. Radmacher, M. Fritz, and P. K. Hansma, "Imaging soft samples with the atomic force microscope: gelatin in water and propanol," *Biophys. J.*, vol. 69, pp. 264-270, July 1, 1995 1995.
- [119] M. Radmacher, M. Fritz, C. M. Kacher, J. P. Cleveland, and P. K. Hansma, "Measuring the viscoelastic properties of human platelets with the atomic force microscope," *Biophys. J.*, vol. 70, pp. 556-567, January 1, 1996 1996.
- [120] Q. Chen, Y. Fan, V. M. Ayres, L. Udpa, M. Schindler, and A. Rice, "Scanning Probe Recognition Microscopy Investigation of Elastic Properties of Tissue Scaffolding," in *MRS 2004 Fall*, Warrendale, PA, 2004.
- [121] C. J. Sullivan, S. Venkataraman, S. T. Retterer, D. P. Allison, and M. J. Doktycz, "Comparison of the indentation and elasticity of *E. coli* and its spheroplasts by AFM," *Ultramicroscopy*, vol. 107, pp. 934-942, 2007.
- [122] S. B. Velegol and B. E. Logan, "Contributions of bacterial surface polymers, electrostatics, and cell elasticity to the shape of AFM force curves," *Langmuir*, vol. 18, pp. 5256-5262, 2002.
- [123] I. N. Sneddon, "The relation between load and penetration in the axisymmetric Boussinesq problem for a punch of arbitrary profile," *Int. J. Eng. Sci.*, vol. 3, pp. 47-57, 1965.
- [124] D. C. Lin, E. K. Dimitriadis, and F. Horkay, "Robust Strategies for Automated AFM Force Curve Analysis—I. Non-adhesive Indentation of Soft, Inhomogeneous Materials," *Journal of Biomechanical Engineering*, vol. 129, pp. 430-440, June 2007.
- [125] J. Domke and M. Radmacher, "Measuring the Elastic Properties of Thin Polymer Films with the Atomic Force Microscope," *Langmuir*, vol. 14, pp. 3320-3325, 1998.

- [126] M. Radmacher, "Measuring the elastic properties of biological samples with the AFM," *Engineering in Medicine and Biology Magazine, IEEE*, vol. 16, pp. 47-57, 1997.
- [127] L. R. Nyland and D. W. Maughan, "Morphology and Transverse Stiffness of Drosophila Myofibrils Measured by Atomic Force Microscopy," *Biophys. J.*, vol. 78, pp. 1490-1497, March 1, 2000 2000.
- [128] I. Ahmed, H.-Y. Liu, P. C. Mamiya, A. S. Ponery, A. N. Babu, T. Weik, M. Schindler, and S. Meiners, "Three-dimensional nanofibrillar surfaces covalently modified with tenascin-C-derived peptides enhance neuronal growth *in vitro*," *Journal of Biomedical Materials Research Part A*, vol. 76A, pp. 851-860, 2006.

MICHIGAN STATE UNIVERSITY LIBRARIES



3 1293 03063 2834